

High-Speed Modulation of Optical Injection-Locked Semiconductor Lasers

Erwin K Lau



Electrical Engineering and Computer Sciences
University of California at Berkeley

Technical Report No. UCB/EECS-2006-188

<http://www.eecs.berkeley.edu/Pubs/TechRpts/2006/EECS-2006-188.html>

December 18, 2006

Copyright © 2006, by the author(s).
All rights reserved.

Permission to make digital or hard copies of all or part of this work for personal or classroom use is granted without fee provided that copies are not made or distributed for profit or commercial advantage and that copies bear this notice and the full citation on the first page. To copy otherwise, to republish, to post on servers or to redistribute to lists, requires prior specific permission.

High-Speed Modulation of Optical Injection-Locked Semiconductor Lasers

by

Erwin K. Lau

S.B. (Massachusetts Institute of Technology) 2000
M.Eng. (Massachusetts Institute of Technology) 2001

A dissertation submitted in partial satisfaction of the
requirements for the degree of

Doctor of Philosophy

in

Engineering – Electrical Engineering and Computer Sciences

in the

Graduate Division

of the

UNIVERSITY *of* CALIFORNIA, BERKELEY

Committee in charge:

Professor Ming C. Wu, Chair
Professor Constance Chang-Hasnain
Professor Xiang Zhang

Fall 2006

The dissertation of Erwin K. Lau is approved:

Professor Ming C. Wu, Chair

Date

Professor Constance Chang-Hasnain

Date

Professor Xiang Zhang

Date

University of California, Berkeley

Fall 2006

High-Speed Modulation of Optical Injection-Locked Semiconductor Lasers

© 2006

by Erwin K. Lau

TABLE OF CONTENTS

TABLE OF CONTENTS.....	i
LIST OF FIGURES	iv
LIST OF TABLES.....	ix
ACKNOWLEDGEMENT	x
ABSTRACT.....	xi
CHAPTER 1 INTRODUCTION	1
1.2 HISTORY	7
1.2.2 Resonance Frequency Enhancement.....	12
1.2.3 Reduction of Non-Linear Distortions	13
1.2.4 RIN Reduction	14
1.3 APPLICATIONS	15
1.3.1 Link Gain Improvement by Gain-Lever OIL.....	15
1.3.2 Optical Injection Phase-Locked Loop.....	18
1.3.3 Injection Locking of Mode-locked Lasers	20
1.3.4 All-Optical Signal Processing.....	21
1.3.5 Other Applications	23
1.4 ORGANIZATION OF DISSERTATION	23
CHAPTER 2 RATE EQUATION THEORY	25
2.1 MOTIVATION.....	25
2.2 RATE EQUATIONS	25
2.3 RATE EQUATION SOLUTIONS.....	27
2.3.1 Steady State Solutions.....	27
2.3.2 Dynamic Solutions.....	28
2.4 LOCKING MAP AND STABILITY	30
2.5 MODULATION REGIMES.....	36
2.5.1 Injection Ratio Effects on Frequency Response	37
2.5.2 Detuning Frequency Effects on Frequency Response	40
2.6 ANALYTIC APPROXIMATIONS FOR LASER FIGURES-OF-MERIT.....	46
2.6.1 Resonance Frequency	47
2.6.2 Damping.....	49
2.6.3 Low-Frequency Gain	51
2.6.4 Frequency Response: The Real Pole.....	53
2.6.5 Frequency Response: The Zero	54
2.6.6 Optimizing Bandwidth.....	55
2.7 CAVITY MODE	57
2.8 PHASOR MODEL.....	65
CHAPTER 3 INJECTION RATIO AND QUALITY FACTOR.....	69
3.1 MOTIVATION.....	69
3.2 DEFINITION OF INJECTION RATIO	70

3.2.1 Conventional Injection Ratio Definition.....	70
3.2.2 External Injection Ratio.....	72
3.2.3 Internal Injection Ratio.....	74
3.2.4 Relating Internal to External Injection Ratios.....	75
3.3 MAXIMUM RESONANCE FREQUENCY ENHANCEMENT.....	77
3.4 FUNDAMENTAL LIMIT OF THE MAXIMUM RESONANCE FREQUENCY ENHANCEMENT FACTOR BASED ON COUPLING QUALITY FACTOR.....	84
3.5 TIME-BANDWIDTH PRODUCT.....	86
3.6 ANALOGY TO ELECTRICAL OSCILLATORS.....	87
3.7 SUMMARY.....	87
 CHAPTER 4 HETERODYNE DETECTION.....	 89
4.1 MOTIVATION.....	89
4.2 THEORY.....	91
4.3 METHOD.....	93
4.4 MODULATION SIDEBAND SEPARATION.....	98
4.4.2 Quantifying the Sideband Asymmetries.....	100
 CHAPTER 5 HIGH-FREQUENCY INJECTION-LOCKED LASERS.....	 101
5.1 MOTIVATION.....	101
5.2 LASER STRUCTURE.....	104
5.3 EXPERIMENTAL SETUP.....	107
5.4 RESONANCE FREQUENCY EVOLUTION.....	109
5.5 EXPERIMENTAL RESULTS.....	117
5.5.1 Optimized Resonance Frequency.....	117
5.5.2 Optimized Broadband Performance.....	119
5.6 DISCUSSION.....	120
5.6.1 Facets of Two-Section DFB Lasers.....	120
5.6.2 > 100 GHz Resonance Frequencies.....	121
5.6.3 Future Plans.....	121
 CHAPTER 6 MODULATION OF THE MASTER LASER.....	 123
6.1 MOTIVATION.....	123
6.2 EXPERIMENT.....	124
6.3 THEORY.....	128
6.4 ANALYSIS.....	132
6.4.1 Direct Modulation.....	133
6.4.2 RAM Suppression.....	134
6.4.3 FM-to-AM Conversion.....	136
6.4.4 FM Efficiency.....	138
6.5 DISCUSSION.....	140
 CHAPTER 7 CONCLUSION.....	 141
7.1 FUTURE APPLICATIONS.....	141
7.1.1 Opto-Electronic Oscillator.....	141
7.2 SUMMARY.....	145
 APPENDIX 1 MATLAB CODE.....	 147
A1.1 LOCKING RANGE MAPPING: LOCKINGRANGE . M.....	147

A1.2 PLOTTING SCRIPTS: LASERPLOT . M.....	150
A1.3 LASER PARAMETERS: LASERPARAM . M.....	155
A1.4 DIFFERENTIAL EQUATION SOLUTION: LASERODE . M.....	156
A1.5 INJECTION-LOCKED LASER RATE EQUATION: RATEEQ . M.....	161
BIBLIOGRAPHY.....	162

LIST OF FIGURES

Figure 1.1 Schematic of optical injection-locked laser system: (a) transmission-style (b) reflection-style.....	3
Figure 1.2 Conceptual diagram of injection locking: (a) free-running laser (b) slave with injected light, before locking (c) locked slave laser.	5
Figure 1.3 Physical gain competition model of injection locking. (a) Illustration of gain model. (b) Detuning dependence on optical intensity, showing competition of ASE and amplified injected intensity, after Henry [2].	6
Figure 1.4 Huygens thought experiment showing injection locking of wall-coupled pendulum clocks. (a) Pendulums are out of phase and frequency, but coupled by wall vibrations. (b) Over time, pendulums eventually lock in frequency with opposite phase.	8
Figure 1.5 Frequency response showing resonance frequency enhancement via OIL [33]. The resonance frequency is improved with increasing injection ratio.....	13
Figure 1.6 SFDR of a directly-modulated DFB laser [42]. Dash/diamonds show the free-running IMP3 power. Solid line/circles show the injection-locked IMP3 power. SFDR improvement was shown to be $5 \text{ dB}\cdot\text{MHz}^{2/3}$	14
Figure 1.7 Experimental (left) and theoretical (right) RIN spectra for free-running and various injection levels and detuning frequencies [45]. The RIN peak at free-running was pushed to higher frequencies, thereby reducing the RIN near the free-running relaxation oscillation.	15
Figure 1.8 (a) Concept of gain-levering [47, 48]. (a) Frequency response: dots: free-running laser, uniform bias; dashes: free-running gain-lever laser, showing increased DC gain; solid: injection-locked gain-lever laser, showing both increased DC gain and increased relaxation oscillation [49].....	17
Figure 1.9 Diagram explaining sources of SFDR improvement. The IMD3 term was reduced by 15 dB and the RIN reduced by 7 dB, totaling to a SFDR improvement of $12 \text{ dB}\cdot\text{Hz}^{2/3}$	18
Figure 1.10 (a) Schematic of optical injection-locked phase-locked loop (OIPLL) [52]. (b) Phase noise spectra for free-running, optical phase locked loop (OPLL), optical injection-locked, and OIPLL systems. The OIL system excels in reducing linewidth of the laser, the OPLL excels in reducing the low-frequency phase noise. The OIPLL system combines the advantages of both.	19
Figure 1.11 Signal channelization schematic. The wideband RF signal is sent to a free-space dispersive grating, which send each channel to its respective detectors. The system ensures synchronization with the desired channel spacing by locking the RF signal's carrier with a known, stable source.	21

Figure 1.12 Pulse-reshaping by OIL [57]. (a) shows the concept. (b) shows experimental results. Top graph is the input pulses with noticeable smoothness. Bottom graph is the output pulse, having a more square-like function.	22
Figure 2.1 Locking range showing the dependence of ϕ across the locking range. n.s. corresponds to the unstable locking regime.	33
Figure 2.2 Phase and injection ratio versus: (a) detuning frequency, (b) resonance frequency, (c) normalized field, and (d) normalized carrier density. The range of phases correspond to $-\pi/2$ to $\cot^{-1}\alpha$	35
Figure 2.3 Locking map versus (a) phase (b) resonance frequency (c) normalized field, and (d) normalized carrier density.	36
Figure 2.4 Effects of increasing injection ratio on the frequency response. (a) Locking map showing the bias points used in (b). (b) Frequency responses of the different injection ratio bias points, clearly showing that resonance frequency increases with increasing injection ratio. (c) Pole/zero diagram of the bias points. (d) Blow-up of the poles from (c).	39
Figure 2.5 Locking map showing the bias points for the three regimes of modulation, for $R_{int} = 2$ dB, in Figure 2.6.	42
Figure 2.6 Frequency response and corresponding pole/zero diagrams for the three regimes of modulation: (a) high resonance frequency regime, (b) broadband regime, and (c) high gain regime.	43
Figure 2.7 Theoretical waterfall plots showing frequency response versus detuning, for $R_{int} = 2$ dB. (a) Different frequency responses along the dotted line in Figure 2.5. The responses of the three bias points in Figure 2.5 are shown in their respective colors. (b) Pole/zero diagram corresponding to the same bias points. The bold, black points show the 2 poles of the free-running case. (c) Frequency responses of the three representative regimes, overlaid for comparison, plus the free-running response (black).	46
Figure 2.8 Graphic of method for maximizing bandwidth. The green line corresponds to the response of the 3 rd pole. The red line corresponds to the response of the resonance frequency. The 3-dB point of both lines must meet to maximize the total bandwidth, shown in blue.	56
Figure 2.9 Cavity mode model of injection locking. (a) shows the laser line of the free-running slave laser. (b) When the slave is injection-locked by a positive detuning frequency, the cavity mode shifts to the red side while the locked optical mode shifts to the blue side. The difference between the locked and cavity modes is the resonance frequency enhancement factor, $\Delta\omega_R$. (c) When modulation is swept from DC to high frequencies the cavity mode will resonantly enhance any modulation sideband (dark blue) that appears near it.	60
Figure 2.10 Experimental representation of origin of resonance frequency enhancement. (a) Optical spectrum showing shifting of cavity mode ($f_{cav} - f_{fr} = -23$ GHz) and positively-detuned locked mode ($\Delta f_{inj} = +34$ GHz). Injection-locked	

case is in blue, free-running in light green. (b) Modulation frequency response showing resonance peak enhanced to 57 GHz.....	62
Figure 2.11 Optical spectra evolution across the locking range, with fixed injection ratio. (a) shows a surface plot of the optical spectrum of master and slave over a continuous range of detuning frequencies. Darker signifies higher power. (b) the experimental locking map, where the red vertical line signifies the range of bias points that correspond to the spectra in (a). (c) sample optical spectra at the four labeled points in (a). (1) shows the master on the red side of the unlocked slave. (2) and (3) show the slave locked to the master, since the master is within the locking range. (4) shows the master on the blue side of the unlocked slave.	64
Figure 2.12 Phasor model of injection locking shows how steady-state is reached. (a) shows the evolution of the slave laser if lasing at its cavity mode. Since it is not locked, it rotates at a frequency of $\Delta\omega_R$. When locked to the master laser (b), the phasor is static by the addition of three vectors: 1) Phasor rotates by difference between master and slave frequencies. 2) Injected master light adds a real component. 3) Amplitude decreases due to reduced gain.....	68
Figure 3.1 Injection locking of various laser structures: (a) VCSEL (b) Fabry-Perot (c) DFB.	70
Figure 3.2 (a) Lumped-element model. (b) Distributed model showing the forward, reverse and injected power intensity along the cavity length.	72
Figure 3.3 Ratio of internal and external injection ratios for different mirror reflectivities.....	77
Figure 3.4 Maximum resonance frequency enhancement versus external injection ratio for a typical EEL and VCSEL.	80
Figure 3.5 Right axis: mirror reflectivity for a laser whose optimum $\alpha_m = 30 \text{ cm}^{-1}$ (corresponding to a minimized current for $P_o = 2\text{mW}$, for typical laser parameters). Left axis: maximum resonance frequency enhancement at $R_{ext} = 0\text{dB}$ for this mirror loss.....	83
Figure 3.6 Graph of maximum resonance frequency enhancement for different optimized α_m	83
Figure 3.7 Comparison of theory with experimental data for maximum resonance frequency enhancement.	86
Figure 4.1 Basic heterodyne detection principle. (a) Schematic of heterodyne detection system. (b) Optical spectrum, showing the LO line at f_{LO} (red), DUT line at f_s (tall, blue), and its modulation sidebands at $f_s \pm f_m$ (2 short, blue). (c) Electrical spectrum, showing the beating between DUT and LO fundamental lines (Δf); the direct detection term (f_m) was created by the beating between the DUT and its sidebands; and the down-converted heterodyne term ($f_m - \Delta f$), created by the beating between the LO and the modulation sideband closest to it.....	91
Figure 4.2 Heterodyne and direct detection comparison.	96

Figure 4.3 Heterodyne detection of frequency response from 0-75 GHz. (a) Optical spectrum of the injection-locked laser, showing the position of the local oscillator. (b) Frequency response, consisting of the two concatenated parts.....	97
Figure 4.4 Measurement that separates and shows the asymmetry of modulation sidebands. (a) Frequency domain representation of the separation. (b) Frequency response of an injection-locked laser at different injection ratios and detuning frequencies.....	99
Figure 5.1 Laser structure of the 1550 nm CMBH DFB laser [37]. (a) Isometric view of the laser chip, showing top contacts, ridge waveguide, and output facet. (b) Blow-up of laser facet, showing epitaxial growth layers and CMBH structure.....	105
Figure 5.2 Frequency response of the free-running slave laser at 29 mA.....	106
Figure 5.3 Small-signal circuit model of the laser, showing relevant components. The RC in the active region (shown, but unlabeled) was neglected.....	107
Figure 5.4 Experimental setup with optional heterodyne detection.....	109
Figure 5.5 Experimental frequency response versus detuning, for $R_{ext} = 8$ dB. (a) Waterfall plot showing all frequency responses across the locking range, plus the resonance frequency evolution. Selected frequency response curves showing (b) maximum resonance frequency (c) largest broadband response (d) highest LF gain.....	111
Figure 5.6 Frequency response vs. injection ratio, Δf_{inj} is fixed at +15 GHz. (a) Optical spectra with optical frequency relative to free-running frequency. Locked mode shown as highest power horizontal line (+15 GHz). Cavity mode is shown as 2 nd highest horizontal line (starting at -5 GHz on l.h.s.). Four-wave mixing terms are shown above and below locked and cavity mode, respectively. (b) Waterfall plot of frequency responses. Resonance frequency is shown to increase with increasing injection ratio.....	113
Figure 5.7 Frequency response vs. detuning frequency. R_{ext} is fixed at +8 dB. (a) Optical spectra with optical frequency relative to free-running frequency. Locked, cavity, and four-wave mixing (4WM) modes are labeled. The locking boundary is marked at $\Delta f_{inj} = -37$ and 0 GHz. (b) Waterfall plot of frequency responses. Resonance frequency is shown to increase and damping is shown to decrease with increasing frequency response.....	115
Figure 5.8 Experimental mapping of resonance frequency versus locking range.....	116
Figure 5.9 Experimental frequency response curve showing resonance frequencies of 59 GHz and 72 GHz. $R_{ext} = +16$ dB.....	118
Figure 5.10 Experimental frequency response curve showing a broadband, 3-dB response of 44 GHz. $R_{ext} = +18$ dB, $\Delta f_{inj} = -60.5$ GHz.....	120
Figure 5.11 Optical spectrum of an injection-locked laser biased such that the cavity mode is 100 GHz away from the locked mode. This shows potential for >100 GHz resonance frequency lasers. $P_{ML} = 16$ dBm, $P_{SL} = 1.4$ dBm, $\Delta f_{inj} = +94$ GHz.	122

Figure 6.1 (a) Schematic of typical injection locking system with direct modulation on the slave current, resulting in AM+FM output. (b) Schematic of injection locking system with master laser modulation. If external modulation is applied, AM or FM (PM) can be applied separately. Choosing either modulation will result in both AM and FM on the slave output.	125
Figure 6.2 Schematic of experimental setup for measuring FM-to-AM conversion and direct modulation. One of two modes can be switched from the output of the network analyzer: A. will create frequency modulation on the master while B. will directly modulate the slave. VOA = variable optical attenuator, Pol. = polarization controller, PM = phase modulator.	125
Figure 6.3 Slave AM due to different modulation sources. FM-to-AM conversion and direct modulation are shown.	127
Figure 6.4 Experimental FM-to-AM conversion for different injection ratios.	128
Figure 6.5 Direct modulation for various injection ratios: (a) schematic (b) frequency response. Driving source: current modulation on slave. Measured output: optical AM on slave.	134
Figure 6.6 RAM suppression for various injection ratios: (a) schematic (b) frequency response. Driving source: optical AM on master. Measured output: optical AM on slave.	136
Figure 6.7 FM-to-AM conversion for various injection ratios: (a) schematic (b) frequency response. Driving source: optical FM on master. Measured output: optical AM on slave.	137
Figure 6.8 Theoretical FM-to-AM conversion for various injection ratios.	138
Figure 6.9 FM Efficiency for various injection ratios: (a) schematic (b) frequency response. Driving source: optical FM on master. Measured output: optical FM on slave.	139
Figure 7.1 Schematic of optoelectronic oscillator. The noise is dominated by the RF amplifier.	142
Figure 7.2 (a) Schematic of OIL-OEO. The system will have enough narrow-band gain to remove the need for RF amplifiers. Note also the high potential frequency of oscillation. (b) Experimental frequency response showing ultra-high resonance and gain at 48 GHz.	144

LIST OF TABLES

Table 1.1 Limitations of directly-modulated lasers and improvements by optical injection locking.....	2
Table 2.1 Injection-locked laser parameters. (*) derived via (3.10).....	30
Table 3.1 Comparison of coupling rates of VCSELs and EELs.....	78
Table 5.1 Survey of state-of-the-art records in high-speed laser modulation.....	103
Table 6.1 Laser parameters used in this chapter.....	133

ACKNOWLEDGEMENT

I would foremost like to thank my advisor, Professor Ming Wu, for his consummate intellect in academic and philosophical matters. His patience and faith in my abilities have inspired me on countless occasions. Without his guidance, this work would not have come to fruition.

With that, I would like to thank the other members of the Integrated Photonics Lab for their input and companionship on this long journey. Specifically, I would like to thank Hyuk-Kee Sung and Thomas Jung for countless hours of brainstorming and discussion. In other groups, I would like to thank Professor Connie Chang-Hasnain, Wendy Zhao, and Rod Tucker for many great suggestions and different perspectives on injection locking matters.

Moving back in time, I have to thank my Master's thesis advisor, Professor Rajeev Ram at MIT. His brilliance in and out of the lab has served as a constant role model for me to look up to. I must say the same about every member of his lab.

On more personal grounds, I have to thank my friends for make life more balanced and complete, from the numerous climbing and backpacking epics to quaint dinner parties and bar nights.

I would like to thank my significant other, Blisseth, for having the patience and understanding during those times when I needed to be focused and out of harmony.

Last and most importantly of all, I thank my family. Without them, life would be an aimless wander without direction – they have served as a basis for everything I do and everything I am today. They are the roots that have anchored the tree of my life.

ABSTRACT

High-Speed Modulation of Optical Injection-Locked Semiconductor Lasers

by

Erwin K. Lau

Doctor of Philosophy in Engineering – Electrical Engineering and Computer Sciences

University of California, Berkeley

Professor Ming C. Wu, Chair

Semiconductor lasers are an integral part of high-speed telecommunications. The push for higher modulation frequencies, thereby allowing greater data rates, has motivated the scientific community for several decades. However, the maximum speed of directly-modulated semiconductor lasers has plateaued as the field reaches a mature state. Recently, optical injection locking has been proven to enhance the bandwidth and resonance frequency of directly-modulated semiconductor lasers. The injection locking technique allows the lasers to exceed their fundamental modulation speed limit, allowing for greater communication speeds. However, although the resonance frequency has been predictably linked to the injection locking parameters, the bandwidth enhancement has not been reliably correlated to the resonance frequency, unlike typical directly-modulated lasers.

In this dissertation, we first develop theoretical insight into the nature of resonance frequency and bandwidth enhancement, attempting to correlate the two. We describe the

fundamental limit of resonance frequency enhancement and generalize these results to oscillators of all kinds. Using these theoretical trends, we optimized the injection locking performance of 1550 nm distributed feedback lasers. We report a high-speed resonance frequency of 72 GHz and a 3-dB modulation bandwidth of 44 GHz. These are the highest reported resonance frequency and 3-dB bandwidth of any directly-modulated semiconductor laser, respectively.

Direct measurement of laser frequency response is often limited by the bandwidth of photodetectors and network analyzers. In order to measure frequencies above our detection equipment limit (50 GHz), we develop a new optical heterodyne technique that can detect arbitrarily-high modulation frequencies. This technique, in contrast to previous heterodyne methods, does not require stable frequency solid-state lasers and can be used to test telecom-wavelength lasers.

Finally, we discuss a new modulation technique, where the master is modulated rather than the slave. This technique has many applications, such as residual amplitude modulation reduction, frequency modulation regeneration, and frequency discrimination. We demonstrate the latter experimentally, achieving 0.88 mW/GHz frequency-to-amplitude conversion. Additionally, we develop the basis for the theory that governs these techniques and find the theory in good agreement with our experiments.

Professor Ming C. Wu, Chair

Chapter 1 Introduction

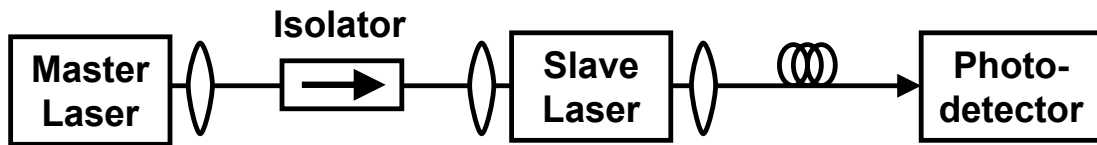
Directly-modulated (DM) semiconductor lasers are compact, low-cost transmitters for both digital and analog photonic communication systems. However, their use in high performance analog photonic systems is limited by several performance issues, listed in Table 1.1. As shown in this table, optical injection locking (OIL) systems can improve a host of fundamental limitations of directly-modulated lasers and links: single mode performance and side-mode suppression [1], enhanced bandwidth and relaxation oscillation frequency [2-4], suppressed nonlinear distortion [5, 6], reduced relative intensity noise [6-10], reduced chirp [11-13], increased link gain [14], and near-single-sideband modulation [15]. In addition to improving the performance of optical communication links, injection-locked laser systems have many other unique properties. These properties make OIL attractive for applications such as optical frequency reference generation [16], phased-array radars [17], phase modulation [18], and optical signal processing [19], amongst others.

Fundamental limits		Benefit from OIL
Laser	Mode partition noise (Fabry-Perot laser)	Single-mode with side-mode suppression [1]
	Relaxation oscillation frequency	Enhanced relaxation oscillation frequency [2-4]
	Non-linear electron-photon coupling	Reduced nonlinearities [5, 6]
	Amplified spontaneous emission noise	Reduced RIN [6-10]
	Wavelength chirp (non-zero α parameter)	Reduced chirp [11-13]
Link	Differential quantum efficiency < 1	Increased link gain [14]
	Double-sideband modulation	Near-single-sideband modulation [15]

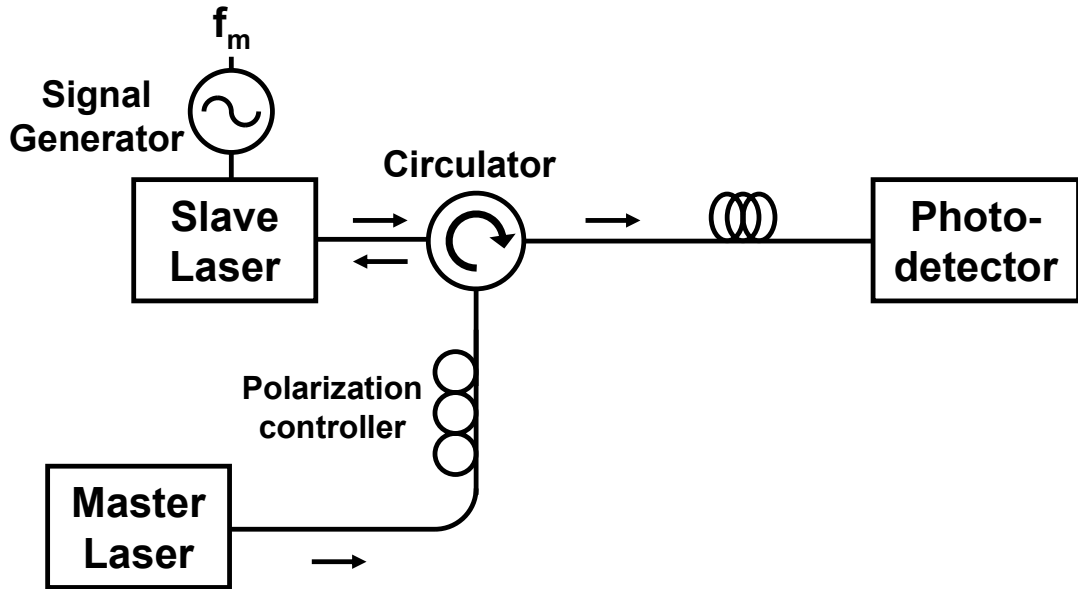
Table 1.1 Limitations of directly-modulated lasers and improvements by optical injection locking.

Figure 1.1(a) shows an experimental schematic of an injection-locked laser system. The light of a master laser is injected into a slave laser. The light from the slave is the useful output of the system. An isolator is placed between master and slave to eliminate light coupling back to the master. There are two possible configurations of injection locking, depending on the choice of outputs of the slave. In transmission-style injection locking (Figure 1.1(a)), the injected master light enters one slave laser facet and the output is taken from the other facet. This necessitates two coupling systems on the slave laser alone. To simplify the system, a reflection-style setup is used (Figure 1.1(b)). The output is taken at the same facet as the input of the injected light. An optical circulator is used to ensure only the output beam goes to the photodetector. The reflection-style system output is susceptible to non-injected master light coupling to the output when the incident master light reflects off the slave laser facet. This is important only in the strong injection regime and not an issue for transmission-style implementations. It can be minimized by applying anti-reflection coating to the slave facet. The coupling can be

done via free-space optics, with lenses, as shown between the master and slave laser in Figure 1.1(a), or via fiber, as shown between the slave and photodetector. Additionally, in a fiber system, a polarization controller is necessary to ensure the master and slave polarizations are matched. Figure 1.1(b) also shows that direct modulation is typically applied to the slave laser.



(a)



(b)

Figure 1.1 Schematic of optical injection-locked laser system: (a) transmission-style (b) reflection-style.

When injection-locked, the slave's lasing wavelength is locked to the master's. Figure 1.2(a) shows the spectrum of a free-running single-mode (SM) laser. Light from the master is then injected into the slave, not necessarily at the same wavelength. Figure

1.2(b) shows both original slave mode and injected master light, before locking. Finally, when the dynamics of the laser settle, the slave wavelength is pulled towards the master wavelength, until it equals that of the master, locking both its frequency and phase. Now, if the master laser frequency is changed, the slave will track this frequency until the difference between master and free-running frequencies (detuning frequency, Δf_{inj}) becomes too large. At this point, the slave unlocks from the master and lases at its natural wavelength. The span of frequencies that result in a locked state is the locking range. The locking range typically becomes larger as the ratio of master and slave optical powers defined as the injection ratio, R , increases. The relative phase between the slave and master (ϕ) is fixed, though its value depends on the detuning frequency and the injection ratio (see Section 2.3.1).

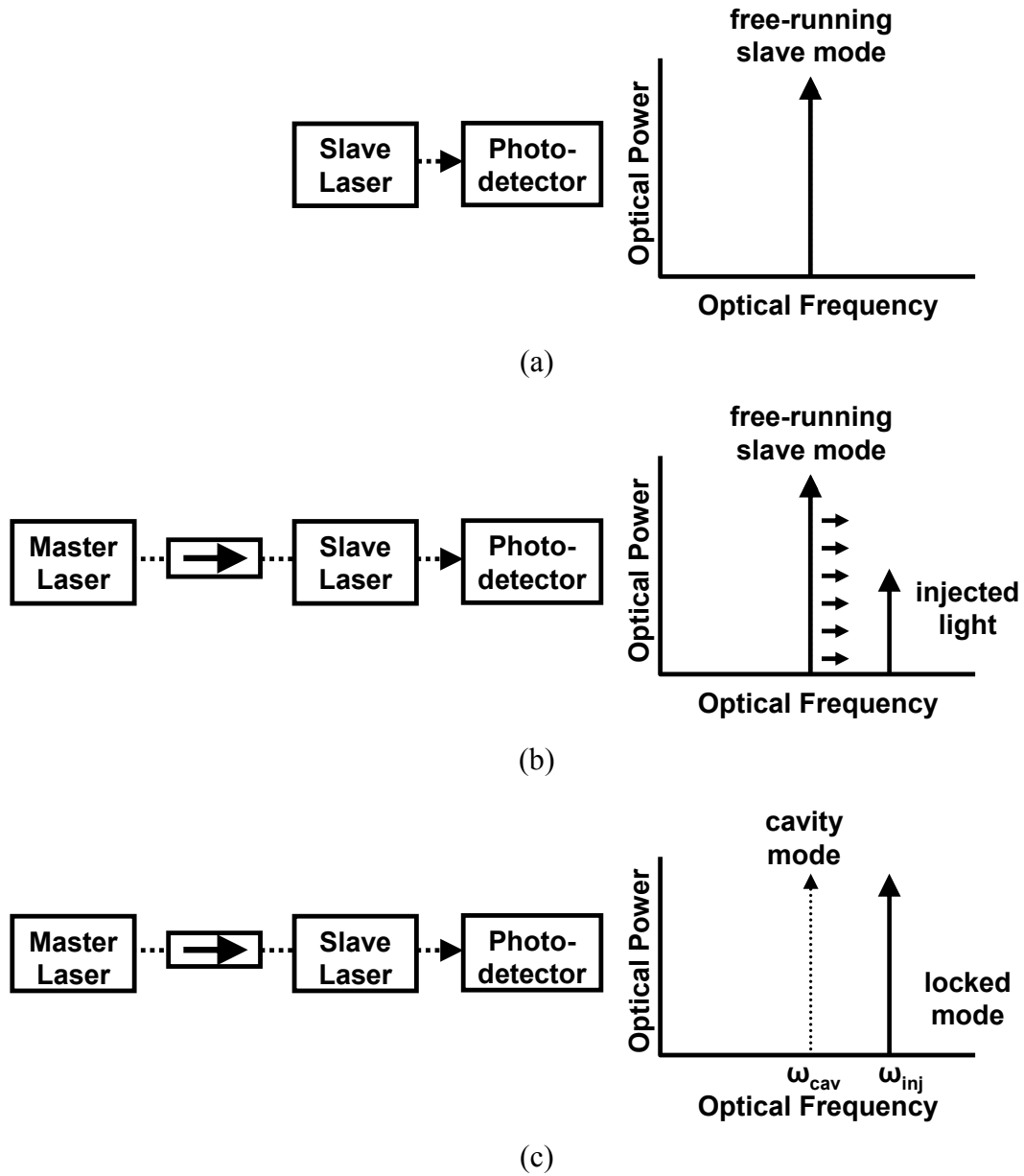


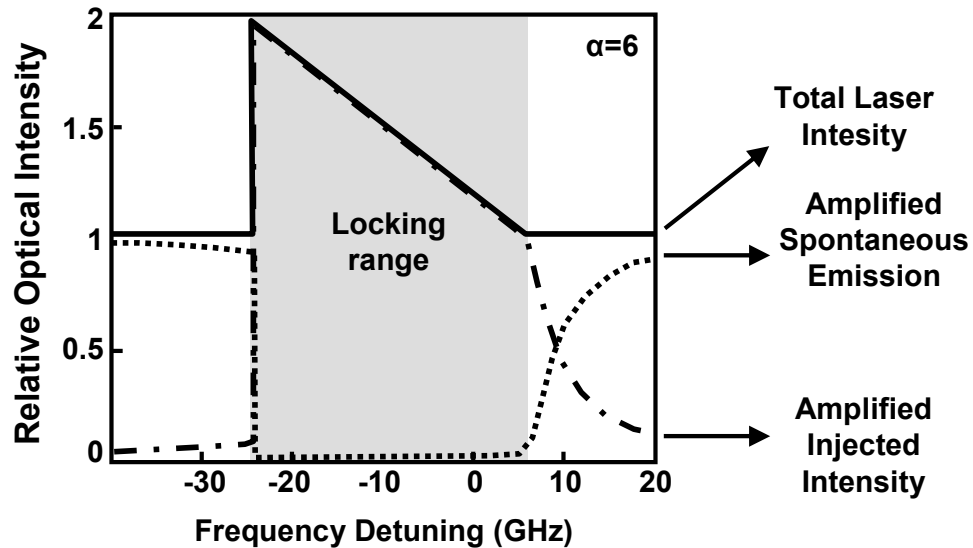
Figure 1.2 Conceptual diagram of injection locking: (a) free-running laser (b) slave with injected light, before locking (c) locked slave laser.

A few theoretical models have been developed that explain the basic physical mechanism of injection locking. A graphical phasor model will be described in Section 2.8. A gain competition model is shown in Figure 1.3. The bottom diagram shows the locking range in gray. Outside the locking range, the laser power is dominated by

amplified spontaneous emission (ASE) in the slave cavity. As in a free-running laser, the ASE of the cavity mode captures the gain and dominates the slave laser power. With external injection, the injected light competes with the spontaneous emission of the slave laser to determine the dominant lasing mode. Within the locking range, the external injection dominates over the spontaneous emission of the slave's natural lasing mode. The injection mode then captures the gain of the laser and the amplified spontaneous emission from the other modes is suppressed.



(a)



(b)

Figure 1.3 Physical gain competition model of injection locking. (a) Illustration of gain model. (b) Detuning dependence on optical intensity, showing competition of ASE and amplified injected intensity, after Henry [2].

1.2 History

Perhaps the first observation of injection locking emerged as a thought experiment of the scientist Christiaan Huygens (1629-1695) [20]. Huygens, inventor of the pendulum clock, observed that the pendulums on two clocks mounted on the same wall would eventually lock frequencies, and swing with opposing phase (Figure 1.4). He reasoned that the pendulums must somehow affect each other. He eventually concluded that they were coupled by emitting vibrations passed through the wall that supported them. One pendulum sent vibrations that traveled through the wall and “injected” small perturbations to the other pendulum, eventually “locking” the frequency and phase of the two pendulums together.

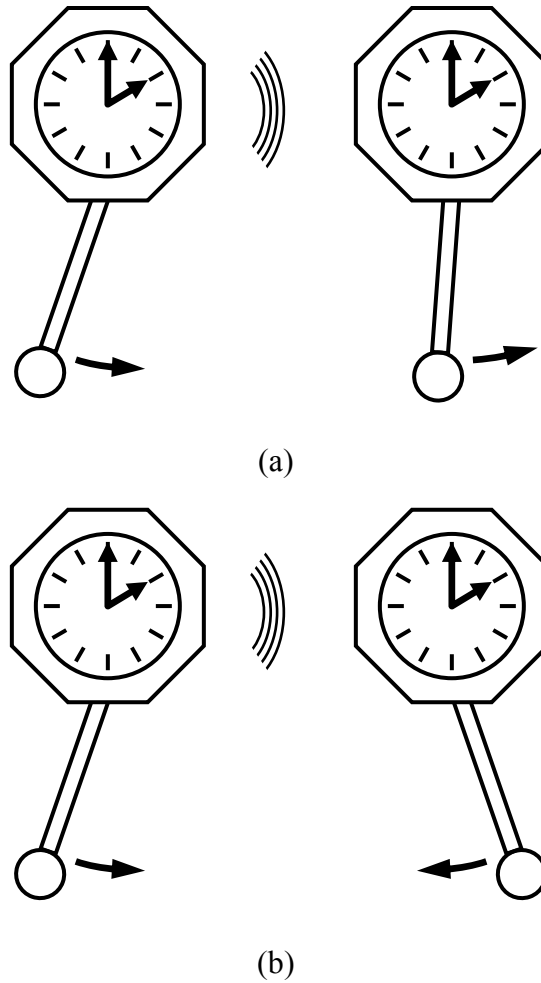


Figure 1.4 Huygens thought experiment showing injection locking of wall-coupled pendulum clocks. (a) Pendulums are out of phase and frequency, but coupled by wall vibrations. (b) Over time, pendulums eventually lock in frequency with opposite phase.

Huygens’s thought experiment introduced the concept of injection locking to the world, and involved mechanical systems. However, the first published work on injection locking was on electrical systems, by R. Adler [21] in 1946. Adler injection-locked an electrical oscillator with an external frequency source. The “free-running” oscillator (without injection of an external source) will oscillate at its natural frequency, ω_0 . Adler showed that when an external signal at frequency ω_{inj} is injected into the oscillator, the

circuit will now oscillate at the injected frequency, provided ω_{inj} is sufficiently close to the natural oscillator frequency, ω_0 .

Finally, twenty years later, injection locking was applied to light, when a source for coherent light was invented in the form of the laser. In 1965, Pantell expanded Adler's injection locking theory to include lasers [22]. A year later, Stover and Steier demonstrated the first injection-locked laser using two red HeNe lasers [23]. Here, the laser cavity acts as the oscillator and ω_0 is the free-running laser frequency.

Injection locking work slowed for the next decade. Lasers were themselves incipient and new applications and materials were just being developed. The 1970's saw optical injection locking applied to different laser systems, such as CO₂ lasers in Buczek *et al.*'s work in 1972 [24]. The 70's also saw the development of low-loss optical fiber and the maturation of semiconductor lasers, as well as optical communications schemes such as direct and coherent detection. Injection locking again came into the spotlight in 1980 when the first demonstration of injection locking in semiconductor lasers was reported by Kobayashi and Kimura using GaAs lasers [25]. Since injection locking can pull two lasers to the same wavelength, they made attractive local oscillators in coherent detection systems [26], then one of the leading methods of long-distance optical communications (before the popularization of optical amplifiers in the early 90's).

The 80's saw rapid development of new phenomenon and applications for OIL systems. In 1982, Kobayashi and Kimura demonstrated optical phase modulation by direct modulation of the slave laser current [18]. When injection-locked to a stable master laser, the frequency of the slave is fixed. Changing the slave bias current will cause its locked conditions to change, thus causing the phase difference (ϕ) between master and

slave to shift. This phase shifting by current modulation provided an attractive and simple method for achieving phase-shift key (PSK) modulation for coherent detection systems. In the same year, Kobayashi and Kimura demonstrated the effects of injecting modulated light into the slave. The master was frequency modulated and injected at weak injection ratios, much lower than the DC power of the slave. The FM was preserved on the slave output while observing up to 30 dB power gain due to the much higher slave output power [27]. Later, Kasapi *et al.* would use this to develop a sub-shot-noise FM spectroscopy technique [28]. In 1989, Esman *et al.* used a similar method of phase modulation, but applied to injection locking of electrical oscillators [29]. They directly modulated a laser to create sidebands and detected the heterodyne beat with a microwave oscillator circuit. The heterodyne beat locked the oscillator and the microwave phase was controlled by changing the laser diode bias. Similar work was done in a pure electrical domain, but with the wide-spread popularization of optical fiber, this technique allowed for an easy distribution method for frequency references in phased array radar [17].

Coherent optical communications would eventually be eclipsed by the advent of the EDFA in the late 80's, making extremely long-haul direct-detection fiber links possible. In the simultaneously developing field of direct detection, OIL made its impact as well. Several groups [12, 13, 30] in the mid-80's demonstrated record bit rate-distance (B-L) products, pushing the limits of long-haul optical communications. In 1984, Lin and Mengel found that OIL reduces the frequency chirp in direct amplitude-modulated lasers by holding the slave frequency constant to the master frequency [11]. Olsson *et al.* demonstrated this reduced chirp by reporting a then-record 165 Gbit/s-km B-L product [13]. This reduced chirp lessens the linewidth broadening thus reducing the effects of

pulse broadening due to fiber dispersion. This allows for longer maximum transmission lengths and a higher B-L product.

Other applications for OIL emerged in the 80's as well. In 1982, Goldberg *et al.* developed a method of optical microwave signal generation [31]. The master laser was modulated at a single frequency, f_M . The slave was then locked to the weak FM sideband rather than the carrier. When the master and slave light were optically combined and detected, the heterodyned frequencies produced a microwave beat note, stronger than direct detection of the modulated master alone. Goldberg also developed variant methods that locked two slaves to different modulation sidebands (3rd order), resulting in frequency multiplication of six to give 35-GHz signals [16]. Applications include distribution of microwave references, frequency multiplexing, and locking of microwave oscillators (see Section 1.2.4).

The seminal theoretical works on injection locking were done mostly in the 1980's, as applications were simultaneously developed. In 1982, Lang [32] published the first definitive theoretical analysis of OIL lasers, including the three OIL laser master rate equations (see Section 2.1). He was the first to note the effect on the refractive index of the slave laser. This resulted in the discovery of an asymmetric locking range and the unstable locking regime (see Figure 2.1 and (2.20)). Henry [2] also published rate equations based on Lang's work, formalizing Lang's theory with Henry's linewidth enhancement factor, α . As shown in Section 2.6.1, Henry also derived an approximate formula for the resonance frequency of OIL lasers. He first discovered this important phenomenon but perhaps did not appreciate its significance until Simpson [4] and Meng [33] in the mid- to late-90's showed the enhancement of resonance frequency and

modulation bandwidth. In 1985, Mogensen *et al.* published several works, developing a set of master rate equations with a Langevin noise treatment [34-36]. They developed the theory of maximum phase tuning of ϕ to less than $\pm\pi$ [36]. Also, they used the Langevin formulation to derive the FM noise for OIL lasers, finding that the FM noise of the slave evolves to look like that of the master as the injection ratio increases, thus the slave laser linewidth can be suppressed to that of the master [35].

As we have seen, optical injection locking bestows many attractive improvements to the free-running slave laser. However, the 90's then brought about the discovery of three of the most significant benefits of OIL systems: noise suppression, reduced nonlinear distortions, and bandwidth enhancement; the latter effect will be discussed in greater detail in this thesis.

1.2.2 Resonance Frequency Enhancement

Typically, the bandwidth of a laser is proportional to the resonance frequency, or relaxation oscillation of a laser. It has been shown that the resonance frequency of the laser can be enhanced several factors by OIL [37-41]. Figure 1.5 shows experimental evidence of this effect. However, as can be observed in this figure, the 3-dB bandwidth is no longer directly proportional to the resonance frequency and cannot be fully explained by laser parasitics.

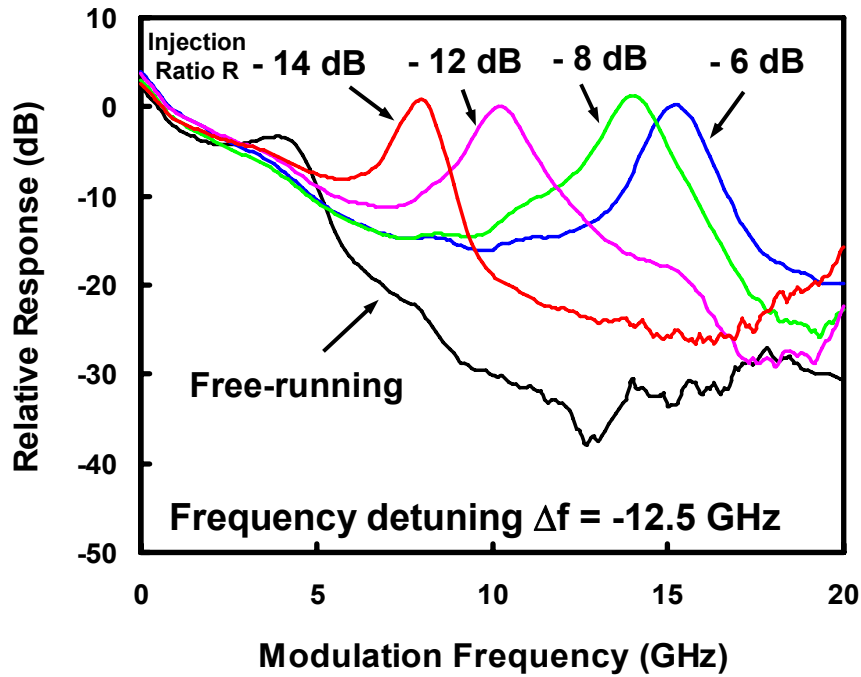


Figure 1.5 Frequency response showing resonance frequency enhancement via OIL [33]. The resonance frequency is improved with increasing injection ratio.

1.2.3 Reduction of Non-Linear Distortions

Analog links desire highly linear signals. OIL has been shown to improve the linearity [42-44]. Non-linearities are enhanced when the signal is close to the relaxation oscillation of the directly-modulated laser. OIL reduces this non-linearity mainly by shifting the resonance frequency away from the bandwidth of the signal. This is shown in Figure 1.6 [42]. The two tones were set at 2 and 2.1 GHz. The free-running and injection-locked relaxation oscillation frequencies were 4.1 and 13.6 GHz, respectively. The 3rd-order intermodulation distortion (IMD3) term was lowered by 15 dB, hence the spur-free dynamic range (SFDR) was improved by $5 \text{ dB} \cdot \text{MHz}^{2/3}$.

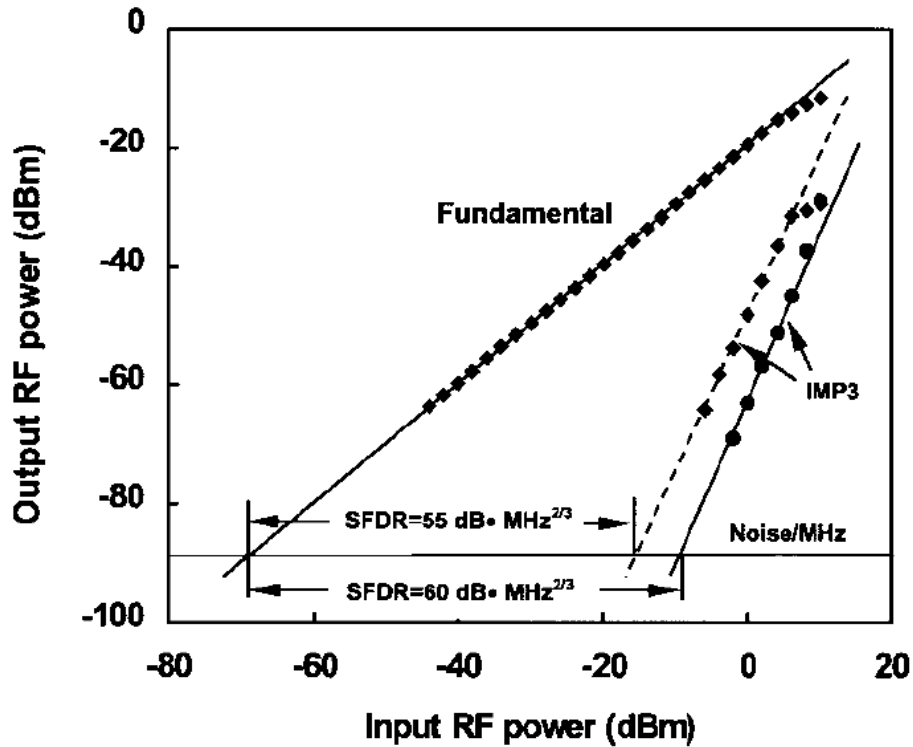


Figure 1.6 SFDR of a directly-modulated DFB laser [42]. Dash/diamonds show the free-running IMP3 power. Solid line/circles show the injection-locked IMP3 power. SFDR improvement was shown to be $5 \text{ dB}\cdot\text{MHz}^{2/3}$.

1.2.4 RIN Reduction

An additional figure-of-merit in improving linearity in links is to reduce the noise floor. In Figure 1.6, the SFDR is calculated as the dB between fundamental and IMD3 tones, along the noise floor level: the lower the noise floor, the higher the SFDR. Once again, injection locking offers a reduction in the relative intensity noise from the free-running level [6, 8-10, 35, 45, 46]. It is known that the RIN spectrum peak coincides with that of the laser's relaxation oscillation. It is no different when injection-locked; the RIN peak is simultaneously enhanced with the resonance. This is shown in Figure 1.7. The RIN around the free-running resonance ($\sim 6 \text{ GHz}$) is effectively reduced since the peak has been shifted to much higher frequencies. The simultaneous reduction of RIN and

non-linear distortion is practically implemented in the first application described in the next section.

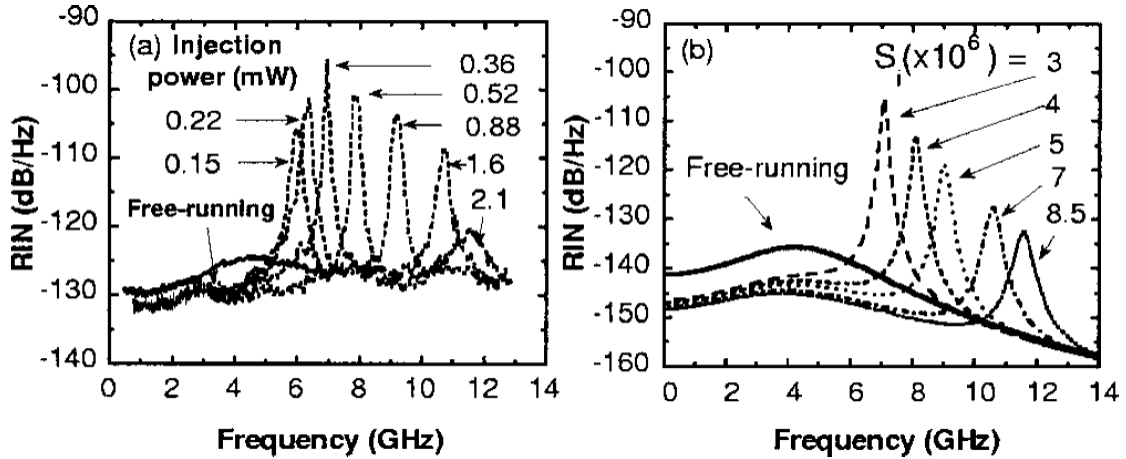


Figure 1.7 Experimental (left) and theoretical (right) RIN spectra for free-running and various injection levels and detuning frequencies [45]. The RIN peak at free-running was pushed to higher frequencies, thereby reducing the RIN near the free-running relaxation oscillation.

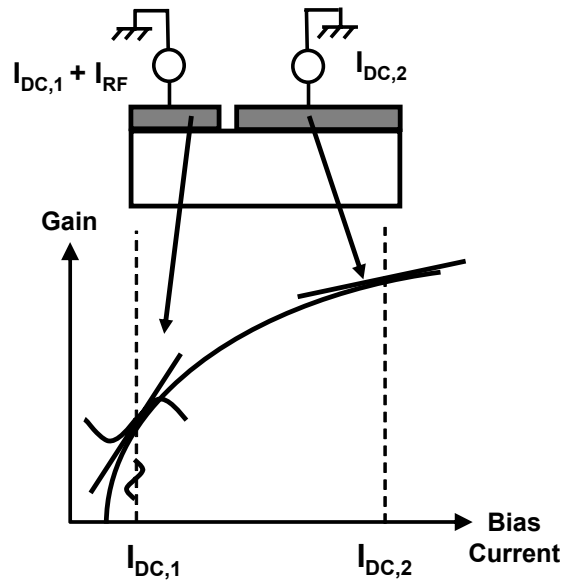
1.3 Applications

Once the groundwork of physical understanding and phenomenon was developed, greater emphasis was devoted to developing applications for injection locking. A sampling of some modern OIL applications is listed here.

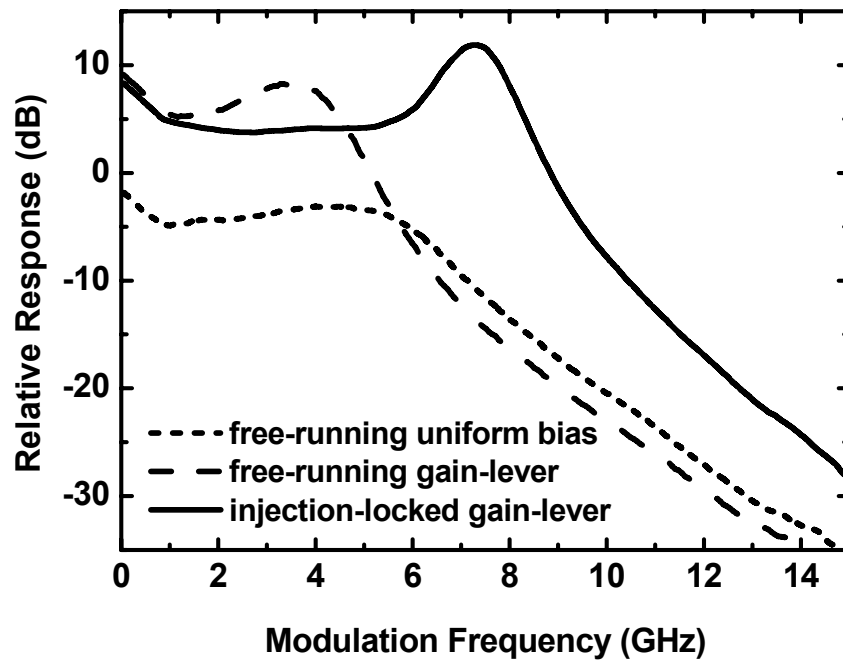
1.3.1 Link Gain Improvement by Gain-Lever OIL

In analog links, there is a desire for higher link gain, since sensitivity and signal-to-noise ratio is proportional to the detected signal. The concept of gain-lever lasers (Figure 1.8(a)) has been shown to increase the DC gain, at the expense of linearity [47, 48]. In a two-section laser, each section is biased at different levels, where the net bias results in a lasing condition. The lower-biased section ($I_{DC,1}$), however, is biased at a lower point on the gain curve and sees a higher differential gain and, therefore, higher modulation

strength. Unfortunately, the higher gain slope coincides with increased non-linearity. Gain-levering is then coupled with injection locking to achieve higher differential gain but increased linearity via OIL [49]. Figure 1.8(b) demonstrates the increased gain (12 dB) with the hybrid system. Additionally, the IMD3 term is reduced by 5 dB, the resonance frequency was increased by three times, and the RIN was reduced by 7 dB, resulting in a SFDR improvement of $12 \text{ dB}\cdot\text{Hz}^{2/3}$, shown in Figure 1.9.



(a)



(b)

Figure 1.8 (a) Concept of gain-levering [47, 48]. (a) Frequency response: dots: free-running laser, uniform bias; dashes: free-running gain-lever laser, showing increased DC gain; solid: injection-locked gain-lever laser, showing both increased DC gain and increased relaxation oscillation [49].

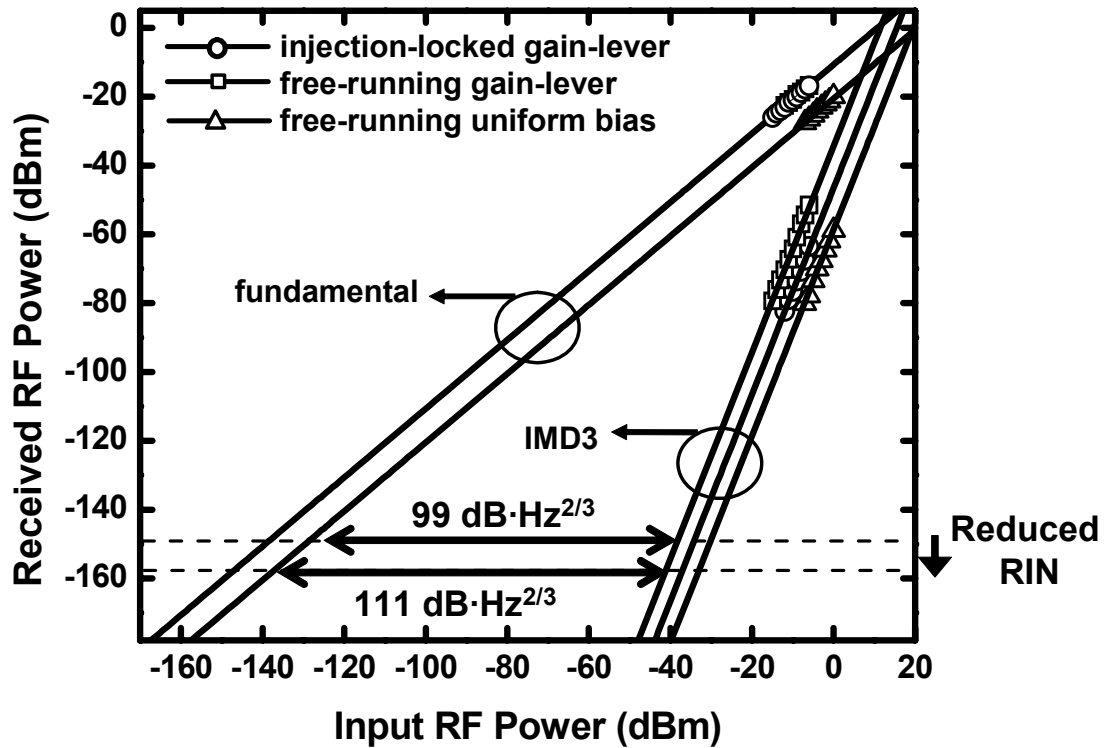
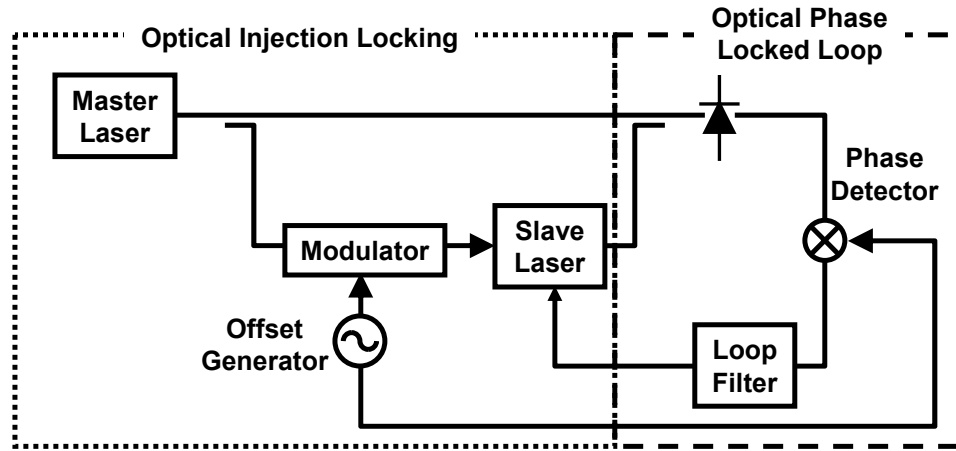


Figure 1.9 Diagram explaining sources of SFDR improvement. The IMD3 term was reduced by 15 dB and the RIN reduced by 7 dB, totaling to a SFDR improvement of $12 \text{ dB}\cdot\text{Hz}^{2/3}$.

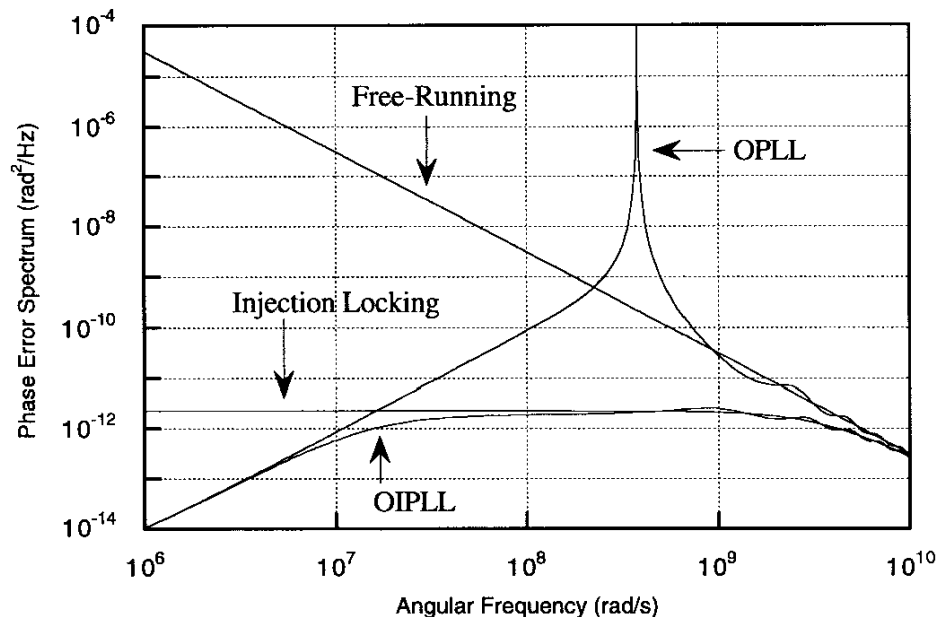
1.3.2 Optical Injection Phase-Locked Loop

In coherent communication, the transmitted signal beats with a DC optical signal, called a local oscillator, at the receiver end. This allows for increased link gain and different formats of modulation, such as the inherently linear phase modulation technique [50]. However, the local oscillator (LO) must be phase-locked to the signal tone in order for these benefits to be realized. Typically, an optical phase-locked loop (OPLL) is implemented [51] (right half of Figure 1.10(a)). However, the laser linewidth noise is too fast for the typical OPLL to reduce. One can also use the injection-locked laser as a frequency locking mechanism, if one locks the LO to the incoming signal [25]. However, the low-frequency phase noise of the OPLL is much more superior. By combining the

techniques, as shown in Figure 1.10(a), one can reap the benefits of both OPLL and OIL, the hybrid implementation being called optical injection phase-locked loop (OIPLL) [52].



(a)



(b)

Figure 1.10 (a) Schematic of optical injection-locked phase-locked loop (OIPLL) [52]. (b) Phase noise spectra for free-running, optical phase locked loop (OPLL), optical injection-locked, and OIPLL systems. The OIL system excels in reducing linewidth of the laser, the OPLL excels in reducing the low-frequency phase noise. The OIPLL system combines the advantages of both.

1.3.3 Injection Locking of Mode-locked Lasers

A mode-locked laser (MLL) can efficiently create many equally-spaced laser lines that are mutually phase coherent. However, in passively mode-locked lasers, the phase noise between modes can be great, due to the passive nature of the mode-locking. As in the previous section, injection locking can be used to create phase locking between an LO and the detectable signal for heterodyne detection. However, if additional sidebands at the width of the mode spacing of the MLL are implied upon the master signal, the modes of the MLL can be synchronized as well, similar to an actively mode-locked laser, reducing the phase noise [53]. Both modulated CW lasers [54] and MLLs [55] have been used as the master laser to synchronize the modes of the slave MLL. One can also use a mode-locked frequency comb to efficiently channelize a wideband RF signal, as shown in Figure 1.11 [56]. The carrier of the wideband RF signal injection locks the frequency comb to the RF signal. Once synchronized, the summation of the signal can be sent to a dispersive medium that will divide the signal into its corresponding channels. Each mode of the frequency comb serves as a carrier signal for its overlapping channel, thus providing the detectors a narrow-band signal to detect.

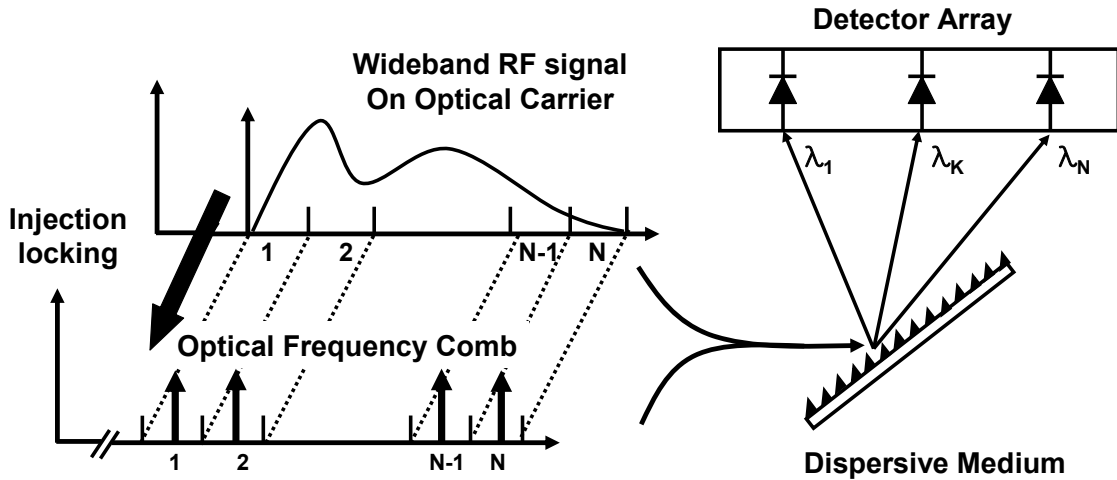
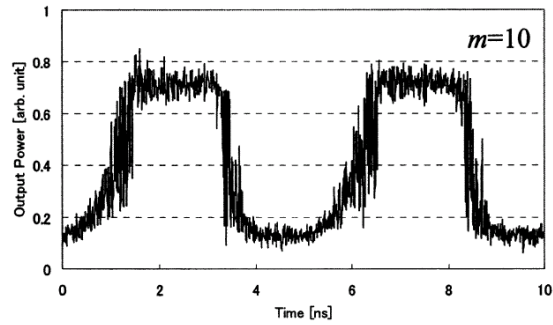
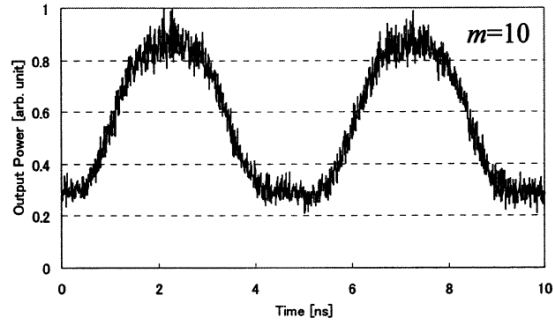
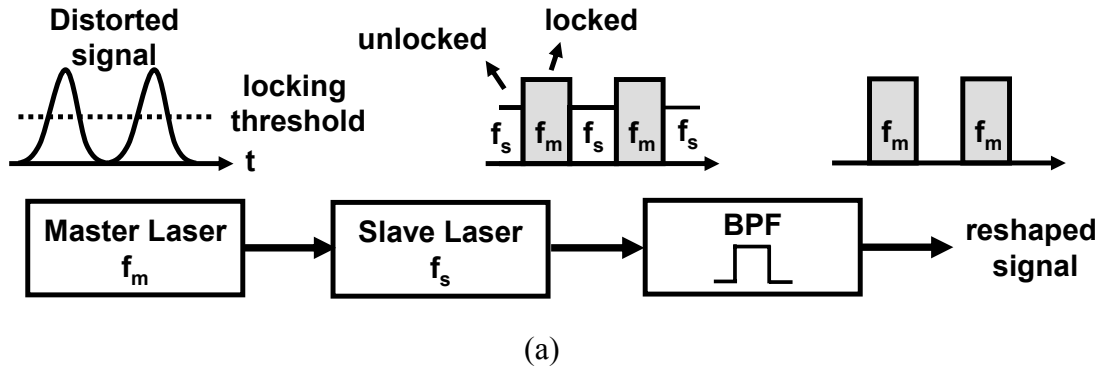


Figure 1.11 Signal channelization schematic. The wideband RF signal is sent to a free-space dispersive grating, which send each channel to its respective detectors. The system ensures synchronization with the desired channel spacing by locking the RF signal’s carrier with a known, stable source.

1.3.4 All-Optical Signal Processing

In long-haul digital communications, dispersion and loss from long distances of the optical fiber cause the pulse train to become smeared, leading to increased bit error rate. Typically, repeaters are used at regular intervals to regenerate and reshape the optical pulse. This requires detection of the signal, conversion to the electrical domain, then regeneration of the pulse into an optical signal. The conversion to the intermediate electrical signal step is undesired, due to its increased complexity and speed limitations. An all-optical solution has been implemented using OIL [57]. In Figure 1.12(a), we see the concept. The master laser is modulated with the digital signal. Over long lengths of fiber, the signal may become degraded. It is then weakly injection-locked into a side-mode of the slave. The high level’s (“1”) power is sufficient to lock the slave to the master frequency (f_m), and the output frequency is then that of the master. However, the low level’s (“0”) power results in an unlocked state, and the free-running frequency (f_s) of

the slave is the output. A band-pass filter (BPF) is used to preserve only the master frequency. Hence, only the master light during the high levels is transmitted (Figure 1.12(b)).



(b)

Figure 1.12 Pulse-reshaping by OIL [57]. (a) shows the concept. (b) shows experimental results. Top graph is the input pulses with noticeable smoothness. Bottom graph is the output pulse, having a more square-like function.

1.3.5 Other Applications

The applications listed here are only a selected group of the many systems in which injection locking has been used. Other applications include millimeter-wave generation up to frequencies of 64 GHz [58], utilizing the technique pioneered by Goldberg, et al. [16]. Recently, un-cooled VCSELs were injection-locked, as inexpensive upstream transmitters for wavelength-division multiplexing passive optical networks (WDM-PON) [59]. Near single-sideband modulation has been developed, using the theory developed in Section 2.7 to reduce the effects of fiber chromatic dispersion [15]. Using optical injection locking, discrete values of locked frequencies have been found to lase at the same intensity [60], contrary to typical laser physics that fault heating and linewidth enhancement for changes in intensity. This may be useful for heterodyne detection schemes or frequency modulation schemes. The enhanced bandwidth and reduced chirp has recently found its way into radio-over-fiber (RoF) [61, 62] and cable-access TV (CATV) [63] applications. Injection locking has also been used distribute carrier signals in phased-array antennas [64].

1.4 Organization of Dissertation

This thesis describes the theory and experimental evidence of high-speed modulation in optical injection-locked lasers. In Chapter 2, we lay down the foundations of the theory of injection-locked lasers. There, we expound on the established theory by developing physical approximations to the complex rate equations. Chapter 3 provides additional theory that describes the fundamental limit of resonance frequency enhancement. In Chapter 4, we then take a break from theory to describe an experimental heterodyne detection technique for measuring extremely high frequency responses. This technique is

then used in Chapter 5, where we describe the experimental validation of the theory developed in the previous chapters and describe two records for highest resonance frequency and bandwidth for semiconductor lasers. Chapter 6 describes a relatively new technique of modulation on the master laser. Finally, we summarize our work in Chapter 7 and describe new applications that have emerged out of our work.

Chapter 2 Rate Equation Theory

2.1 Motivation

In order to push the limit of injection-locked laser systems, it is important to understand the theory that governs its dynamics. The basic theory has been developed in the past by several groups and can describe a wide array of benefits from the injection-locked laser, including RIN reduction [6, 8-10, 35, 45, 46], suppression of non-linear effects [42-44], and resonance frequency enhancement [37-41]. Only recently has the development of ultra-strong injection locking come about. We focus on the effects of ultra-strong injection and its implications to the theory.

2.2 Rate Equations

The most common model for injection-locked lasers uses a set of three differential equations, as published by several authors [2, 3, 32, 36]. The differential equation governing a free-running (non-injection-locked) laser, neglecting spontaneous emission, is:

$$\frac{dE(t)}{dt} = \frac{1}{2} g \Delta N (1 + j\alpha) E(t) \quad (2.1)$$

where $E(t)$ is the complex field, g is the linear gain coefficient, ΔN is the carrier number above threshold, and α is the linewidth enhancement factor [65]. Here, $\Delta N \equiv N(t) - N_{th}$, where N is the carrier number and N_{th} is the threshold carrier number. The differential equation governing the complex field of an injection-locked laser is similar to that of a free-running laser, with the addition of terms describing injection:

$$\frac{dE(t)}{dt} = \frac{1}{2} g \Delta N (1 + j\alpha) E(t) + \kappa A_{inj} - j \Delta \omega_{inj} E(t) \quad (2.2)$$

where $E(t)$ is the slave laser's complex field, κ is the coupling rate, A_{inj} is the magnitude of the injected master field (just inside the facet, see Section 3.2 for further details), and $\Delta \omega_{inj}$ is the detuning frequency between master and slave, defined as $\Delta \omega_{inj} \equiv \omega_{master} - \omega_{slave}$, where ω_{master} and ω_{slave} are the master and slave lasing frequencies, respectively. This model ignores spontaneous emission, assuming it is negligible when sufficiently above threshold. It also ignores Langevin noise terms [35], since noise is not of primary interest here. This equation can be split into the field magnitude and phase by assuming that $E(t) = A(t) \exp(j\phi(t))$, where $A(t)$ and $\phi(t)$ are the slave laser's field magnitude and phase, respectively. This split equation, along with the carrier rate equation, constitute the three differential equations of injection-locked lasers:

$$\frac{dA(t)}{dt} = \frac{1}{2} g [N(t) - N_{th}] A(t) + \kappa A_{inj} \cos \phi(t) \quad (2.3)$$

$$\frac{d\phi(t)}{dt} = \frac{\alpha}{2} g [N(t) - N_{th}] - \kappa \frac{A_{inj}}{A(t)} \sin \phi(t) - \Delta \omega_{inj} \quad (2.4)$$

$$\frac{dN(t)}{dt} = J - \gamma_N N(t) - \left\{ \gamma_p + g [N(t) - N_{th}] \right\} A(t)^2 \quad (2.5)$$

where $N(t)$ is the slave laser's and carrier number. $A(t)$ is normalized as $A^2(t) = S(t)$, where $S(t)$ is the photon number. $\phi(t)$ is the phase difference between master and slave: $\phi(t) \equiv \phi_{slave}(t) - \phi_{master}(t)$. J , γ_N , and γ_P are the current (in electrons/sec.), carrier recombination rate, and photon decay rate, respectively.

2.3 Rate Equation Solutions

2.3.1 Steady State Solutions

It is possible to solve the steady-state solutions to the rate equations (2.3)-(2.5) using time-dependent differential equation solutions such as finite-difference methods. It is desirable, however, to come upon a quick solution without having to solve three coupled, non-linear differential equations. Murakami provides three equations that solve the differential equations in steady-state, one each for the field magnitude, phase, and carrier number [3], defined here as A_0 , ϕ_0 , and N_0 , respectively. Here, we solve them similarly, but with different results. Solving for the free-running field magnitude, A_{fr} , in (2.5), we can set the above-threshold carrier number, $\Delta N_0 \equiv N_0 - N_{th} = 0$, obtaining:

$$A_{fr}^2 = \frac{J - \gamma_N N_{th}}{\gamma_P}. \quad (2.6)$$

Using this and solving for the steady-state values of the injection-locked laser, we obtain:

$$A_0^2 = \frac{A_{fr}^2 - \frac{\gamma_N}{\gamma_P} \Delta N_0}{1 + \frac{g \Delta N_0}{\gamma_P}} \quad (2.7)$$

$$\phi_0 = \sin^{-1} \left\{ -\frac{\Delta \omega_{inj}}{\kappa \sqrt{1 + \alpha^2}} \frac{A_0}{A_{inj}} \right\} - \tan^{-1} \alpha \quad (2.8)$$

$$\Delta N_0 = -\frac{2\kappa}{g} \frac{A_{inj}}{A_0} \cos \phi_0. \quad (2.9)$$

One would choose an injection ratio and detuning frequency, and use the coupled non-linear equations to solve for A_0 , ϕ_0 , and N_0 . However, they tend to be unwieldy due to the coupled nature of their solutions. For example, the field magnitude equation depends on having solved the carrier number, which depends on having solved the phase and magnitude, which then in turn depends on having solved the field magnitude.

Another technique is to assume one of these values and solve the other two based on this. A logical choice would be the phase, because we know the bounds of the phase across the locking range are approximately $\cot^{-1}\alpha$ to $-\pi/2$ (given by Mogensen [36] and described in Section 2.4), from the negative to positive frequency detuning edges, respectively (see Figure 2.1 for illustration). We must assume an injection ratio and use the steady-state equations to solve for A_0 , ΔN_0 , and $\Delta\omega_{inj}$. Knowing ϕ_0 and substituting (2.9) into (2.7) yields:

$$A_0^3 - \left[\frac{2\kappa}{\gamma_P} A_{inj} \cos \phi_0 \right] A_0^2 - A_{fr}^2 A_0 - \frac{\gamma_N}{\gamma_P} \frac{2\kappa}{g} A_{inj} \cos \phi_0 = 0 \quad (2.10)$$

whose roots, A_0 , can be easily solved by a root-solving program. Then, (2.9) solves for ΔN_0 and we rearrange (2.8) to solve for $\Delta\omega_{inj}$:

$$\Delta\omega_{inj} = -\kappa\sqrt{1+\alpha^2} \frac{A_{inj}}{A_0} \sin(\phi_0 + \tan^{-1} \alpha). \quad (2.11)$$

2.3.2 Dynamic Solutions

Equations (2.3)-(2.5) can be linearized by applying a small-signal time-harmonic perturbation around its steady-state solutions:

$$X(t) = X_0 + \Delta X \exp(st) \quad (2.12)$$

where X are the state variables A , ϕ , N , and J . X_0 represents the steady-state values A_0 , ϕ_0 , N_0 and J_0 . ΔX represents the small-signal magnitudes ΔA , $\Delta\phi$, ΔN , and ΔJ . s represents the complex time-harmonic angular frequency. The linearized equations can be placed in matrix form:

$$\begin{bmatrix} m_{AA} + s & m_{A\phi} & m_{AN} \\ m_{\phi A} & m_{\phi\phi} + s & m_{\phi N} \\ m_{NA} & 0 & m_{NN} + s \end{bmatrix} \begin{bmatrix} \Delta A \\ \Delta\phi \\ \Delta N \end{bmatrix} = \begin{bmatrix} 0 \\ 0 \\ \Delta J \end{bmatrix} \quad (2.13)$$

where the matrix terms are:

$$\begin{aligned} m_{AA} &= z \cos \phi_0 \\ m_{A\phi} &= z A_0 \sin \phi_0 \\ m_{AN} &= -\frac{1}{2} g A_0 \\ m_{\phi A} &= -z \sin \phi_0 / A_0 \\ m_{\phi\phi} &= z \cos \phi_0 \\ m_{\phi N} &= -\frac{1}{2} \alpha g \\ m_{NA} &= 2 A_0 (\gamma_P - 2z \cos \phi_0) \\ m_{NN} &= \gamma_N + g A_0^2 \end{aligned} \quad (2.14)$$

where $z \equiv \kappa A_{inj} / A_0$. Each of the matrix terms, m_{XY} , describe the magnitude in which X changes as Y is perturbed. Hence, m_{AN} tells us how much the field changes as a result of a change in the carrier number. Inverting the matrix, the magnitude of the frequency response is then

$$H(s) = \frac{\Delta A}{\Delta I} = M \frac{s - Z}{s^3 + A s^2 + B s + C} \quad (2.15)$$

where

$$\begin{aligned}
A &= m_{AA} + m_{\phi\phi} + m_{NN} \\
B &= m_{AA}m_{\phi\phi} + m_{AA}m_{NN} + m_{\phi\phi}m_{NN} - m_{A\phi}m_{\phi A} - m_{AN}m_{NA} \\
C &= m_{AA}m_{\phi\phi}m_{NN} + m_{A\phi}m_{\phi N}m_{NA} - m_{A\phi}m_{\phi A}m_{NN} - m_{AN}m_{NA}m_{\phi\phi} \\
Z &= (m_{A\phi}m_{\phi N} - m_{AN}m_{\phi\phi})/m_{AN} \\
M &= -m_{AN}
\end{aligned} \tag{2.16}$$

Therefore, the frequency response can be easily determined by (2.15) and its auxiliary equations, (2.16) and (2.14). Table 2.1 lists the typical parameter values used in the simulations in this paper, unless otherwise noted.

Symbol	Value	Units
λ	1550	nm
g	5667	1/s
N_{th}	2.214×10^8	#
α	3	-
J	$3.5 \times J_{th}$	1/s
J_{th}	2.1×10^{17}	1/s
γ_N	1	1/ns
γ_P	333	1/ns
L	500	cm
r	0.3	-
κ	183*	1/ns

Table 2.1 Injection-locked laser parameters. (*) derived via (3.10).

2.4 Locking Map and Stability

Here, we formally describe the stability conditions that delineate the locking range. The first constraint is found in (2.8). A real solution for the phase can only be found if the absolute value of the arcsine term is not greater than unity. Therefore:

$$-\frac{\pi}{2} - \tan^{-1} \alpha \leq \phi \leq \frac{\pi}{2} - \tan^{-1} \alpha . \quad (2.17)$$

The second constraint is found in (2.9). The carrier number must not go above threshold, or there would be an unstable gain. Therefore:

$$-\frac{\pi}{2} \leq \phi . \quad (2.18)$$

Putting (2.17) and (2.18) together, we obtain the phase constraint:

$$-\frac{\pi}{2} \leq \phi \leq \cot^{-1} \alpha \quad (2.19)$$

which, when used in (2.11), yields Mogensen's locking range [36]:

$$-\kappa \sqrt{1 + \alpha^2} \frac{A_{inj}}{A_0} \leq \Delta \omega_{inj} \leq \kappa \frac{A_{inj}}{A_0} . \quad (2.20)$$

The third constraint can be found through the dynamic equation solutions for the frequency response, namely in the determinant of (2.15):

$$D(s) = s^3 + As^2 + Bs + C . \quad (2.21)$$

When the real parts of the roots of the determinant (i.e. poles of the frequency response) become positive, the solution becomes unstable, which equates to a stability check on the region of convergence (R.O.C.). This can be solved by determining the roots computationally. This typically shrinks the locking range on the positive side, and determines the boundary between stable locking and chaos [66].

Finally, we must take into account the fact that at high injection ratios, the steady-state field magnitude can deviate significantly from the free-running value. Experimentally, we can only determine the injection ratio w.r.t. the free-running slave field, A_{fr} . Here, we formally define the internal power injection ratio as the ratio of master

laser power that has entered into the slave cavity over the power of the free-running slave, inside the cavity:

$$R_{\text{int}} = \left(\frac{A_{\text{inj}}}{A_{\text{fr}}} \right)^2. \quad (2.22)$$

The external power injection ratio, namely the injection power before entering the slave cavity over the free-running output power of the slave, is a more empirical value, but we use the internal ratio here to decouple the theory from laser length or mirror reflectivity. The difference between the two will be described in Section 3.2. However, the slave steady-state power, for high injection ratios and negative frequency detuning, can be significantly higher than the free-running value. This translates to a reduced detuning range on the negative detuning frequency side. An illustration of all of these boundaries can be seen in Figure 2.1.

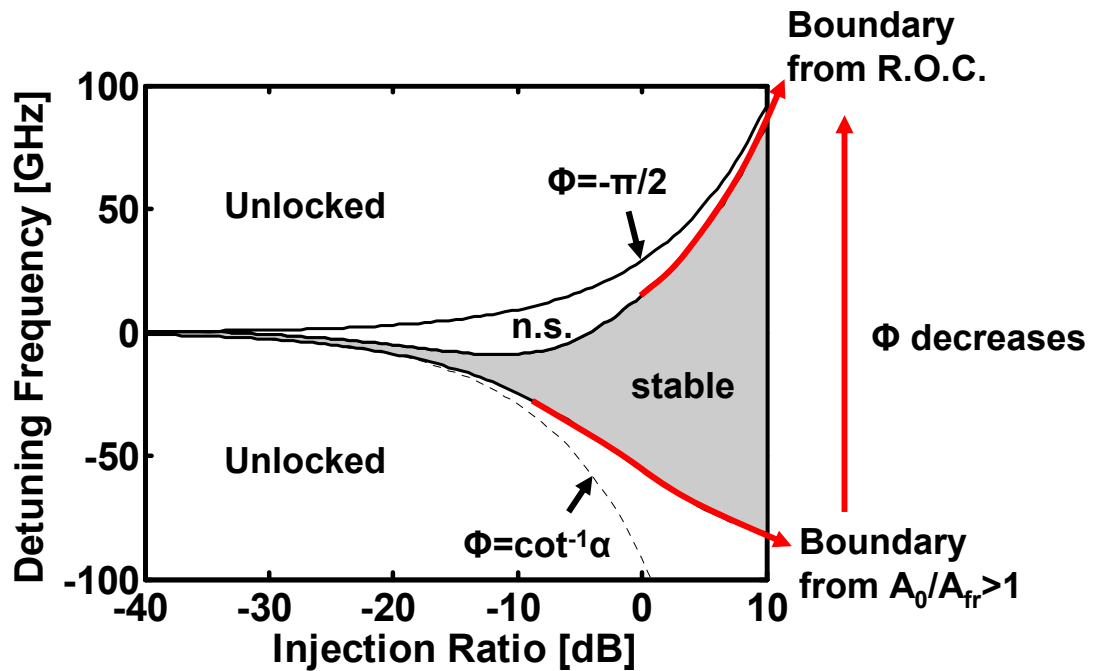


Figure 2.1 Locking range showing the dependence of ϕ across the locking range. n.s. corresponds to the unstable locking regime.

It is most intuitive to choose an injection ratio and detuning frequency and then solve for the other steady-state values, since this is what we do in experiments. However, it is computationally easiest to choose an injection ratio and phase to solve the other steady-state values. Using the steady-state equations (2.9)-(2.11), we can plot the state variables w.r.t. injection ratio and phase, as shown in Figure 2.2. The phase ranges from $-\pi/2$ to $\cot^{-1} \alpha$, which corresponds to the theory. From these graphs, we can see that there are a range of phases at certain injection ratios that correspond to an unstable locking condition determined through the R.O.C. Since the carrier density is the constraint that governs the stable locking region boundary on the negative phase side, through the third constraint described above, we know that the left-hand edge of the carrier density graph must be equal to 1. In Figure 2.3, we plot the same data, except plotted w.r.t. the traditional

locking map variables: injection ratio and detuning frequency. From (a), we see that the positive frequency detuning edge is described by the smallest phase. (b) shows that the resonance frequency increases with detuning and injection ratio. (c) shows that, at the positive edge of the locking range, the field starts at its free-running value and then increases with decreasing detuning and higher injection ratios. (d) shows that the carrier density is at threshold on the positive edge of the detuning range. It gradually decreases as the detuning frequency decreases and/or injection ratio increases. The trends shown in Figure 2.3 are useful when determining the optimized bias point for modulation.

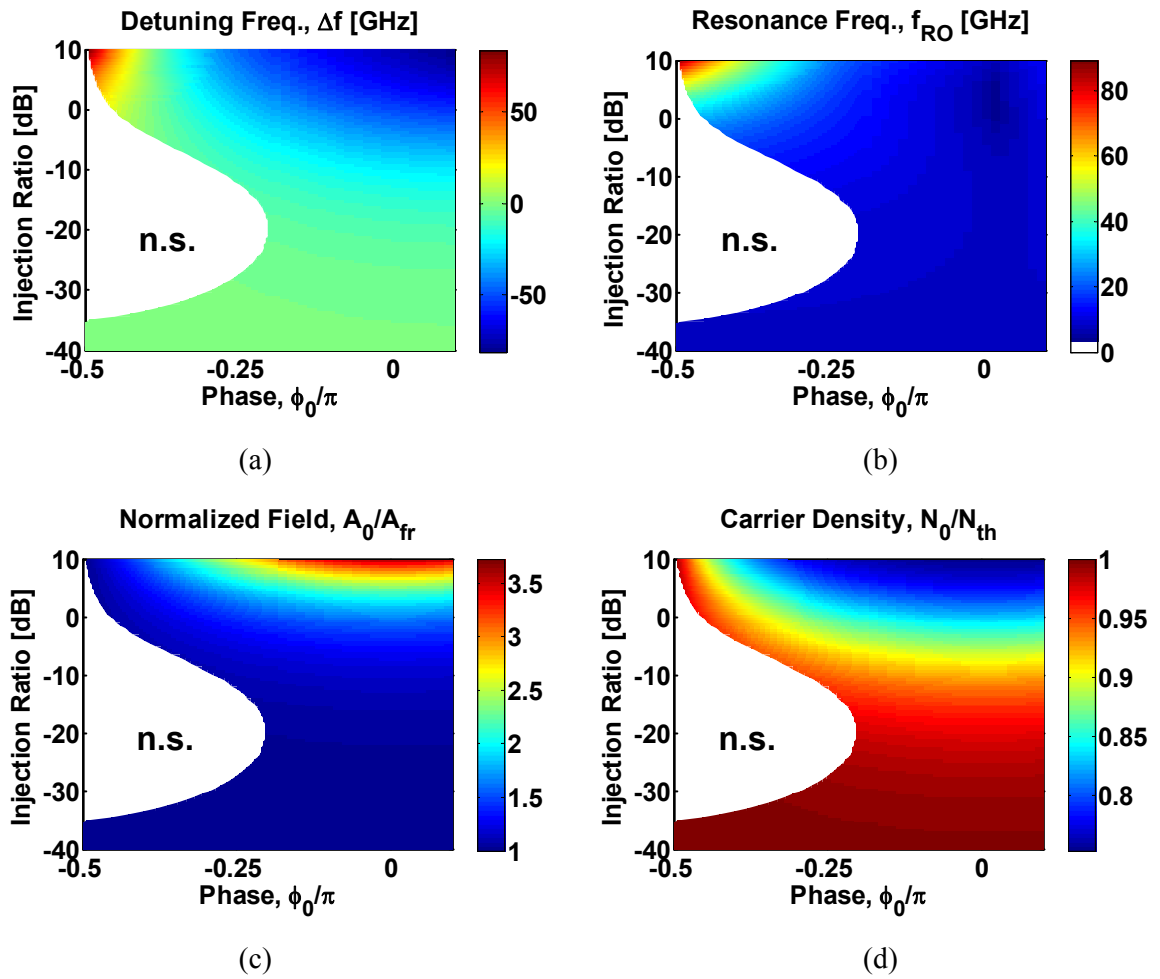


Figure 2.2 Phase and injection ratio versus: (a) detuning frequency, (b) resonance frequency, (c) normalized field, and (d) normalized carrier density. The range of phases correspond to $-\pi/2$ to $\cot^{-1}\alpha$.

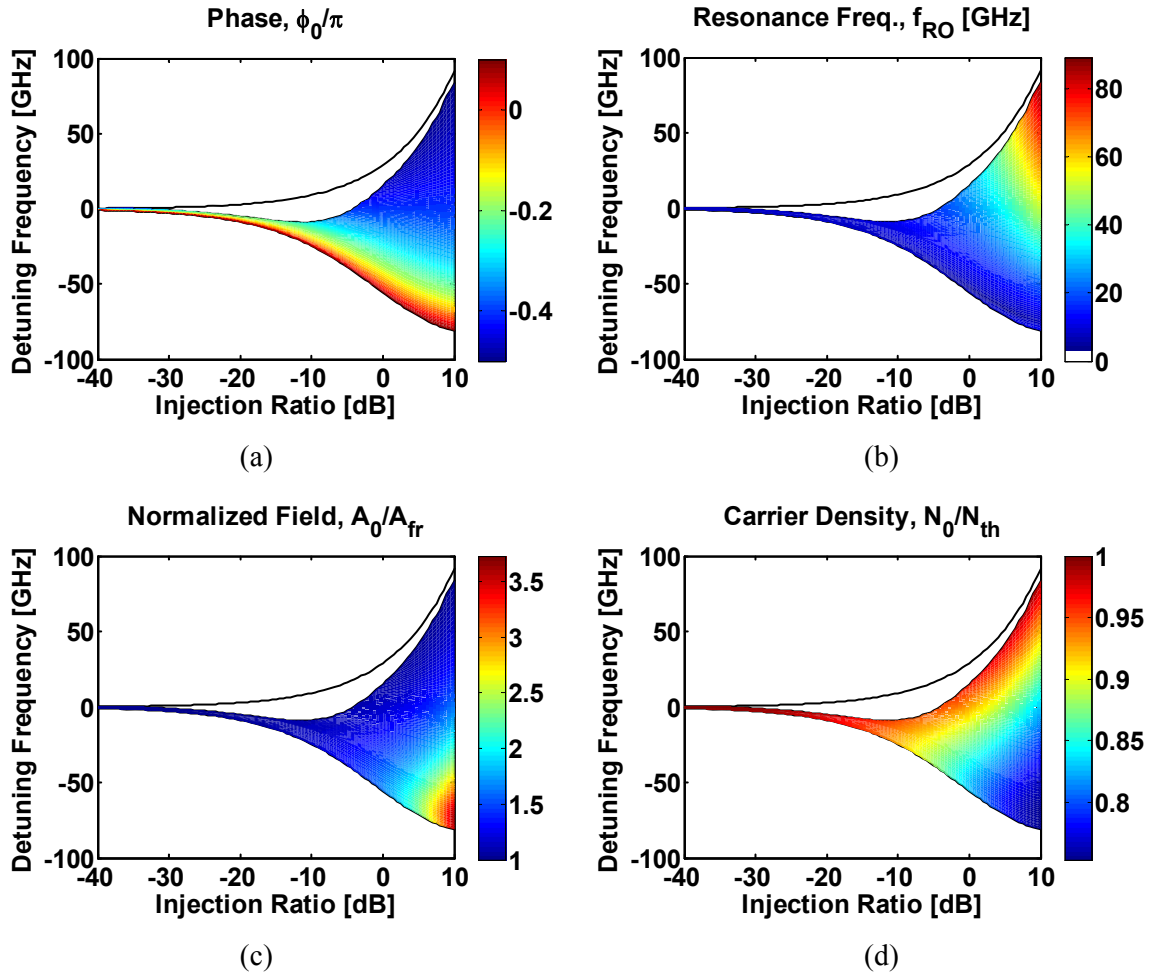


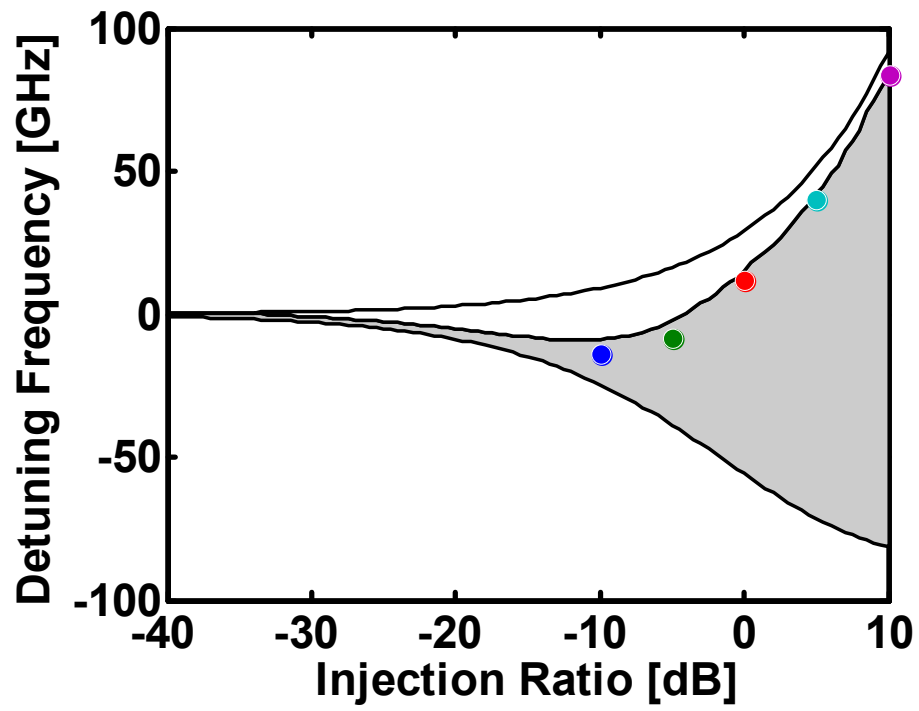
Figure 2.3 Locking map versus (a) phase (b) resonance frequency (c) normalized field, and (d) normalized carrier density.

2.5 Modulation Regimes

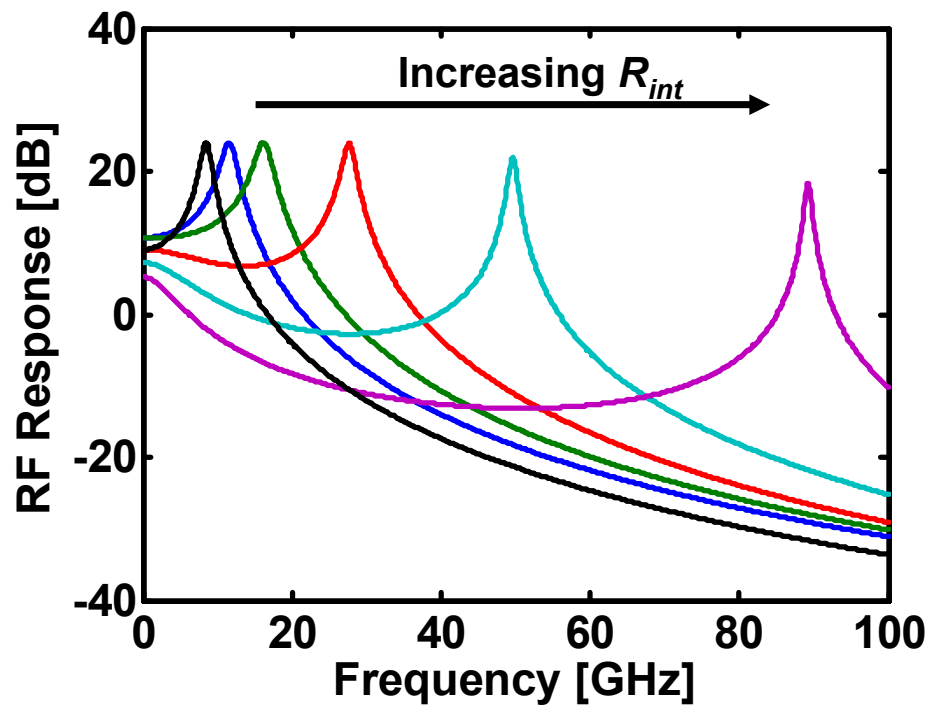
From Figure 2.3, we know that the resonance frequency increases with injection ratio and detuning frequency. However, the resonance frequency is not sufficient information to optimize an injection-locked laser's frequency response, as we saw in Figure 1.5. For example, the 3-dB bandwidth is not necessarily related to the resonance frequency.

2.5.1 Injection Ratio Effects on Frequency Response

We can use (2.15) to plot the frequency response for different values of injection ratio and/or detuning frequency. First, we increase the injection ratio, keeping the detuning close to the positive detuning edge. We do so because, by Figure 2.3(b), we see that the largest resonance frequency for a given injection ratio occurs on the positive edge. As we will see, the resonance peak can be arbitrarily close to the locking edge, and thus the damping can be made arbitrarily small. So, we choose detuning values such that the heights of the resonance peaks are roughly equal, and adjust the detuning accordingly to obtain this (Figure 2.4).



(a)



(b)

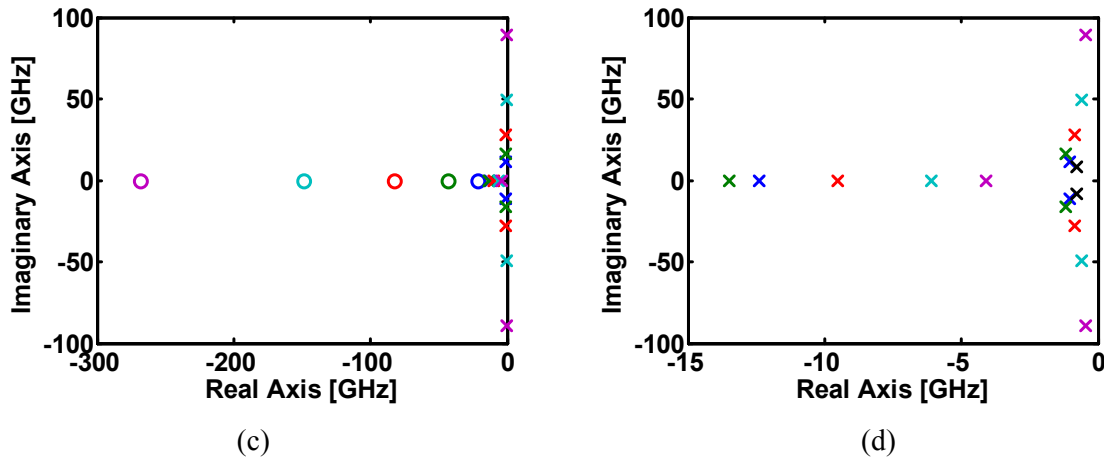


Figure 2.4 Effects of increasing injection ratio on the frequency response. (a) Locking map showing the bias points used in (b). (b) Frequency responses of the different injection ratio bias points, clearly showing that resonance frequency increases with increasing injection ratio. (c) Pole/zero diagram of the bias points. (d) Blow-up of the poles from (c).

Figure 2.4 shows the general trend that increasing the injection ratio increases the resonance frequency, but there are a few notes of interest. First, we must remember that the resonance frequency changes dramatically across the locking range, from the free-running value at the negative side, all the way to the maximum value on the positive side. Hence, the points chosen here are somewhat arbitrary, but they roughly approximate the maximum resonance frequency for a given injection ratio. Intuitively, it would be far more general to fix the injection ratio and sweep across the detuning range, which we will do in the next section. Secondly, it is evident that the 3-dB bandwidth is not proportional to the resonance frequency. As the maximum resonance frequency is increased, a dip occurs between DC and the resonance frequency. The dip falls below the 3-dB value before the resonance frequency is reached, thereby drastically reducing the usable broadband frequency range. This dip is not found in the two-pole system of a free-running laser. Figure 2.4(d) shows the cause of the dip. The dip is caused by the third

pole, located on the negative part of the real axis. It causes a 20 dB/decade roll-off for modulation frequencies larger than the pole's frequency. As the injection ratio is increased, the pole migrates toward the origin, pushing the start of the roll-off to lower frequencies. For low injection ratios, the third pole roll-off is roughly canceled by the zero, shown in Figure 2.4(c). For medium injection ratios, such as $R_{int} = 0$ dB (red curve), the zero has moved to much higher frequencies, exposing the third pole roll-off. However, the resonance frequency is low enough that, when the modulation frequency is increased, the resonance frequency is reached before the third pole roll-off has any significant effect in dipping the frequency response. Hence, it is important to note that the resonance frequency does not determine the 3-dB bandwidth. The idea of 3-dB bandwidth is explored in the next section as well as Section 2.6.

2.5.2 Detuning Frequency Effects on Frequency Response

It is more interesting to explore how the frequency response evolves by fixing the injection ratio and changing the detuning frequency. In Figure 2.5, we again show the classic locking range map. We choose a constant value of injection ratio, then vary the frequency detuning. Three representative plots and their corresponding pole/zero diagrams are shown in Figure 2.6(a), (b), and (c). The response is normalized to the DC response of the free-running laser. From these modulation response plots, we observe three regimes of modulation with distinctly different characteristics.

At negative detuning values (Figure 2.6(c)), the modulation response has a high gain, but relatively low bandwidth. We see no evidence of a resonance peak, since it is highly damped. Since non-linearities are generally proportional to high resonance peaks, this

regime should yield quite linear responses as well. This regime can be used for low bandwidth applications that need low link loss and/or high linearity.

At positive detuning values (Figure 2.6(a)), we see a sharp and high frequency resonance peak. As stated in the previous section, this regime suffers from a dip between DC and resonance. Therefore, the bandwidth is narrow and centered on the high-gain resonance peak. This regime can be used for narrow-band applications that need high gain at extremely high frequencies, or for ultra-high-frequency opto-electronic oscillators, as described in Chapter 7. Additionally, the high resonance is characterized by a near-single-sideband modulation signature, which will be explored in greater detail in Chapter 4. This can be useful for mitigating fiber chromatic dispersion effects [15].

The third regime lies in between these two (Figure 2.6(b)), characterized by a large broadband response. The detuning is well away from the positive frequency edge, so the resonance is well-damped. The response, therefore, has a large 3-dB ripple bandwidth as well, with good linearity. The applications for this regime are high bandwidth telecommunications, radar, or any application that requires large amounts of data transfer.

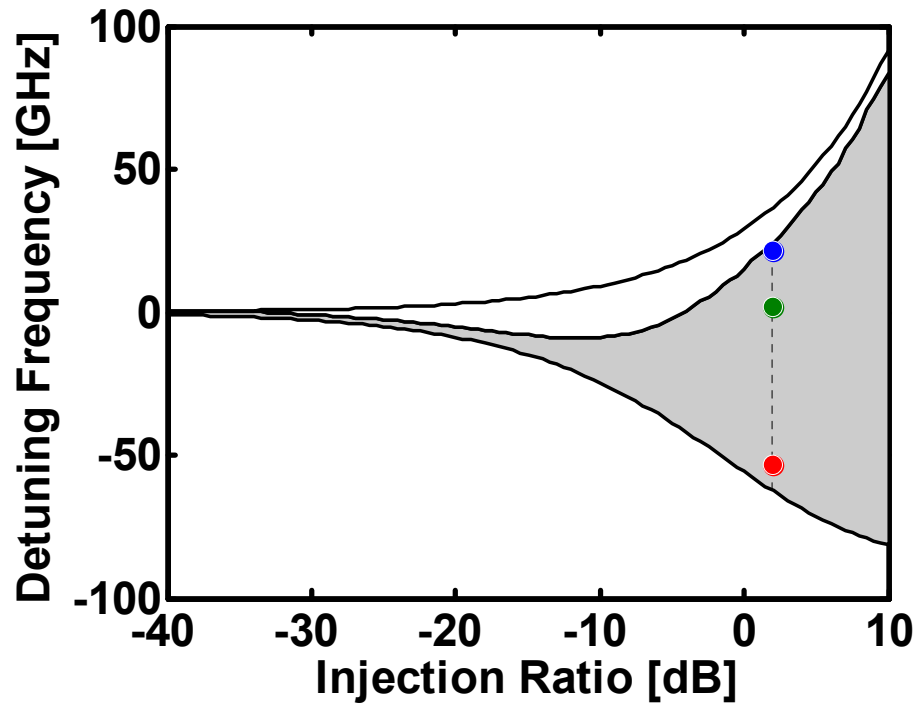


Figure 2.5 Locking map showing the bias points for the three regimes of modulation, for $R_{int} = 2$ dB, in Figure 2.6.

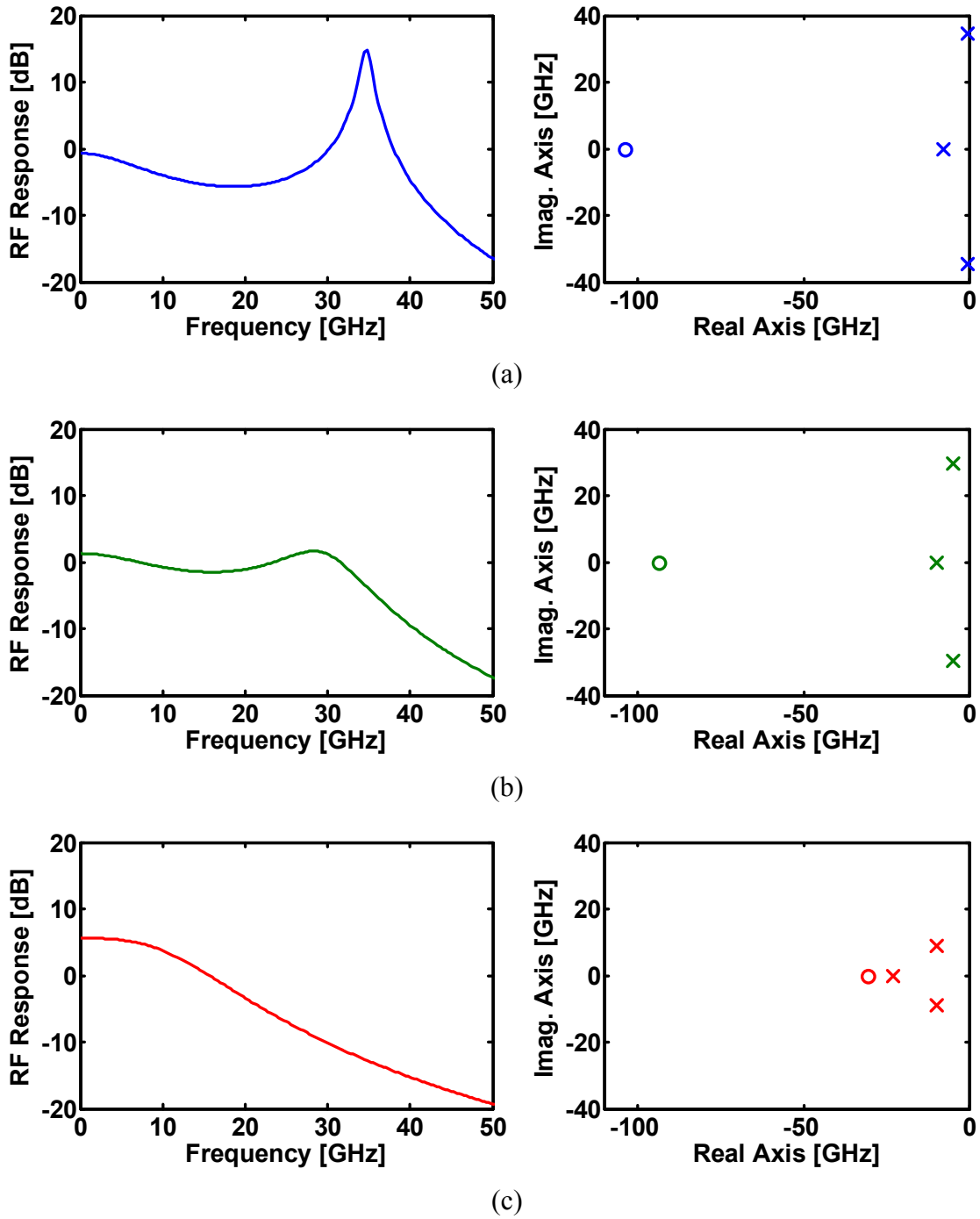
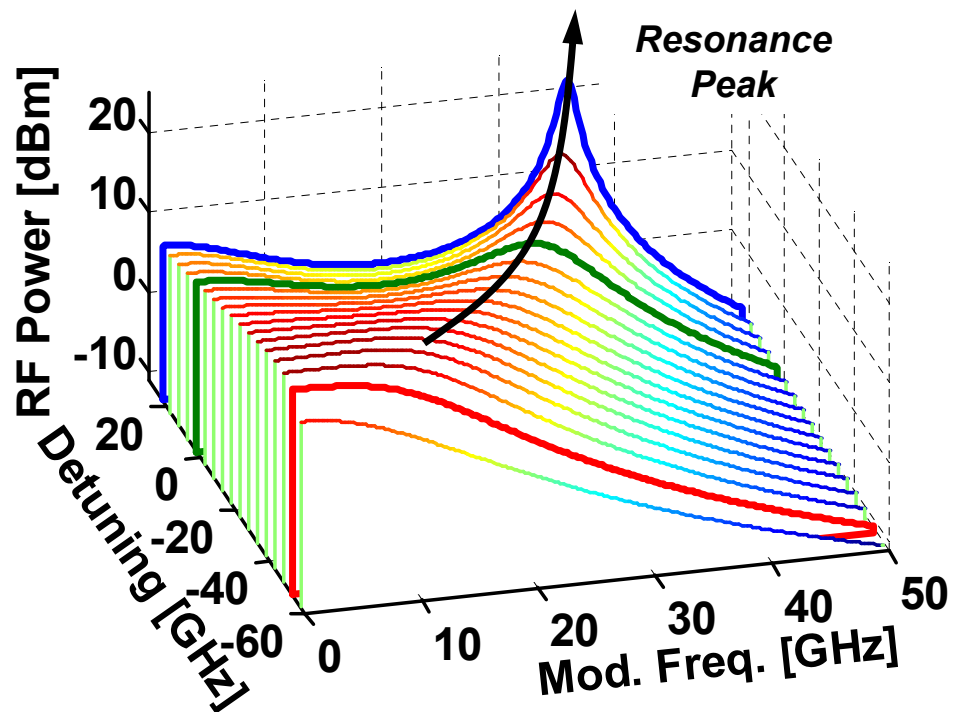


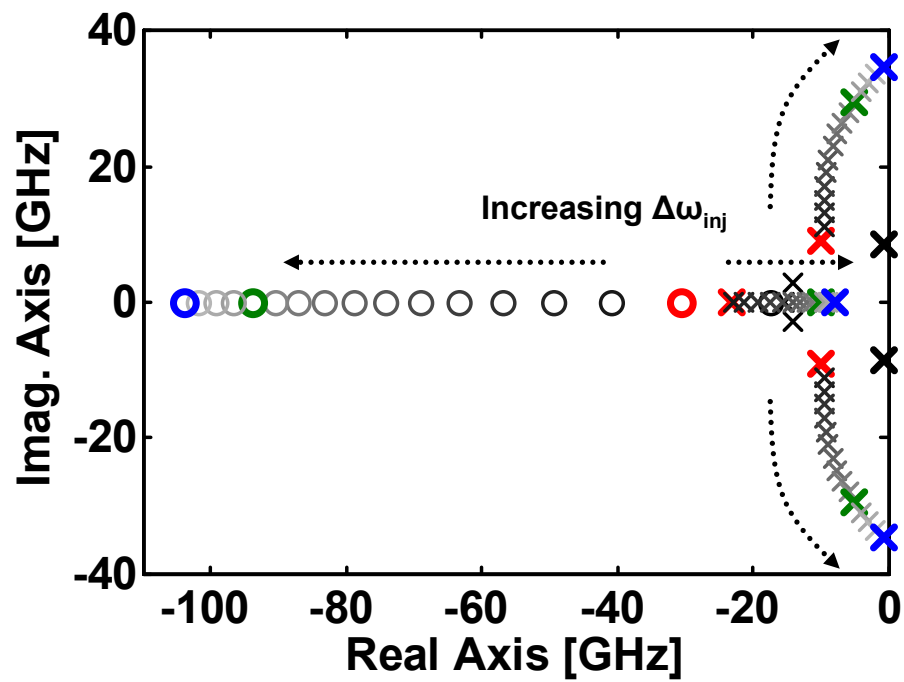
Figure 2.6 Frequency response and corresponding pole/zero diagrams for the three regimes of modulation: (a) high resonance frequency regime, (b) broadband regime, and (c) high gain regime.

It is obvious that the three regimes are not discrete; the three points in Figure 2.6 simply represent the optimized values for each regime. Rather, there is a continuum of frequency response curves across the detuning range. We show this in Figure 2.7. Again, we choose the same injection ratio as before, but instead we plot several frequency response curves along the entire range. The waterfall plot in Figure 2.7(a) shows the evolution of the frequency response. Each slice represents a frequency response curve for different detuning values. The three regimes we just introduced still appear, shown in the solid colored slices. For example, the red represents the high gain regime, the green represents the broadband regime, and the blue represents the high resonance regime. Additionally, the plot shows how the resonance frequency increases and damping decreases as we detune to higher frequencies. Again, the dip between DC and resonance occurs for higher detuning frequencies. From Figure 2.7(b), we see that the third pole also migrates to lower frequencies and the zero to higher frequencies as the detuning increases. Again, this exposes the third pole roll-off and moves it to lower frequencies.

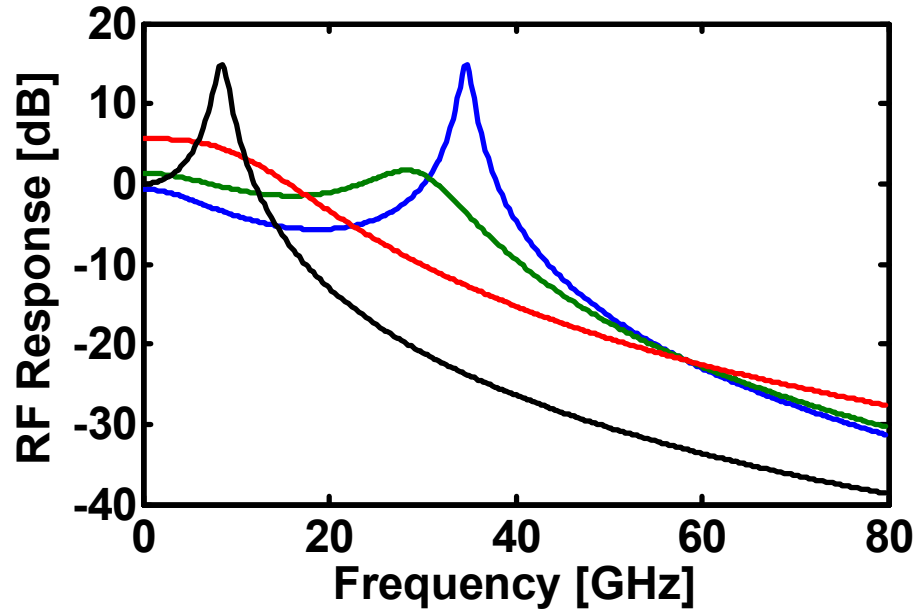
Finally, Figure 2.7(a) clearly shows the method for optimizing the 3-dB bandwidth. The resonance frequency must be increased until the point where the dip's nadir just touches the 3-dB mark. The resonance then brings the response up again, until it rolls off beyond the resonance frequency.



(a)



(b)



(c)

Figure 2.7 Theoretical waterfall plots showing frequency response versus detuning, for $R_{int} = 2$ dB. (a) Different frequency responses along the dotted line in Figure 2.5. The responses of the three bias points in Figure 2.5 are shown in their respective colors. (b) Pole/zero diagram corresponding to the same bias points. The bold, black points show the 2 poles of the free-running case. (c) Frequency responses of the three representative regimes, overlaid for comparison, plus the free-running response (black).

2.6 Analytic Approximations for Laser Figures-of-Merit

As we observed in Section 2.5, the three different modulation regimes have distinctly different characteristics. Depending on our application, we may prefer to bias the OIL system in one of the three regimes. This leads us to define different figure-of-merits for the different regimes. For example, in the high resonance frequency regime (blue curves in Figure 2.7), the obvious figure-of-merit is the resonance frequency. Additionally, we may wish to know the height of the peak, which is governed by the damping coefficient. In the broadband regime (green curves in Figure 2.7), the figure-of-merit is 3-dB frequency, or f_{3dB} , defined as the lowest frequency at which the modulation response

drops more than 3-dB below the DC response. Finally, in the high-gain regime (red curves in Figure 2.7), the figure-of-merit would be low-frequency (LF) gain, defined as the ratio of the DC responses of the injection-locked case versus the free-running case. For example, the LF gain for the red curve in Figure 2.7 would be approximately 5 dB above the free-running DC response. In this section, we attempt to quantify these figures-of-merit by deriving approximate analytical formulae.

2.6.1 Resonance Frequency

The concept of enhancement of resonance frequency by injection locking has been known for a decade [2, 4, 67]. In Section 2.5, we observed that the two major parameters that affect the resonance frequency are injection ratio and frequency detuning. The determinant of the frequency response can be used to determine the resonance frequency:

$$D(s) = s^3 + As^2 + Bs + C \quad (2.23)$$

The roots of this equation will be a pair of complex conjugate roots and a real, negative root. As with a free-running laser, the imaginary part of the complex conjugate pair should give us the resonance frequency. We can approximate this value.

For modulation frequencies in the GHz range and above, the last term, C , can be neglected:

$$C \ll s^3, As^2, Bs \quad (2.24)$$

Solving for a pure driving frequency:

$$D(j\omega) \approx j\omega(B - \omega^2 + j\omega A). \quad (2.25)$$

The determinant is proportional to that of a classic damped oscillator and takes the form:

$$D(j\omega) \approx j\omega(\omega_R^2 - \omega^2 + j\gamma\omega) = j\omega(j\omega + j\omega_R + \frac{1}{2}\gamma)(j\omega - j\omega_R + \frac{1}{2}\gamma) \quad (2.26)$$

where the resonance frequency, ω_R , is:

$$\omega_R^2 \approx B \quad (2.27)$$

and whose damping, γ , is

$$\gamma \approx A. \quad (2.28)$$

The first three terms of B , shown in (2.16), contain only diagonal terms in the matrix of (2.13). Physically, these terms correspond to the effect a state variable has upon itself, and are typically weak. Therefore, under typical conditions, we can consider the last two non-diagonal terms in B to dominate, yielding:

$$\omega_R^2 \approx -m_{AN}m_{NA} - m_{A\phi}m_{\phi A}. \quad (2.29)$$

The first term is the resonance attributed to the photons and carriers:

$$-m_{AN}m_{NA} = g\gamma_P A_0^2 \left(1 + \frac{g}{\gamma_P} \Delta N_0\right) = \omega_{R0}^2 \left(1 - \frac{\gamma_N}{\gamma_P} \frac{\Delta N_0}{A_{fr}^2}\right). \quad (2.30)$$

where $\omega_{R0} = (g\gamma_P A_{fr}^2)^{1/2}$ is the relaxation oscillation of the free-running laser, using the equality in (2.7). The last term in (2.30) is much smaller than unity and therefore $-m_{AN}m_{NA} \approx \omega_{R0}^2$. Using (2.14) and (2.30) to expand (2.29), we get:

$$\omega_R^2 \approx \omega_{R0}^2 + \Delta\omega_R^2 \quad (2.31)$$

where we have defined the resonance frequency enhancement term as the second term in (2.29):

$$\Delta\omega_R = \left| \kappa_{inj} \frac{A_{inj}}{A_0} \sin \phi_0 \right|. \quad (2.32)$$

which describes the resonance attributed to the photon field and its phase. The steady-state condition of (2.4) is:

$$-\frac{\alpha}{2} g(N_0 - N_{th}) + \Delta\omega_{inj} + \kappa \frac{A_{inj}}{A_0} \sin \phi_0 = 0 \quad (2.33)$$

Using (2.32) and (2.33), we obtain a more physical formula:

$$\Delta\omega_R = \left| -\frac{\alpha}{2} g(N_0 - N_{th}) + \Delta\omega_{inj} \right|. \quad (2.34)$$

As described by Murakami [3], the resonance frequency enhancement is equal to the difference between the master laser frequency and that of the slave laser's natural cavity mode frequency. This cavity mode is shifted by α via the first term in (2.34). This will be described further in Section 2.7. Equation (2.31) is similar to Henry's formulation [2], although the derivation is different, and improves upon Murakami's approximate formula, which does not include the absolute value sign, and does not approximate well for negative detuning frequencies where the resonance frequency is small.

2.6.2 Damping

Here, we describe an approximate term for the damping coefficient. This is useful for describing the height of the resonance peak. We can expand the damping term, using (2.14), (2.16), and (2.28):

$$\gamma \approx \gamma_N + gA_0^2 + 2z \cos \phi_0 \quad (2.35)$$

Using the steady-state solution for (2.3), we can replace the 2^{nd} term on the right-hand side (r.h.s.) to a more physical term:

$$\gamma \approx \gamma_0 - g(N_0 - N_{th}) \quad (2.36)$$

where $\gamma_0 = \gamma_N + gA_0^2$ is the free-running damping term. Therefore, the injection-locked laser's damping is the free-running damping, enhanced by the reduction of gain below threshold. A basic physical explanation is that the damping is enhanced by a reduction in gain. The injection-locked laser resonance is primarily due to energy oscillating between the slave field and the slave phase interfering with the injected master light. The reduced gain allows a portion of this oscillating energy to be lost to the carriers. We can make an analogy to a RLC circuit oscillator, where the field, phase, and carriers are the energy in the capacitor, inductor, and heat. The capacitor and inductor energies oscillate between each other, while increasing the resistance causes more energy to be leaked into heat, thus damping the oscillations.

Equation (2.36) is accurate if C is negligible. However, when modulated with frequencies near the resonance, the approximate determinant in (2.26) becomes small and C becomes important:

$$D(s) = s(s + j\omega_R + \frac{1}{2}\gamma)(s - j\omega_R + \frac{1}{2}\gamma) + C \quad (2.37)$$

In this case, near resonance, we can assume that the damping at resonance is:

$$\begin{aligned} D(j\omega_R) &= j\omega_R(j\omega_R + j\omega_R + \frac{1}{2}\gamma)(j\omega_R - j\omega_R + \frac{1}{2}\gamma) + C \\ &\approx j\omega_R(2j\omega_R)(\frac{1}{2}\gamma) + C \\ &= -\gamma\omega_R^2 + C \end{aligned} \quad (2.38)$$

This can be viewed as a modified damping term, where

$$\begin{aligned} -\gamma_M\omega_R^2 &= -\gamma\omega_R^2 + C \\ \gamma_M &= \gamma - \frac{C}{\omega_R^2} \end{aligned} \quad (2.39)$$

When the laser is near the positive detuning frequency edge ($\phi = -\pi/2$), the frequency response exhibits a pronounced resonance. Solving for C at this edge, we obtain:

$$C(\phi = -\pi/2) = z\alpha g\gamma_P A_0^2 + z^2(\gamma_N + gA_0^2) \quad (2.40)$$

From (2.32) and the definition of z , we can approximate $z \approx \Delta\omega_R$, so that

$$\gamma_M(\phi = -\pi/2) \approx -\frac{\alpha g\gamma_P A_0^2}{\Delta\omega_R} - g(N_0 - N_{th}). \quad (2.41)$$

The carrier number must be sufficiently below threshold for the damping term to be positive and the solution to remain in the R.O.C. Another interesting note is that the damping can shift arbitrarily close to zero (as also seen in the pole/zero diagram trend for increasing detuning frequency, Figure 2.7(b)). This would predict that we can make the resonance peak arbitrarily high. However, this is not found in experiments; the lasers become unlocked before the modulation power becomes larger than the free-running slave laser line. This is possibly due to spontaneous emission from the slave, which begins to dominate the dynamics when the master detuning approaches the edge of stable locking. Further analysis of where the theory breaks down is needed, possibly by including a spontaneous emission term.

2.6.3 Low-Frequency Gain

The low-frequency modulation response can oftentimes be higher than the free-running response. As shown in Figure 2.7, this typically occurs near the negative detuning frequency edge of the locking range, where the resonance frequency is very low. Intuitively, when the laser is near the negative detuning edge, the extremely-low

resonance frequency contributes to increasing the DC gain. We can derive an analytical formula for this.

At zero frequency, (2.15) reduces to:

$$H(j\omega = 0) = \frac{-m_{AN}m_{\phi\phi} + m_{A\phi}m_{\phi N}}{C}. \quad (2.42)$$

Expanding this into laser parameters yields:

$$H(0) = \frac{\frac{1}{2}gzA_0(\cos\phi_0 - \alpha\sin\phi_0)}{z^2(\gamma_N + gA_0^2) + gzA_0^2(\gamma_P - 2z\cos\phi_0)(\cos\phi_0 - \alpha\sin\phi_0)}. \quad (2.43)$$

We know to look for the peak DC response near the negative detuning frequency edge. However, when the system is locked exactly at the negative detuning frequency edge, $\phi_0 = \cot^{-1}\alpha$, which would make the numerator term, $\cos\phi_0 - \alpha\sin\phi_0 = 0$, leading to poor DC response. From this, we deduce that the peak is near, but not at, the negative detuning edge.

When we deal with RF response, we must multiply the response, $H(0)$, with the fundamental, A_0 , at that particular bias point. This favors the negative detuning side since the field increases above free-running as the system approaches this edge (Figure 2.3(c)). Additionally, we can claim that

$$\gamma_N \ll gA_0^2 \quad (2.44)$$

since the carrier recombination rate is much slower than the stimulated emission rate in a lasing laser. This inequality is further amplified near the negative detuning edge, since the field is again higher than free-running at this edge. This reduces the response to:

$$A_0H(0) = \frac{\frac{1}{2}(\cos\phi_0 - \alpha\sin\phi_0)}{z + (\gamma_P - 2z\cos\phi_0)(\cos\phi_0 - \alpha\sin\phi_0)}. \quad (2.45)$$

One can solve this function by noting that z depends on R_{int} and A_0 , the latter which depends on ϕ_0 . This function is complicated to maximize, however some general trends can be noted. In general, this function is maximized when R_{int} is larger, since the response is proportional to A_0 (which is large for negative detuning and larger injection ratios). The function also grows with increasing α and decreasing γ_p .

2.6.4 Frequency Response: The Real Pole

The value of the third, real pole factors greatly in the size of the dip between DC and resonance. The smaller the pole, the earlier the dip appears in the frequency response, leading to poor 3-dB bandwidth. Here, we attempt to extract some trends for mitigating this effect. In other words, we wish for the largest frequency for the third pole.

The full determinant, when expanded, takes on a value of:

$$\begin{aligned} D(s) &= (s - P)(s + j\omega_R + \frac{1}{2}\gamma)(s - j\omega_R + \frac{1}{2}\gamma) \\ &= s^3 + (\gamma - P)s^2 + (\omega_R^2 - \gamma P)s - \left(\omega_R^2 + \frac{\gamma^2}{4}\right)P \end{aligned} \quad (2.46)$$

where P is defined as the value of the third, real pole. Comparing it to the determinant equation in (2.23), we see that the final term in both equations can be equated, giving us:

$$P = C \left(\omega_R^2 + \frac{\gamma^2}{4} \right)^{-1}. \quad (2.47)$$

It is clear that the higher the resonance frequency, the smaller the pole (and therefore, larger dip), which corresponds to the trend seen in the pole/zero diagram shown in Figure 2.7(b) and Figure 2.4(d). Thus, we wish to maximize the value of C , shown here:

$$C \approx g_z A_0^2 [z + (\gamma_p - 2z \cos \phi_0)(\cos \phi_0 - \alpha \sin \phi_0)] \quad (2.48)$$

where we have made the same approximation as in (2.44). Hence, we see that increasing the injection ratio (through z) and increasing the slave field, A_0 , will maximize the value of C . The latter amounts to either detuning the laser to the negative frequency side or increasing the bias current to obtain a higher free-running slave power. Increasing the photon decay rate also serves to increase C . This can be accomplished by engineering a lower mirror reflectivity.

2.6.5 Frequency Response: The Zero

The zero of the frequency response solution in (2.15) is:

$$Z = (m_{AN} m_{\phi\phi} - m_{A\phi} m_{\phi N}) / m_{AN}. \quad (2.49)$$

After expanding this with (2.14) and reducing, the zero's value is simply:

$$Z = z(\alpha \sin \phi_0 - \cos \phi_0) \quad (2.50)$$

Hence, across the detuning range, from negative to positive edges, the zero takes on a value of $Z = 0$ to $Z = -z\alpha$. In terms of optimizing the bandwidth of the frequency response, the zero should be minimized, so that once the modulation frequency exceeds the zero's value, the numerator will scale roughly with the modulation frequency. This corresponds to bias points close to the negative detuning edge. Unfortunately, the zero scales with injection ratio, which is necessary for increasing bandwidth. Fortunately, a large zero frequency doesn't hurt the modulation bandwidth, since the numerator looks like a constant for modulation frequencies much smaller than the zero frequency. A small zero value would only serve to mitigate the effects of the dip caused by the third (real) pole. The approximate optimal point would be when the zero value equals the third pole value, thereby canceling the effect of both. This would leave an approximately two-pole

system, which we know from classic laser physics does not dip before hitting the resonance frequency. However, this point would correspond to a very low resonance frequency, and would gain scant benefits from the enhanced resonance. Otherwise, reducing the α parameter may serve to reduce the zero. Still, the effect of lowering the 3rd pole is more dominant than reducing the value of the zero.

2.6.6 Optimizing Bandwidth

The broadband regime is a delicate balance between the DC to resonance dip, the damping factor, and the resonance frequency. In general, these values are complex analytical functions. Although it is difficult to derive an intuitive analytical formula to assist in optimization of the injection-locked system for maximum broadband performance, we can make some general observations and trends. As stated in Section 2.6.4, the bias current, injection ratio, and photon decay rate should be increased.

We can estimate the maximum bandwidth point (across the detuning range) by following a few approximations. The dip, caused by the 3rd pole, should not go 3 dB below DC before the modulation frequency reaches the full-width half-maximum (FWHM) of the resonance frequency. The intersection of these two points, shown as circled in Figure 2.8, represents this condition. The resonance frequency is then the approximate maximum bandwidth point.

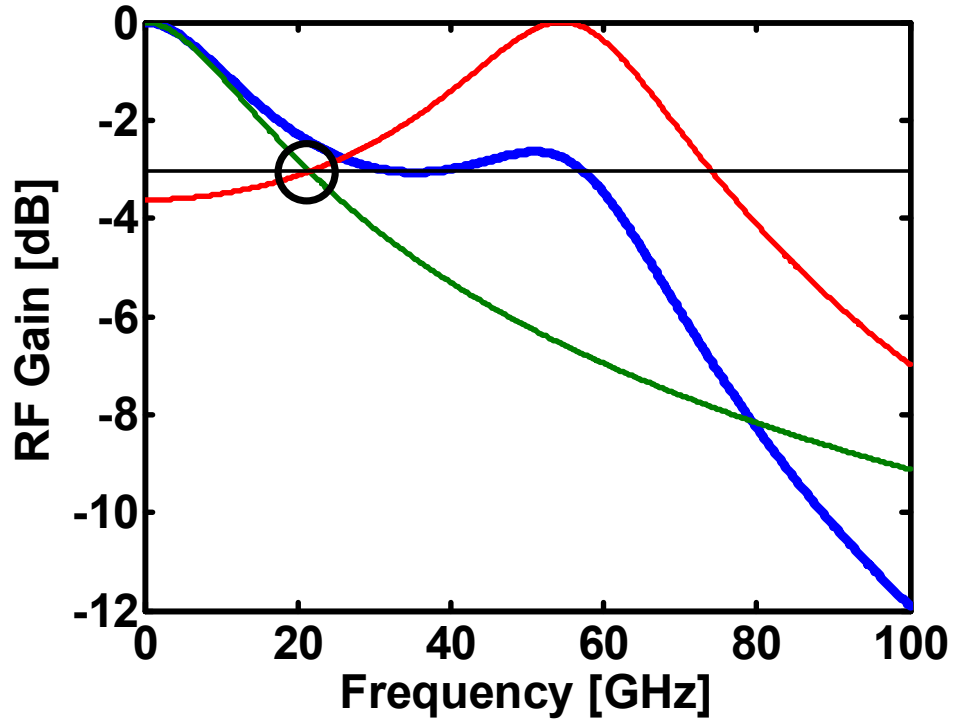


Figure 2.8 Graphic of method for maximizing bandwidth. The green line corresponds to the response of the 3rd pole. The red line corresponds to the response of the resonance frequency. The 3-dB point of both lines must meet to maximize the total bandwidth, shown in blue.

Taking into consideration the zero and the 3rd pole, we attempt to find its 3-dB point:

$$\left| \frac{j\omega_{3dB} - Z}{j\omega_{3dB} - P} \right|^2 = \frac{Z^2}{2P^2} \quad (2.51)$$

which yields:

$$\omega_{3dB} = \frac{PZ}{\sqrt{Z^2 - 2P^2}} \quad (2.52)$$

The FWHM of the resonance peak is simply $\omega_R - \frac{\gamma}{2}$. Setting these two points equal

yields:

$$\omega_R - \frac{\gamma}{2} = \frac{PZ}{\sqrt{Z^2 - 2P^2}}. \quad (2.53)$$

One can numerically solve for the ϕ_0 that will satisfy this equation. This yields the approximate bandwidth as simply ω_R .

2.7 Cavity Mode

The physical origin for the resonance enhancement has been a subject of much debate. We attempt to explain the origin here. In Figure 2.9(a), we see an illustration of the optical spectrum of a single-mode free-running slave laser, lasing at ω_{fr} . When we add injection from the master laser at a positive detuning value, the effects are shown in Figure 2.9(b). The majority of the slave's optical power is pulled to the locked mode, ω_{inj} . However, the slave's cavity mode, defined by the laser length and cavity roundtrip time (a function of laser length and effective index), does not vanish. In fact, the cavity mode continues to exist, but is red-shifted via the α parameter [65]. The carrier density, as shown in Section 2.4, can deviate from threshold (free-running value). Hence, the index changes via the linewidth enhancement parameter and therefore, the cavity resonance frequency changes. The value of the shift, $\Delta\omega_{shift}$, is equal to the first term in (2.34):

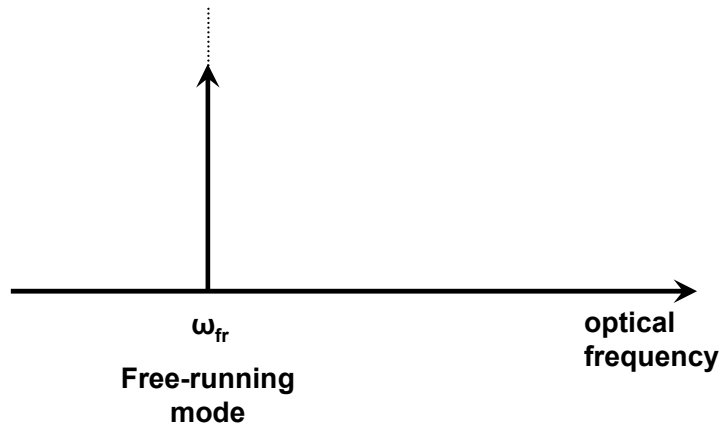
$$\Delta\omega_{shift} = \frac{\alpha}{2} g(N_0 - N_{th}) \quad (2.54)$$

and is always negative, since the carrier number must always be below threshold. Finally, the total difference between the cavity mode (ω_{cav}) and the locked mode (ω_{inj}) frequencies is called the resonance enhancement frequency, $\Delta\omega_R$:

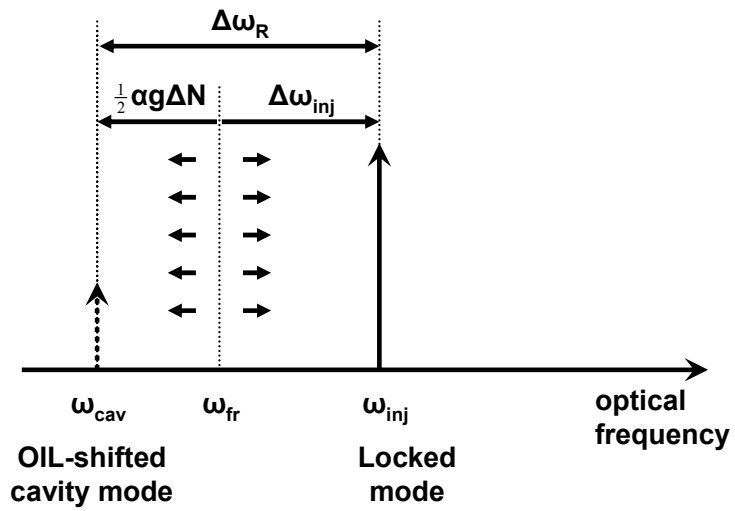
$$|\omega_{inj} - \omega_{cav}| = \Delta\omega_R = |\Delta\omega_{inj} - \Delta\omega_{shift}| \quad (2.55)$$

and is equivalent to (2.32) and (2.34).

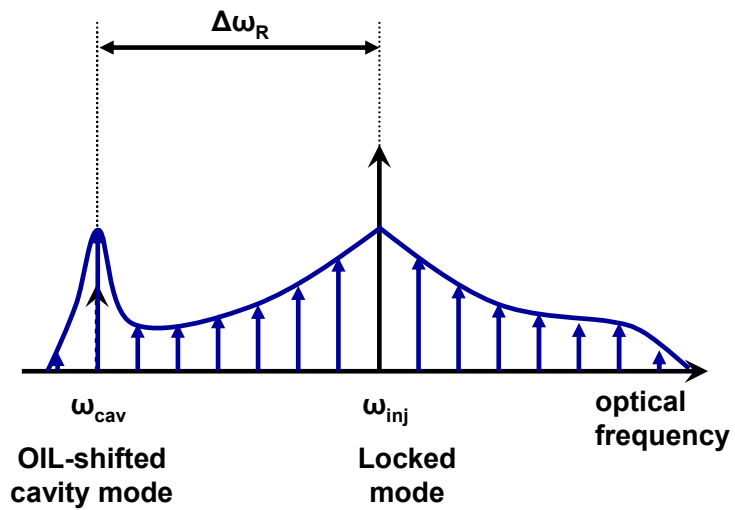
This cavity mode will resonantly amplify any modulation sideband at or near its frequency. When we modulate the locked mode near the value of $\Delta\omega_R$, an optical modulation sideband appears near the cavity mode. This sideband will be resonantly amplified, shown in the dark blue curves in Figure 2.9(c).



(a)



(b)



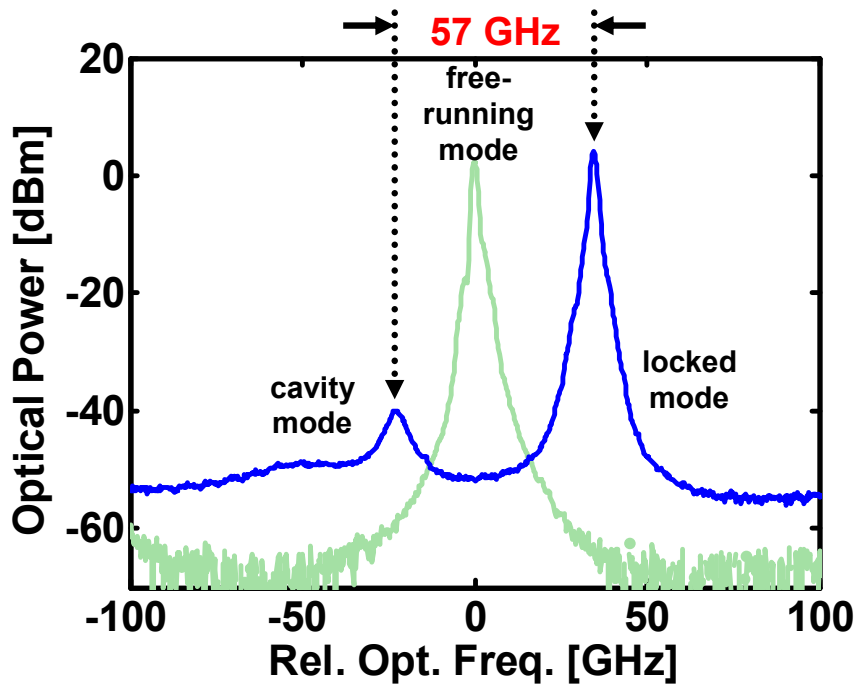
(c)

Figure 2.9 Cavity mode model of injection locking. (a) shows the laser line of the free-running slave laser. (b) When the slave is injection-locked by a positive detuning frequency, the cavity mode shifts to the red side while the locked optical mode shifts to the blue side. The difference between the locked and cavity modes is the resonance frequency enhancement factor, $\Delta\omega_R$. (c) When modulation is swept from DC to high frequencies the cavity mode will resonantly enhance any modulation sideband (dark blue) that appears near it.

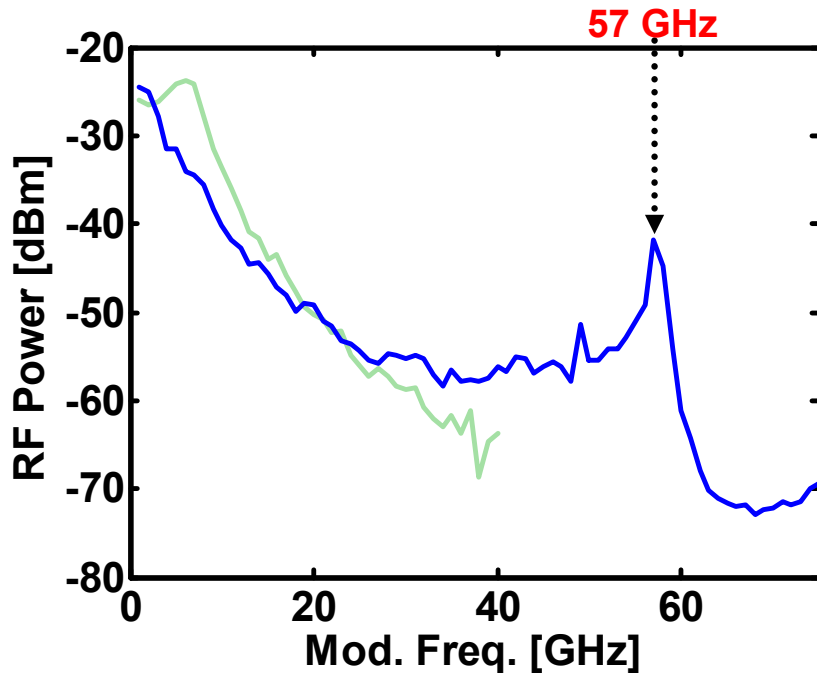
We show experimental evidence of this theory in Figure 2.10(a). The light green curve is the optical spectrum of a free-running single-mode distributed feedback (DFB) laser. In Figure 2.10(b), we show its corresponding frequency response also in light green. The spectrum is single-mode and the resonance frequency is about 6 GHz. The blue curves represent a locked case, where the master is positively detuned to +34 GHz and the system is in the strong optical injection case. When locked to the master laser, the majority of the slave's power is locked to the master laser line, as seen by the "locked mode" in Figure 2.10(a). However, the slave's natural cavity resonance still persists, as revealed by the small amplified spontaneous emission peak at the frequency 23 GHz lower than the free-running value. In Figure 2.10(a), we see that the locked and cavity modes are 57 GHz apart. When the locked slave laser mode is modulated at or around 57 GHz, this will create a resonantly-enhanced sideband. In Figure 2.10(b), this causes the frequency response (also in blue) to show a 57 GHz resonance peak.

Note that despite the high resonance frequency, the DC to resonance response has a large dip, as predicted by theory. Thus, the 3-dB bandwidth is not proportional to the resonance frequency. To date, there has been no coherent study linking OIL 3-dB bandwidth to resonance frequency. One of the goals of this dissertation is to establish this link in order to optimize both bandwidth and resonance frequency. The optimized data

will be presented in Chapter 5. Additionally, the modulation response above 50 GHz was obtained using the optical heterodyne detection system described in Chapter 4.

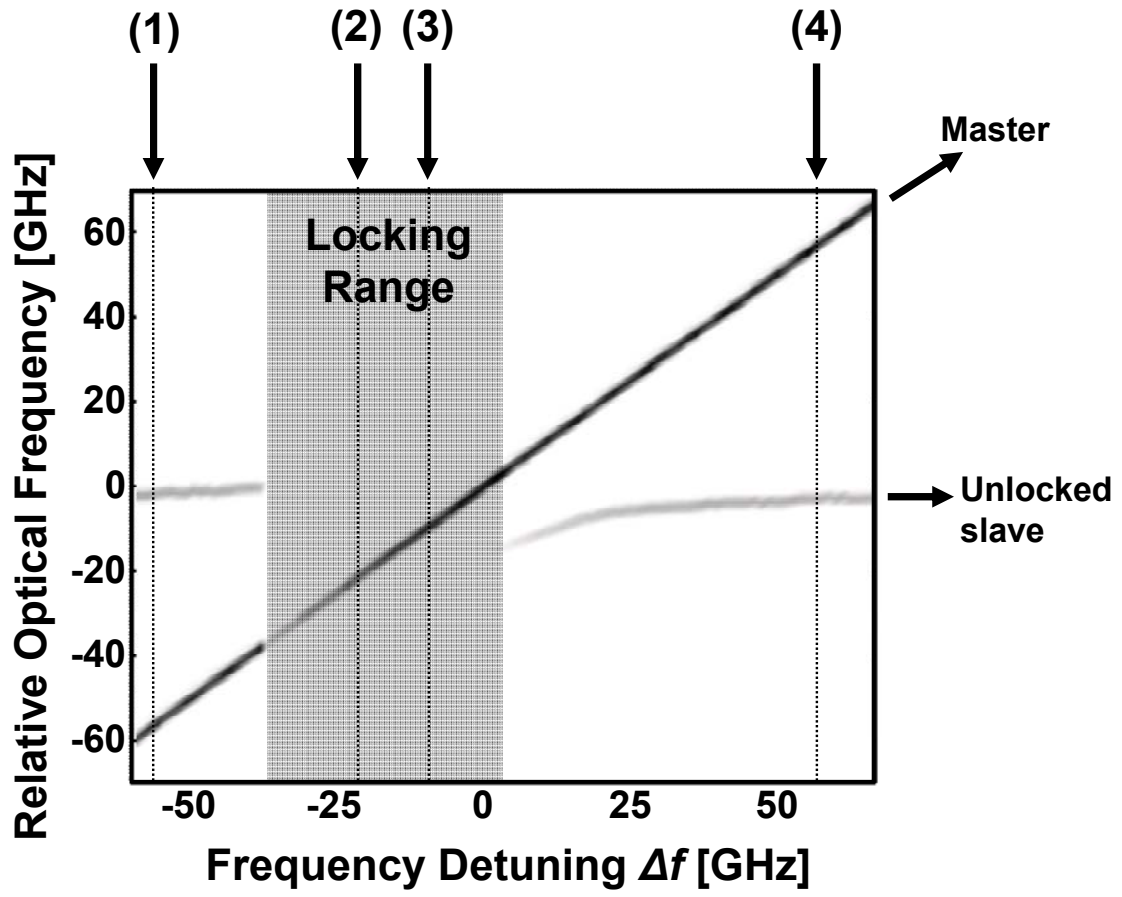


(a)



(b)

Figure 2.10 Experimental representation of origin of resonance frequency enhancement. (a) Optical spectrum showing shifting of cavity mode ($f_{cav} - f_{fr} = -23$ GHz) and positively-detuned locked mode ($\Delta f_{inj} = +34$ GHz). Injection-locked case is in blue, free-running in light green. (b) Modulation frequency response showing resonance peak enhanced to 57 GHz.



(a)

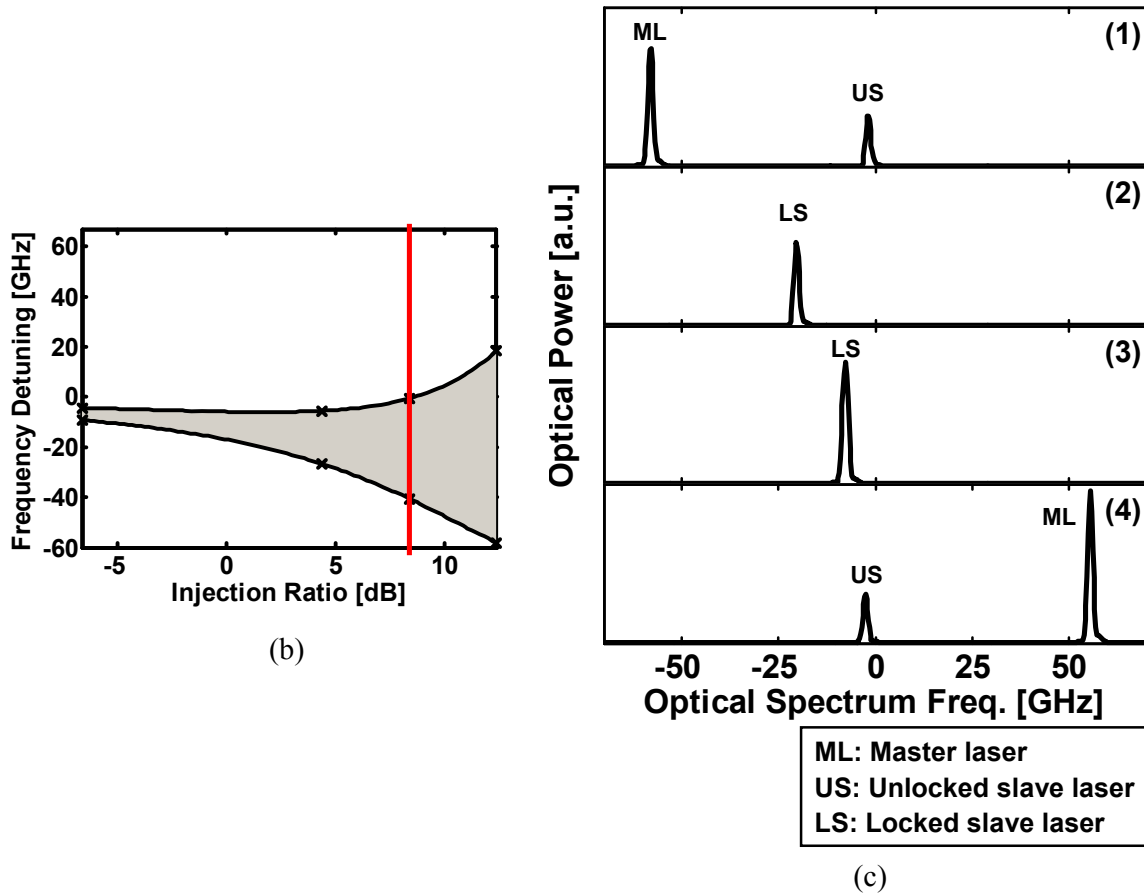


Figure 2.11 Optical spectra evolution across the locking range, with fixed injection ratio. (a) shows a surface plot of the optical spectrum of master and slave over a continuous range of detuning frequencies. Darker signifies higher power. (b) the experimental locking map, where the red vertical line signifies the range of bias points that correspond to the spectra in (a). (c) sample optical spectra at the four labeled points in (a). (1) shows the master on the red side of the unlocked slave. (2) and (3) show the slave locked to the master, since the master is within the locking range. (4) shows the master on the blue side of the unlocked slave.

Figure 2.11 shows mode evolution across the locking range of an injection-locked DFB laser, and further evidence of the cavity mode dynamics. Figure 2.11(a) shows the experimentally-measured optical spectrum over the full locking range. The diagonal line marks the frequency position of the master as it is scanned through the detuning frequencies. The broken horizontal line shows the frequency of the slave. The gray region

signifies the locking range: -37 GHz to +2 GHz. Within the locking range, the slave becomes the same frequency as the master. Note that at the negative frequency edge of the locking range, the laser becomes unlocked discretely, as evidenced by the separate master and slave modes to the red side and a single locked mode on the blue side. On the positive frequency edge, however, the laser becomes unlocked in a gradual manner, where the slave mode gradually builds up from noise (around +2 GHz) to a point where it has recovered all of its free-running power (around +30 GHz). Experimentally, we can arbitrarily consider the positive edge of the locking range the point at which the cavity mode has 30 dBc of side-mode suppression ratio (SMSR) from the locked mode. Figure 2.11(b) shows the experimental locking map, where the vertical red line marks the range of detuning frequencies that were used in Figure 2.11(a). Figure 2.11(c) shows sample spectra at different points inside (2&3) and outside (1&4) the locking range.

2.8 Phasor Model

The model presented in Figure 1.3 argues that the injected light dominates over the slave spontaneous emission generation, thus winning the competition of gain and determining the slave's lasing wavelength. This model breaks down when we consider detuning the master laser away from the slave's natural cavity resonance, as described in the previous section. For instance, we would expect frequency-filtering effects due to the cavity of a DFB laser to reduce the lasing magnitude when we detune away from the free-running frequency. However, this is not the case. We can gain better insight to injection locking physics by using a phasor model, expanded upon the one developed by Henry [2].

We define the difference between injected and cavity mode frequencies as $\Delta\omega$:

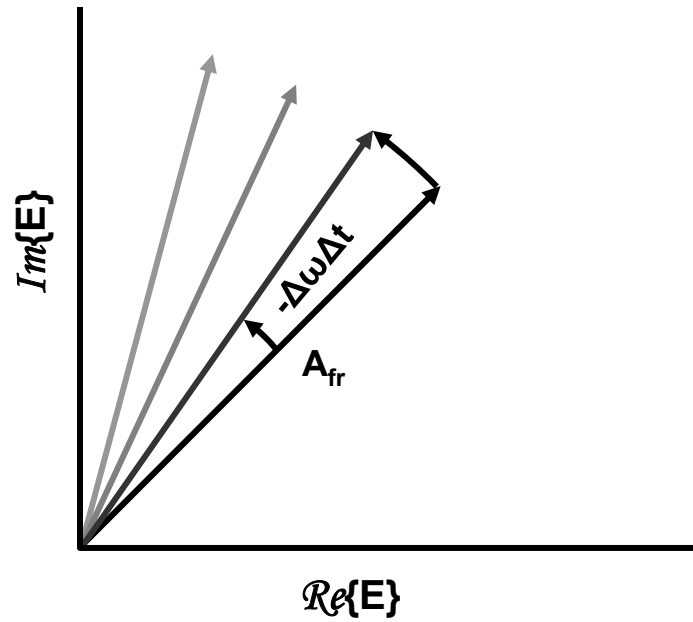
$$\Delta\omega \equiv \omega_{inj} - \omega_{cav} = -\frac{\alpha}{2}g(N_0 - N_{th}) + \Delta\omega_{inj} \quad (2.56)$$

and is simply a signed version of $\Delta\omega_R$. Substituting (2.56) into the complex field rate equation, (2.2), yields:

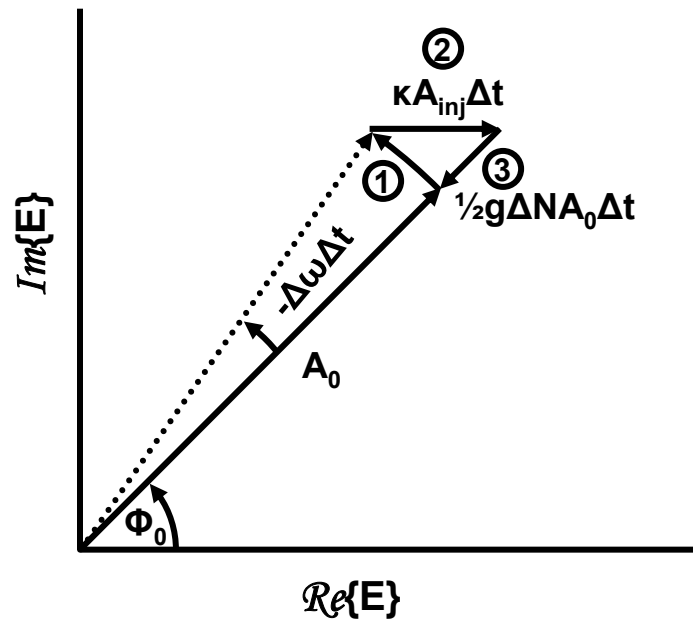
$$\frac{dE(t)}{dt} = \frac{1}{2}g\Delta NE(t) + \kappa A_{inj} - j\Delta\omega E(t). \quad (2.57)$$

This equation can be illustrated graphically in Figure 2.12. Figure 2.12 shows the phasor of the slave laser field, in the frequency frame-of-reference of the master laser. In other words, if the slave was locked to the master, they would share the same frequency and the phasor in Figure 2.12 would not rotate over time. Figure 2.12(a) shows the slave when lasing at its natural cavity mode frequency. Since its frequency differs from the master's by $\Delta\omega$, the phasor rotates by $\Delta\omega\Delta t$ during each time interval, Δt . Figure 2.12(b) shows the slave when locked. In a time interval, Δt , the sum of three vectors balance to return the phasor to its original position, thus preserving the steady-state requirement. In (2.57), this would be equivalent to setting the derivative to zero. Vector 1, which is equivalent to the $-j\Delta\omega E(t)$ term of (2.57), rotates the phasor by the frequency difference of master (locked) and slave cavity mode, $\Delta\omega$. Vector 2, equivalent to the $+\kappa A_{inj}$ term of (2.57), adds the contribution of the injected light. This differs in phase to the slave phasor by ϕ_0 . Since the injected light increases the slave field, the slave's gain must reduce in order to maintain a steady-state amplitude. This gain reduction is achieved by reducing the carrier number to below threshold. Its effects are shown by vector 3 (the $\frac{1}{2}g\Delta NE(t)$ term of (2.57)), where the slave's amplitude is reduced by the negative overall gain. Here, ΔN is

the carrier number difference from threshold ($\Delta N \equiv N_0 - N_{th}$). The three vectors sum to keep the phasor in steady-state. Vector 1 iterates the fact that *even during stable locking conditions, the slave still lases at its natural cavity mode*. To wit, it is almost the same vector as the free-running case in Figure 2.12(a), with the additional frequency shift due to the carrier change (Equation (2.34)). However, in the locked case, the constant addition of injected light “kicks” the slave phase to match that of the master, thus locking its wavelength. This kicking effect by the injected light is similar to the Doppler effect for sound waves. A relative velocity change between sound wave and observer causes a frequency shift in the perceived sound. This explains why the longitudinal cavity resonance properties do not affect the locked mode, despite being detuned from the free-running value. The slave still lases at the cavity mode but the injected light coherently sums with this light to shift the perceived output frequency. Hence, the laser can be a Fabry-Perot, DFB, DBR, or VCSEL, and the frequency-filtering effects of the laser structure will not affect the injection locking dynamics.



(a)



(b)

Figure 2.12 Phasor model of injection locking shows how steady-state is reached. (a) shows the evolution of the slave laser if lasing at its cavity mode. Since it is not locked, it rotates at a frequency of $\Delta\omega_R$. When locked to the master laser (b), the phasor is static by the addition of three vectors: 1) Phasor rotates by difference between master and slave frequencies. 2) Injected master light adds a real component. 3) Amplitude decreases due to reduced gain.

Chapter 3 Injection Ratio and Quality Factor

3.1 Motivation

Optical injection locking of semiconductor lasers can exhibit numerous enhancements over their free-running counterparts. Enhancement of modulation bandwidth [67-69] and suppression of non-linear distortion [5] and relative intensity noise [8, 9] have been reported. These effects exhibit themselves under the strong-injection regime. The strengths of these effects are predominantly functions of the ratio between the injected power from the master laser and the free-running power of the slave laser. Hence, the injection ratio, R , is an important parameter when implementing injection-locked laser systems.

In this chapter, we introduce a more physical and robust definition of injection ratio that is based on experimentally measurable values. We then derive a simple expression for the maximum resonance frequency enhancement ($\Delta\omega_{R,max}$) and utilize it as a figure-of-merit to compare injection-locked systems with a wide range of cavity lengths of slave lasers, from vertical cavity surface-emitting lasers (VCSELs) to edge-emitting lasers

(EELs) (Figure 3.1). We show that $\Delta\omega_{R,max}$ is inversely proportional to the quality factor (Q) of the lossless laser cavity and develop a time-bandwidth product that sets the fundamental tradeoff between cavity Q and resonance frequency enhancement. Finally, we show that the upper-locking range limit is synonymous to that developed for injection locking of electronic oscillators.

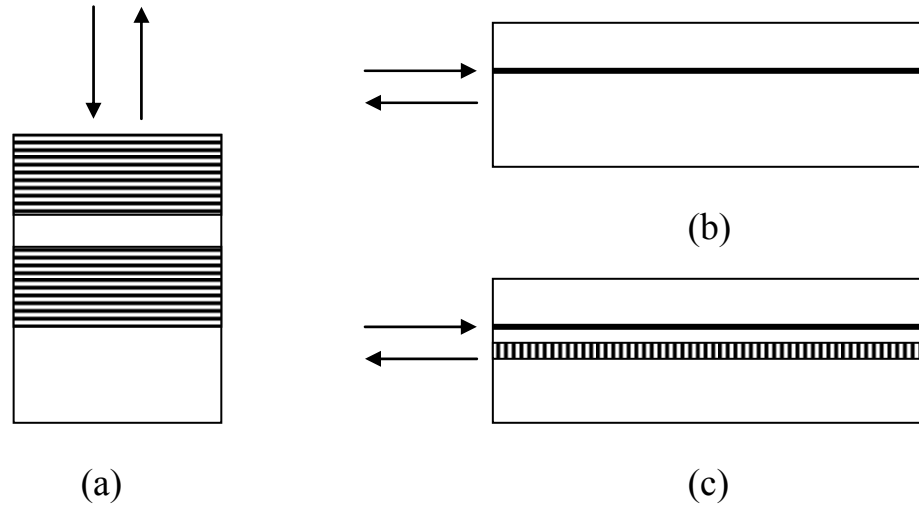


Figure 3.1 Injection locking of various laser structures: (a) VCSEL (b) Fabry-Perot (c) DFB.

3.2 Definition of Injection Ratio

3.2.1 Conventional Injection Ratio Definition

One of the most important parameters in injection locking is the injection ratio, R , typically defined as:

$$R = \left(\frac{A_{inj}}{A_0} \right)^2 = \frac{P_{inj}}{P_0} \quad (3.1)$$

where A_0 is the internal slave field magnitude, P_{inj} is the internal injected power and P_0 is the internal slave free-running power. Note that A_{inj} and A_0 are the injected and free-

running fields *inside* the cavity. This ratio is typically hard to calculate due to the losses of coupling from the lens to the facet and the facet mirror reflectivity. It is not empirically determined. Additionally, the lumped element model approximates the internal field as a single number. This is typically the average field over the laser cavity, as shown in Figure 3.2(a). However, for distributed feedback (DFB) lasers and other engineered-reflectivity lasers, the average field is not directly correlated to the output of the laser, making this injection ratio even harder to determine. The output of a laser is proportional to the field strength at the interface of the facet. DFBs can exhibit their peak field strength in the middle of the cavity, rather than typically at the two facets as in symmetric edge-emitters. Note that for this section we have chosen to ignore the change of the internal slave from its free-running value, when locked. The implications of the theory in this chapter deals with the positive detuning frequency side, where the free-running (A_{fr}) and internal locked-slave-field (A_{θ}) values are approximately equal.

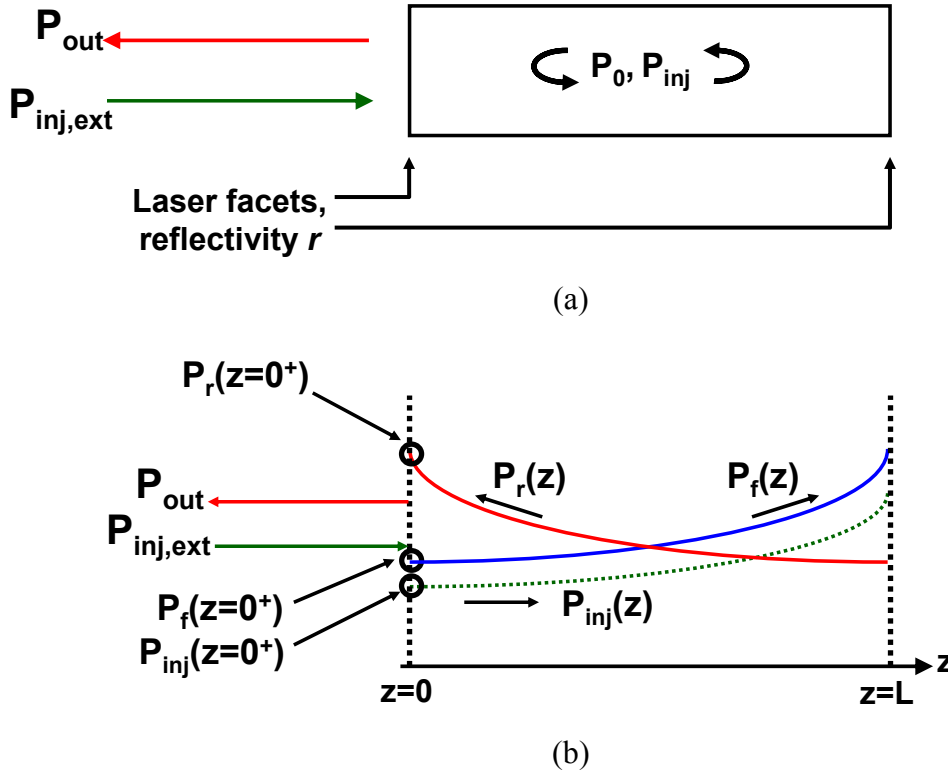


Figure 3.2 (a) Lumped-element model. (b) Distributed model showing the forward, reverse and injected power intensity along the cavity length.

3.2.2 External Injection Ratio

We can bypass these problems by defining an injection ratio based on externally-measurable parameters. The measurable power of the slave laser is the output from the injected facet. A wide-area detector can be used to collect all the light from this facet. Optical coupling from lenses to a fiber system can be calibrated. The measurable power of the master laser is the power incident to the slave laser facet. An external injection ratio can be defined using these two values:

$$R_{ext} = \frac{P_{inj,ext}}{P_{out}}. \quad (3.2)$$

where the powers on the right-hand-side are defined in Figure 3.2. Figure 3.2(b) shows the distributed power along the length of the laser. Forward- and reverse-propagating waves are shown as $P_f(z)$ and $P_r(z)$, respectively. $z = 0^+$ is the point just inside the left-hand laser facet and is not directly measurable. $z = 0^-$ is the point just outside the left-hand laser facet, and is a measurable value. Here, we define $P_{out} \equiv P_r(z = 0^-)$ as the free-running output power of the slave laser from the left facet. $P_{inj,ext} \equiv P_{inj}(z = 0^-)$ is the incident injected power from the master laser, just outside the cavity. We model the injected light as entering the facet, a fraction of which is lost due to mirror reflectivity, then combining with and propagating co-directionally with the forward-propagating wave of the slave. This external injection ratio is empirically measurable, but we must first relate the external injection ratio to the definitions in the conventional injection locking theory.

Note that any coupling loss due to the optical head or lens coupling mode mismatch can be calibrated out using a wide-area detector. For example, let us say we have a single-mode optical fiber with a microscope objective output. After aligning this output to the laser facet, we can then measure the power collected from the free-running laser. We can then remove the coupling apparatus and collect the free-running output with a wide-area detector, to ensure capture of all the light. Calculating the ratio of these two powers gives the coupling loss from the laser to the fiber. We can then apply time reversal to assume that the same coupling loss will be incurred when coupling from the fiber to the laser. Of course, mirror reflectivity must be factored in before knowing the actual amount of injected light that makes it into the laser, at point $z = 0^+$. This will be discussed in the next section.

3.2.3 Internal Injection Ratio

Conventional lumped-element theory uses an average value for the power of the slave and assumes the injected power distributes itself evenly along the cavity, as shown in (3.1). The problems with this definition are that it is difficult to relate these values to the external injection ratio, and they do not represent accurate values to apply to the theory. As we see in Figure 3.2(b), the powers are not equal along the laser cavity. Choosing an average value would not be accurate, especially for a laser with low-reflectivity mirrors or distributed mirrors such as DFBs. For example, a DFB with a peak power intensity in the middle of the cavity would have relatively low powers at the facets and low output powers, despite having a large photon density.

Since we are attempting to describe a lumped-element model using a real device, we must choose two numbers to describe the injection ratio. Examining the model in Figure 3.2(b), we find we have many choices as to where we wish the lumped-element value to represent. Using Figure 3.2(b), we assume that the injected light transmitted through the facet travels in parallel with the forward-propagating wave of the internal slave field. Hence, it experiences a nearly-identical gain as the internal slave field and grows via stimulated emission. Therefore, the ratio of powers between the injected field and the forward-propagating slave field at $z=0^+$ will remain relatively constant along all points of the laser cavity. Once the two fields hit the right facet, they both experience similar mirror losses before reflecting in the reverse direction. Again, they maintain the same ratio of powers until they return to the left facet. Since the ratio is equivalent at any point along the cavity, we can choose to define the internal injection ratio at any point and propagation direction as the ratio of the injected field over the slave field *at that point*:

$$R_{int} = \frac{P_{inj}(z)}{P_f(z)} \quad (3.3)$$

where $P_{inj}(z)$ and $P_f(z)$ are the injected power and slave power in the forward direction. Given this freedom, we choose to define the internal injection ratio at $z=0^+$ in the forward-propagating direction:

$$R_{int} = \frac{P_{inj}(z=0^+)}{P_f(z=0^+)}. \quad (3.4)$$

Equation (3.4) will be the working definition of internal injection ratio in this dissertation. This is a more accurate and physical definition than the simplistic definition in (3.1). In summary, defining the injection ratio as the average powers inside the cavity leads to inaccuracies. Defining the ratio at the facets leads to a more physical and accurate definition.

The accuracy of both was verified by comparing the lumped element simulations to that of a distributed model simulation. The same laser parameters were used for each. The injection ratio was first calculated by dividing the injected power by the average steady-state power of the free-running laser. This equates to the definition in (3.1). Then, we defined the injection ratio using (3.4). The latter definition was found to match the lumped element model, while the former did not, thus confirming the improved accuracy of the new definition.

3.2.4 Relating Internal to External Injection Ratios

The definition of internal injection ratio in (3.4) is a convenient value because we can directly relate it to the external powers through the mirror reflectivity, r , of the left facet:

$$(1-r)P_{inj,ext} = P_{inj}(z=0^+), \quad (3.5)$$

$$(1-r)P_r(z=0^+) = P_{out}, \quad (3.6)$$

$$rP_r(z=0^+) = P_f(z=0^+). \quad (3.7)$$

Finally, combining (3.5)-(3.7) with (3.4), we can relate the internal injection ratio with the external injection ratio:

$$\frac{R_{int}}{R_{ext}} = \frac{(1-r)^2}{r}. \quad (3.8)$$

Note that this relates the internal injection ratio commonly used in theoretical papers with the external injection ratio, which is easily determinable by empirical methods. We may substitute R_{int} as defined in (3.4) for any theory that uses an injection ratio, R , as defined in (3.1):

$$\left(\frac{A_{inj}}{A_0} \right)^2 \Rightarrow R_{int}. \quad (3.9)$$

Then we use (3.8) to relate the internal injection ratio to an experimentally-determinable ratio, R_{ext} . Note also that (3.8) works only for reflection-type injection locking experiments. Equation (3.8) is plotted versus mirror power reflectivities in Figure 3.3. Figure 3.3 shows that for extremely-high mirror reflectivities (on the order typically used for VCSELs), much of the incident injected light does not transmit into the cavity.

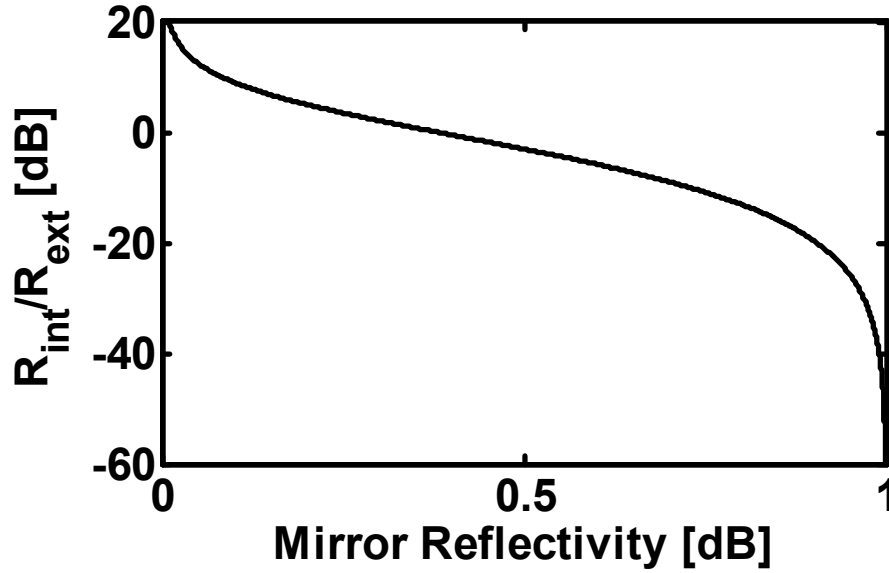


Figure 3.3 Ratio of internal and external injection ratios for different mirror reflectivities.

3.3 Maximum Resonance Frequency Enhancement

The coupling coefficient, κ , for injection-locked lasers has been shown to be important for determining the efficiency of the injection process. It is typically defined as [32]:

$$\kappa = \frac{1}{\tau_{rt}} = \frac{v_g}{2L} \quad (3.10)$$

where τ_{rt} is the cavity roundtrip time, v_g is the cavity group velocity, and L is the cavity length. Physically, it means that the injected light must distribute itself across the entire laser cavity. Therefore, longer cavities seem to have poorer injection efficiencies; the longer cavity dilutes the injection's effects. Table 3.1 illustrates this difference between VCSELs and edge-emitting lasers (EELs). A VCSEL with $L = 2 \mu\text{m}$ versus an EEL with $L = 500 \mu\text{m}$ would benefit from a κ that is 250 times larger than its EEL counterpart.

	VCSEL / EEL
Cavity length, L	$\frac{L_{VCSEL}}{L_{EEL}} = \frac{2\mu m}{500\mu m}$
Coupling rate, κ	$\frac{\kappa_{VCSEL}}{\kappa_{EEL}} = \frac{500\mu m}{2\mu m} = 250$

Table 3.1 Comparison of coupling rates of VCSELs and EELs.

The resonance frequency enhancement, found in (2.32), can be rewritten using (3.4):

$$\Delta\omega_R = \left| \kappa \sqrt{R_{int}} \sin \phi_0 \right|. \quad (3.11)$$

The resonance frequency enhancement reaches its maximum when $\sin \phi_0 = -1$, or $\phi_0 = -\pi/2$, which occurs at the positive edge (upper bound) of the stable locking range [36]:

$$-\kappa \sqrt{R_{int}} \sqrt{1 + \alpha^2} < \Delta\omega < \kappa \sqrt{R_{int}}. \quad (3.12)$$

Using (3.10), (3.11) and the upper bound of (3.12), we obtain the maximum resonance frequency enhancement for a given injection ratio:

$$\Delta\omega_{R,max} = \kappa \sqrt{R_{int}} = \frac{v_g}{2L} \sqrt{R_{int}}. \quad (3.13)$$

This equation is only dependent on the cavity round-trip time and the injection ratio. The equation uses Mogensen's locking range, not the one implied by the dynamic R.O.C. stability criteria. However, the unstable regime shrinks with lower slave current biases. Additionally, the unstable regimes collapses as we increase the injection ratio into the strong injection regime. Equation (3.13) suggests that a high resonance frequency enhancement would favor short-cavity lasers. In other words, our VCSEL example above would have a 250 times larger resonance frequency enhancement than the EEL.

However, one must remember that short-cavity-lasers require high-reflectivity mirrors, which reduce the internal injection ratio as shown in Figure 3.3. To find the trade-off between cavity length and mirror reflectivity, we use (3.8) to relate (3.13) to the external injection ratio:

$$\Delta\omega_{R,\max} = \frac{v_g}{2L} \cdot \frac{1-r}{\sqrt{r}} \sqrt{R_{ext}} . \quad (3.14)$$

Figure 3.4 shows a comparison of $\Delta\omega_{R,\max}$ between a typical EEL and VCSEL versus the external injection ratio. Using R_{ext} allows for a fair comparison between the two types of lasers, since the injection source should be the same and their free-running output powers should be roughly equivalent. As postulated, the VCSELs high coupling coefficient, κ , is compensated by the decreased efficiency of injection transmission from outside to inside the cavity. This results in an almost equivalent maximum resonance frequency enhancement for VCSELs and EELs.

Equation (3.14) states that to obtain the maximum resonance frequency enhancement, aside from increasing the external injection ratio, one must choose a short cavity laser and a laser with low mirror reflectivity. However, the trade-off is that lowering these two values leads to decreased photon lifetimes and higher threshold powers. In order to optimize the resonance, we can engineer the two facets' reflectivity via anti- or high-reflection coatings. In reflection-style injection locking of edge-emitting lasers, we can compensate the lowering of the input facet reflectivity by raising the reflectivity of the output facet.

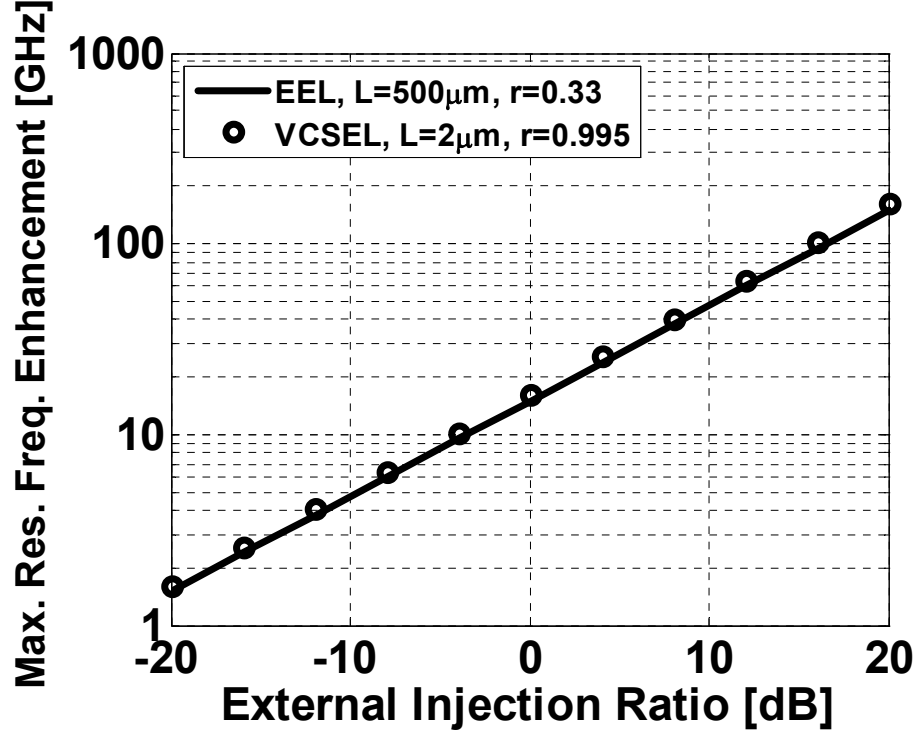


Figure 3.4 Maximum resonance frequency enhancement versus external injection ratio for a typical EEL and VCSEL.

In order to study the effects of both cavity length and mirror reflectivity on the maximum resonance frequency enhancement, we functionalize mirror reflectivity with respect to cavity length. Since we cannot choose any arbitrarily low cavity length and mirror reflectivity, a fair comparison can be made by choosing the mirror reflectivity for a given cavity length that will minimize the current needed to achieve a 1 mW output power. Given $P_0 = 1$ mW, we solve

$$P_0 = \left(\frac{\alpha_m}{\alpha_i + \alpha_m} \right) h\nu (J - J_{th}) \quad (3.15)$$

for J . Here, $h\nu$ is the photon energy, J_{th} is the threshold current, α_i is the distributed intrinsic material loss, and α_m is the distributed mirror loss. We see that the output power

is a function of the mirror loss. The threshold current also depends on α_m , since the threshold gain is:

$$g_{th} = v_G(\alpha_m + \alpha_i) = v_G g_0 \ln\left(\frac{N_{th}}{N_r}\right) \quad (3.16)$$

where g_0 is the logarithmic differential gain coefficient. The threshold current is proportional to the threshold carrier number:

$$J_{th} = \gamma_N N_{th}. \quad (3.17)$$

Then, solving for current in (3.15) as a function of α_m , using (3.16) and (3.17), we get:

$$J(\alpha_m) = \gamma_N N_r \exp\left(\frac{\alpha_m + \alpha_i}{g_0}\right) + \frac{P_0}{h\nu} \left(\frac{\alpha_m + \alpha_i}{\alpha_m}\right). \quad (3.18)$$

To find the value of α_m that minimizes J , we take the derivative w.r.t. α_m , and set to 0:

$$\alpha_m^2 \exp\left(\frac{\alpha_m}{g_0}\right) = \frac{P_0 \alpha_i g_0}{h\nu \gamma_N N_r} \exp\left(-\frac{\alpha_i}{g_0}\right). \quad (3.19)$$

One can solve this numerically, but it is sufficient to note that it is a monotonic function of the r.h.s. Typically, the only variable parameter is the desired optimized output power. Higher output powers require larger α_m 's to minimize the bias current. Therefore, the laser parameters and the desired minimized output power determine the optimum α_m for this system. Once α_m is determined, we have a relationship between r and L :

$$\alpha_m = \frac{1}{L} \ln\left(\frac{1}{r}\right). \quad (3.20)$$

Solving for r and substituting into (3.14) yields an equation for the resonance frequency enhancement w.r.t. only L :

$$\Delta\omega_{R,\max} = \frac{v_G}{2L} \left[\exp\left(\frac{\alpha_m L}{2}\right) - \exp\left(-\frac{\alpha_m L}{2}\right) \right] \sqrt{R_{\text{ext}}} . \quad (3.21)$$

We scan the cavity length, L , from 1 μm to 1000 μm , for a representative value of mirror loss ($\alpha_m = 30 \text{ cm}^{-1}$) and injection ratio ($R_{\text{ext}} = 0 \text{ dB}$). Figure 3.5 shows a plot of the maximum resonance frequency enhancement in (3.21). Additionally, we plot the corresponding reflectivity for the given mirror loss, shown in green. As Figure 3.5 shows, the optimal mirror reflectivity goes up when the cavity length goes down. Furthermore, the maximum resonance frequency enhancement varies by only 30% as the length changes by 3 orders of magnitude, for any typical laser lengths. This shows that the maximum resonance frequency enhancement of an optimized laser does not vary by much for VCSELs or edge-emitting lasers of typical lengths. For lengths greater than 1 mm, however, the optimum reflectivity becomes quite small ($< 10\%$) and it seems that the maximum resonance frequency enhancement becomes larger. It would be interesting to explore the resonance enhancement for external-cavity or fiber lasers. Changing the injection ratio simply scales the resonance enhancement. However, optimizing for higher output powers requires larger mirror losses. The effect of this is shown in Figure 3.6. Higher mirror losses actually increase the maximum resonance frequency enhancement. This phenomenon is formally quantified in the next section.

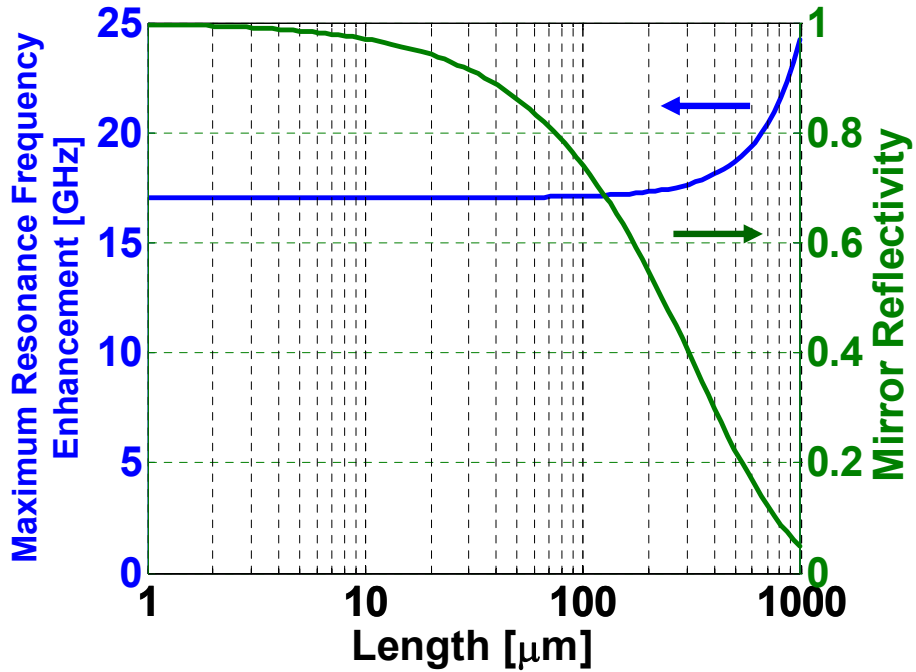


Figure 3.5 Right axis: mirror reflectivity for a laser whose optimum $\alpha_m = 30 \text{ cm}^{-1}$ (corresponding to a minimized current for $P_o = 2\text{mW}$, for typical laser parameters). Left axis: maximum resonance frequency enhancement at $R_{ext} = 0\text{dB}$ for this mirror loss.

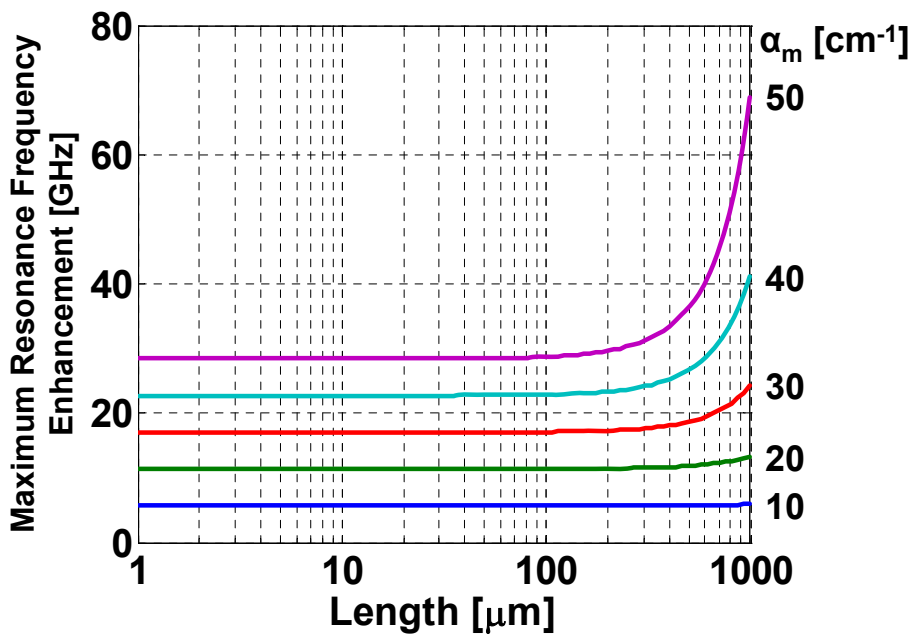


Figure 3.6 Graph of maximum resonance frequency enhancement for different optimized α_m .

3.4 Fundamental Limit of the Maximum Resonance Frequency Enhancement Factor Based on Coupling Quality Factor

The previous section attempted to provide design rules for laser resonance frequency optimization w.r.t. power and current. Here, we develop a fundamental theory that governs the figure-of-merit that is generalized for all resonator structures.

Note that the quality factor of a loss-free Fabry-Perot cavity (coupling Q) with mirror reflectivities of r and a cavity length of L is [70]:

$$Q \equiv \frac{\omega_0}{\omega_{1/2}} = \frac{\omega_0 L}{v_g} \cdot \frac{\sqrt{r}}{1-r} \quad (3.22)$$

where ω_0 is the laser frequency and $\omega_{1/2}$ is the full-width-at-half-maximum (FWHM) width of the cavity resonance. $\Delta\omega_{R,\max}$, can then be simplified to:

$$\Delta\omega_{R,\max} = \frac{\omega_0}{2Q} \sqrt{R_{\text{ext}}} . \quad (3.23)$$

This equation removes the dependency of the resonance frequency enhancement from r and L , and relates it to a single cavity parameter: Q . It also states, perhaps counter-intuitively, that to obtain a high resonance frequency, we should design a laser cavity with a low Q . Interestingly, a typical EEL with $L = 500 \mu\text{m}$ and $r = 0.3$ has the same Q ($= 6.7 \cdot 10^3$) as a typical VCSEL with $L = 2 \mu\text{m}$ and $r = 0.995$. This could explain the similarities between the maximum resonance frequencies of the two laser geometries. Equation (3.23) states that both lasers would have the same maximum resonance frequency enhancement. As we intuited previously, the VCSEL's high coupling coefficient, κ , is compensated by the decreased ratio of injected light that is successfully transmitted into the cavity.

In order to validate our theory, we fit our theory to a survey of experimental data throughout the literature [39, 67, 71-74], shown in Figure 3.7. It should be noted that $\Delta\omega_{R,max}$ is calculated from the free-running resonance frequency, ω_{R0} , and the enhanced resonance frequency, ω_R . The two can be related through (2.31):

$$\omega_R^2 = \omega_{R0}^2 + \Delta\omega_R^2 \quad (3.24)$$

We assume that the resonance frequencies found in the literature had been optimized to the maximum value they could obtain for their given injection ratio. The data in Figure 3.7 includes eight different lasers. For each laser, the $\Delta\omega_{R,max}$ -vs- R_{ext} curve fits well with a straight line with a slope of $\frac{1}{2}$ in logarithmic scale, agreeing well with the prediction by (3.23). The offset among the curves indicate these lasers have different Q values. Laser DFB1 and DFB2 were from the authors' own distributed feedback (DFB) lasers ($\kappa_{grating}L = 4$). The Q values extracted from Figure 3.7 are $8.5 \cdot 10^3$ and $14.1 \cdot 10^3$ for DFB1 and DFB2, respectively. From Yariv [70], DFBS with a $\kappa_{grating}L = 4$ and no cleaved facets will have a Q of $8.3 \cdot 10^3$, well within the variability of random phases in cleaved facets. To perform a more comprehensive study, an anti-reflection coating should be used to remove random phase conditions at the facets. The extracted Q 's for other lasers in Figure 3.7 also show reasonable agreement with the values estimated from the device parameters reported in the literature.

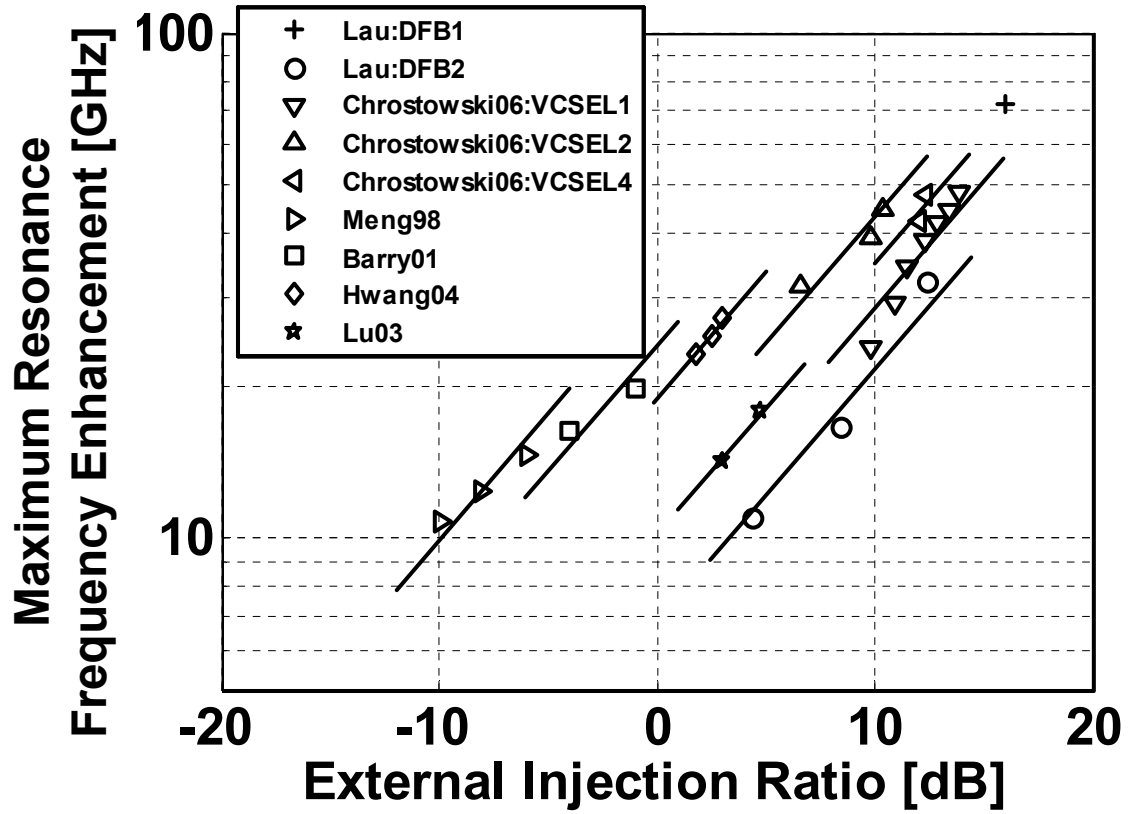


Figure 3.7 Comparison of theory with experimental data for maximum resonance frequency enhancement.

3.5 Time-Bandwidth Product

The photon lifetime due to the mirror coupling loss is defined as τ_c . We can relate it to the FWHM linewidth of mirror loss, $\omega_{1/2}$ [75]:

$$\omega_{1/2} = \frac{1}{\tau_c}. \quad (3.25)$$

Using (3.22), (3.23) and (3.25), we obtain:

$$\tau_c \cdot \Delta\omega_{R,\max} = \frac{1}{2} \sqrt{R_{\text{ext}}}. \quad (3.26)$$

Equation (3.26) can be viewed as a time-bandwidth product, which increases with higher injection ratio. This sets a fundamental engineering trade-off between high resonance frequency and low threshold currents.

3.6 Analogy to Electrical Oscillators

We can also use (3.23) to delineate the upper edge of the locking range. Interestingly, Adler [21] and similarly Slater [76] cite an identical boundary on the locking range of injection-locked electronic oscillators:

$$\Delta\omega = \frac{\omega_0}{2Q} \sqrt{\frac{P_i}{P_0}} \quad (3.27)$$

where $\Delta\omega$ is the detuning frequency and Q is again the coupling Q . The similarity between electronic and optical oscillator theory suggests that the theory is universal to all types of oscillators, including different optical cavity designs, and that coupling Q is the main factor affecting the resonance frequency for a given injection ratio. It would be useful to further explore the resonance frequency enhancement via different cavity designs, such as fiber ring lasers or micro-cavities.

3.7 Summary

In summary, we have derived a universal formula for the maximum resonance frequency enhancement of an injection-locked semiconductor laser in terms of the quality factor (Q) and the external injection ratio of the slave laser. The enhancement increases with the square root of the external injection ratio but decreases with Q . With this model, we find that typical lasers of different lengths have comparable performance for the same external injection ratio, provided they have similar Q . The theory agrees well with the

experimental data reported in the literature, including those from the authors' laboratory. Finally, we show that the time-bandwidth product of injection-locked lasers is equal to one-half of the square root of the external injection ratio. The results presented here clearly identify the design trade-off between the threshold of the laser and the maximum resonance frequency enhancement, and can serve as a guideline to optimize the performance of injection-locked lasers.

Chapter 4 Heterodyne Detection

4.1 Motivation

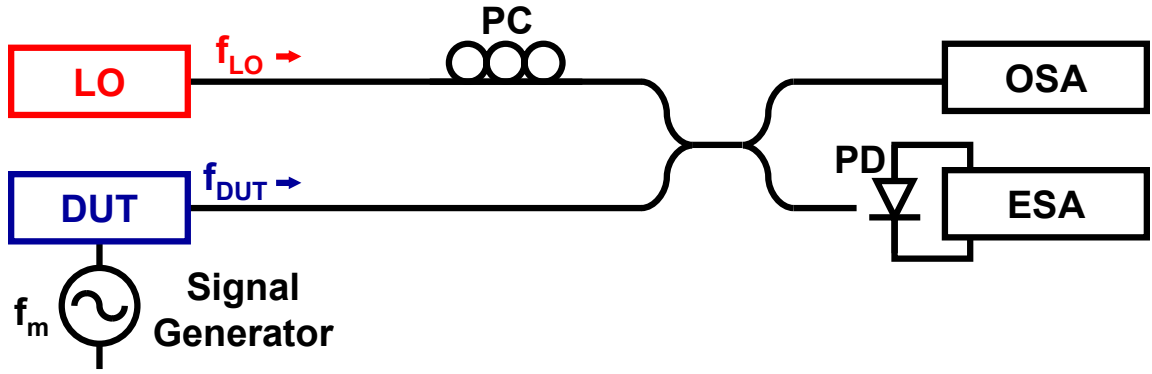
The development of high speed electro-optic devices has seen a recent increase in speed. Electro-optic modulators (EOM) have been reported with speeds >75 GHz for LiNbO_3 EOMs [77], >50 GHz for GaAs EOMs [78], and 150 GHz for polymer EOMs [79]. 100 GHz polymer EOMs are currently available commercially (Lumera Corporation). Electro-absorption modulators (EAM) have reached measured bandwidths of 50 GHz and model-extrapolated bandwidths of 90 GHz [80, 81]. Directly-modulated semiconductor lasers have achieved bandwidths of 43 GHz [82]. As the bandwidth of these devices becomes increasingly higher, the need for simple and inexpensive testing methods becomes greater.

A basic system for measuring the frequency response of an electro-optic device consists of 1) a modulation source 2) a photodetector (PD) and 3) an electrical spectrum analyzer (ESA). The maximum measurable frequency response may be bottlenecked by

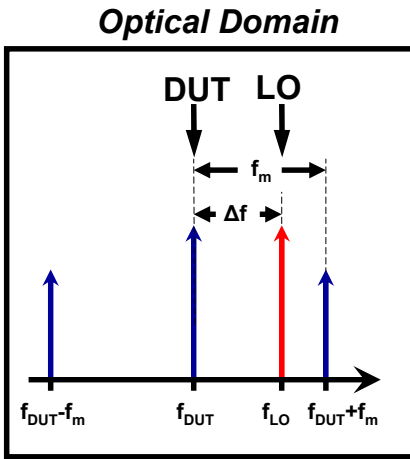
any or all of these components. Specifically, direct measurement of electro-optic devices are usually limited by the maximum bandwidth of the photodetector, typically 50 to 60 GHz. Additionally, high-speed photodetectors and network analyzers (> 65 GHz) can be prohibitively expensive.

Several techniques for measuring the frequency response of transmission-style modulators (EOMs and EAMs) have been reported [83-86]. Heterodyne detection mixes the modulation sidebands of an optical modulator with a local oscillator (LO) laser. If the LO frequency is tuned close to the sideband, the beat tone amplitude will be proportional to the field strength of the LO and the modulation, and can be detected with a low-frequency PD and ESA. However, heterodyne systems are typically complex and costly due to the phase drift between the signal and LO lasers, necessitating a phase-locking feedback mechanism and a high-frequency electrical oscillator and mixer [87].

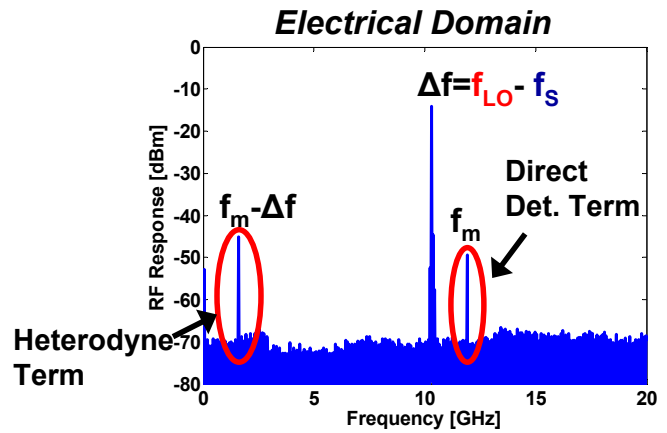
In this chapter, we demonstrate a heterodyne detection system that removes the need for phase-locking or feedback by relying on the slowly-varying nature of the frequency and phase drift.



(a)



(b)



(c)

Figure 4.1 Basic heterodyne detection principle. (a) Schematic of heterodyne detection system. (b) Optical spectrum, showing the LO line at f_{LO} (red), DUT line at f_s (tall, blue), and its modulation sidebands at $f_s \pm f_m$ (2 short, blue). (c) Electrical spectrum, showing the beating between DUT and LO fundamental lines (Δf); the direct detection term (f_m) was created by the beating between the DUT and its sidebands; and the down-converted heterodyne term ($f_m - \Delta f$), created by the beating between the LO and the modulation sideband closest to it.

4.2 Theory

A basic optical heterodyne signal can be created using a simple setup, as shown in Figure 4.1(a). The device-under-test (DUT) can either be a laser or a modulator with a laser input. This setup assumes that the LO and DUT are phase-locked and this subsystem is removed for clarity. The LO and DUT outputs are combined using a 3-dB

coupler and then sent to a PD/ESA or an optical spectrum analyzer (OSA). To ensure the polarizations are matched, a polarization controller (PC) is used. In Figure 4.1(a) and (b), we show the LO laser line in red. The optical power and frequency are P_{LO} and f_{LO} , respectively. The DUT laser line is shown in dark blue with an optical power and frequency of P_{DUT} and f_{DUT} . The summation of the two laser lines, P_{LO} and P_{DUT} , as received in the photodetector is:

$$P_{tot} = P_{LO} + P_{DUT} + 2\sqrt{P_{LO}P_{DUT}} \cos(\Delta\omega t + \Delta\theta), \quad (4.1)$$

where P_{LO} and P_{DUT} are the optical powers of the LO and DUT, respectively, and $\Delta\omega$ and $\Delta\theta$ are the angular frequency and phase difference between the LO and DUT optical laser lines. Here, $\Delta f = f_{LO} - f_{DUT}$, where $\Delta\omega = 2\pi\Delta f$.

On an ESA, a beat tone at Δf and proportional to $\sqrt{P_{LO}P_{DUT}}$ will be observed, as shown in Figure 4.1(c). By knowing the power of the local oscillator, the magnitude of the DUT can be determined. In the example in Figure 4.1, the LO was placed approximately +10 GHz above the DUT fundamental. The modulation was set to 12 GHz, creating sidebands with power P_M . In the same manner as (4.1), a beat tone at f_m and proportional to $\sqrt{P_{DUT}P_M}$ will be observed. We can extract the strength of the modulation by knowing the DUT fundamental line's power and then solving for P_M . For the sake of argument, if our detection system bandwidth was capped at 11 GHz, the direct detection term could not be measured. However, the difference between LO and the blue-side modulation sideband is $12 - 10 = 2$ GHz, well within the bandwidth of the detection system. Hence, a beat tone at $|f_m - \Delta f|$ and proportional to $\sqrt{P_{LO}P_M}$ will be observed. We can then extract the modulation power simply by knowing the LO power.

If, however, the frequencies and phases of the two lasers are not locked together at a fixed difference, as is typically the case without a phase-locking mechanism, there will be a time dependence associated with $\Delta\omega$ and $\Delta\theta$:

$$P_{tot} = P_{LO} + P_{DUT} + 2\sqrt{P_{LO}P_{DUT}} \cos[\Delta\omega(t)t + \Delta\theta(t)], \quad (4.2)$$

making the measurement of the magnitude of the beat tone difficult. The frequency and phase fluctuations have many sources, including noise from current sources, spontaneous emission, etc. The large-signal frequency fluctuations are typically caused by mechanical vibrations of the lasers' frequency-selection method or temperature variations in the laser medium's refractive index. Both of these fluctuation sources are slowly varying, with a bandwidth typically not exceeding MHz.

4.3 Method

If we assume that the large-signal frequency drift is sufficiently small and low-frequency, which is typically the case, one can capture its value on an ESA. Here, we assume that the frequency will not vary more than the resolution bandwidth during the time frame of the sampling. The method to measure the power of the DUT is described here:

1. Tune the LO frequency close to the DUT frequency, until the beat frequency is within the bandwidth of the PD and ESA.
2. Center the ESA frequency to that of the approximate frequency difference, Δf . On repeated frequency sweeps, the ESA will show a peak that jumps in frequency (akin to frequency jitter on a ms time scale).

3. Zoom the span until it is larger than the range of frequency peaks and set the resolution bandwidth just large enough for the peaks to be approximately the same magnitude. The magnitude of the beat term will be equal to the height of these peaks.

To measure the modulation frequency response of a DUT, the process is the same, except replace the DUT fundamental line with one of the modulation sidebands (we choose blue side for this example). We place the LO at a frequency Δf away from the DUT fundamental line, such that f_{LO} is close to the modulation sideband $f_{DUT} + f_m$. We then modulate the DUT at a frequency f_m and then measure the beat frequency at $|f_m - \Delta f|$ (as shown in Figure 4.1(b) and (c)). For each value of f_m , we can keep the LO frequency fixed, but the center frequency of the ESA must be changed to $|f_m - \Delta f|$.

Hence, by tuning the LO close to one of the modulation sidebands, the beat frequency can be down-converted to a frequency that is within the bandwidth of the PD and ESA. The magnitude of the modulation can be determined by simply knowing the magnitude of the LO. The system removes the necessity for any complicated phase-locking or feedback.

The trade-off of this system is that the faster the fluctuations in frequency of $\Delta\omega$, the larger the resolution bandwidth or the shorter the sampling time must be to ensure the beat note does not drift out of the sampling window during the sampling time. The system allows unlimited detectable modulation frequency, within the tuning range of the LO. From (4.1), we can also see that we can get heterodyne gain if the LO power is at

least $\sqrt{2}$ times larger than the DUT fundamental. Finally, the LO or DUT need not be ultra-stable.

Figure 4.2 shows a calibrated comparison between the direct detection of a directly-modulated DFB laser and the heterodyne technique described here. The DFB laser was a 1550 nm capped-mesa buried heterostructure (CMBH) laser biased at 3.5 times threshold [88]. The LO was an external-cavity tunable laser (SDL 8610). We used an Agilent 83650B 10 MHz to 50 GHz swept signal generator, an Agilent 8565E 30 Hz to 50 GHz spectrum analyzer, and an Agilent 83440D DC to 34 GHz PD for our experiments. Here, we placed the LO 10 GHz away from the DUT fundamental. Modulation from 10 to 20 GHz was applied. Hence, the heterodyne term swept from ~ 0 to 10 GHz; a lower-frequency signal than the modulation, and proof of the concept. Since this was a comparison, the modulation frequencies were kept intentionally small so we could measure the direct-detection term simultaneously. Here, we see a heterodyne gain of approximately 8 dB around 10 to 14 GHz. Above 14 GHz, the gain is gradually lost until the magnitudes are almost identical at 20 GHz. This discrepancy could possibly be due to asymmetric phases of the modulation sidebands, which can cause a change in the direct detection term, as described in Section 4.4. Note that the heterodyne detection is immune to these effects. Otherwise, the shape of the resonance peak as well as the roll-off is well preserved in the heterodyne detection scheme, validating our system.

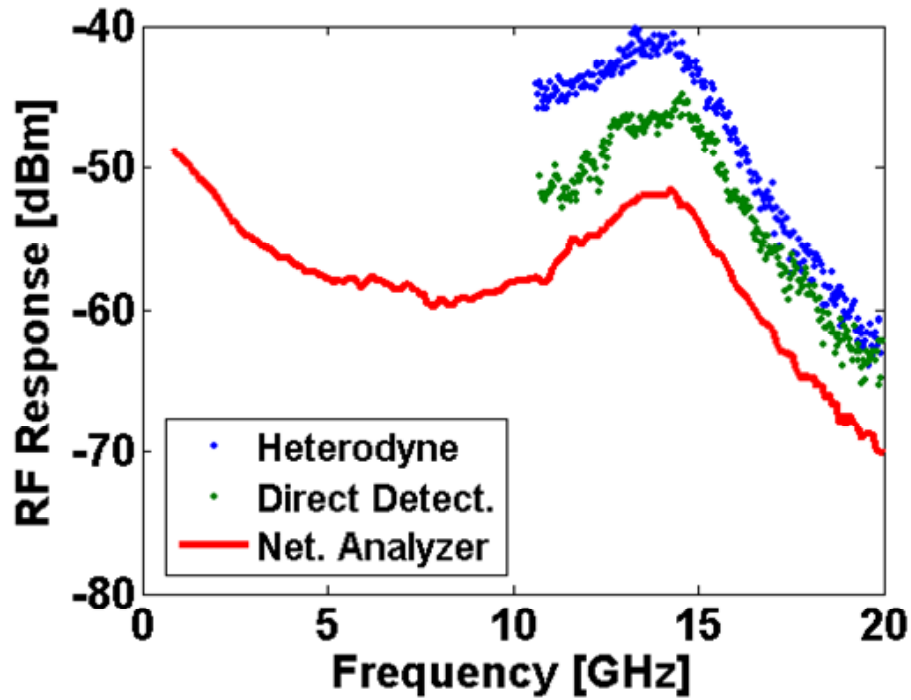
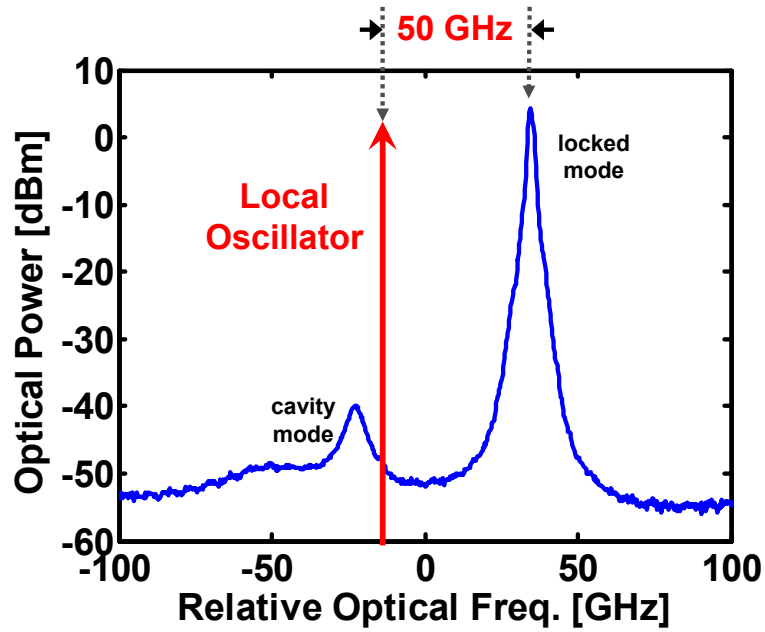


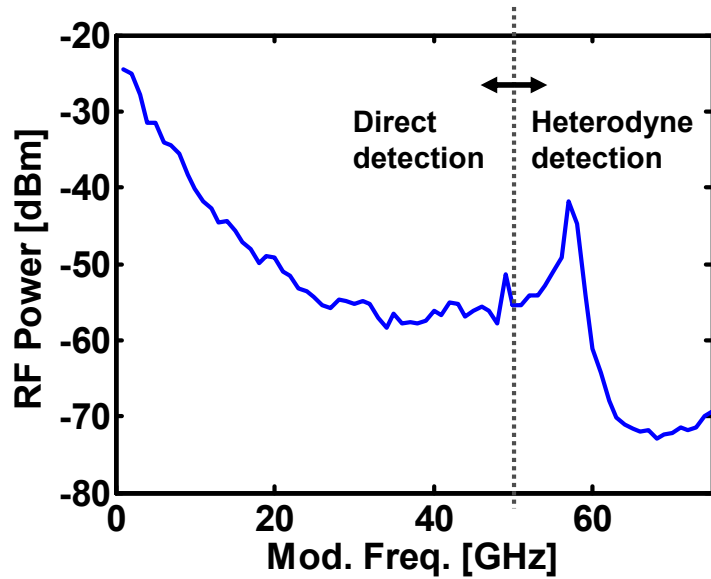
Figure 4.2 Heterodyne and direct detection comparison.

In Figure 4.3, we show a frequency response that goes beyond the limitations of our direct detection equipment. The full response was constructed from two separate responses. The first part (left part in Figure 4.3(b)), from 0-50 GHz, was acquired using direct detection, calibrating the photodetector, microwave cables, synthesizer, and ESA. The second part (right part in Figure 4.3(b)), from 50-75 GHz, was acquired using the heterodyne detection technique. The LO is tuned to 50 GHz below the frequency of the master laser (Figure 4.3(a)). The red side is chosen so that the modulation sideband that is cavity mode-enhanced will be selected. We then use a 50-75 GHz mm-wave source module to modulate the laser and use the heterodyne detection system to measure the frequency response. Since $\Delta\omega \approx 50$ GHz, the down-converted modulation frequency would be around 0-25 GHz, well within the bandwidth of both the PD and ESA. Since

the responses at 50 GHz are redundant, we can use it as a calibration point when joining the two parts together.



(a)

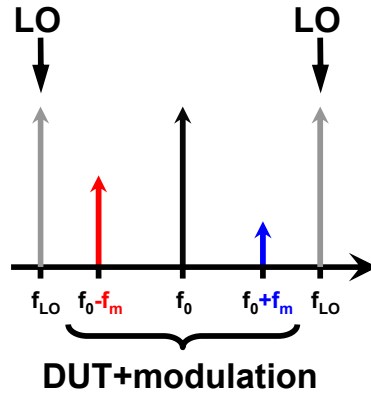


(b)

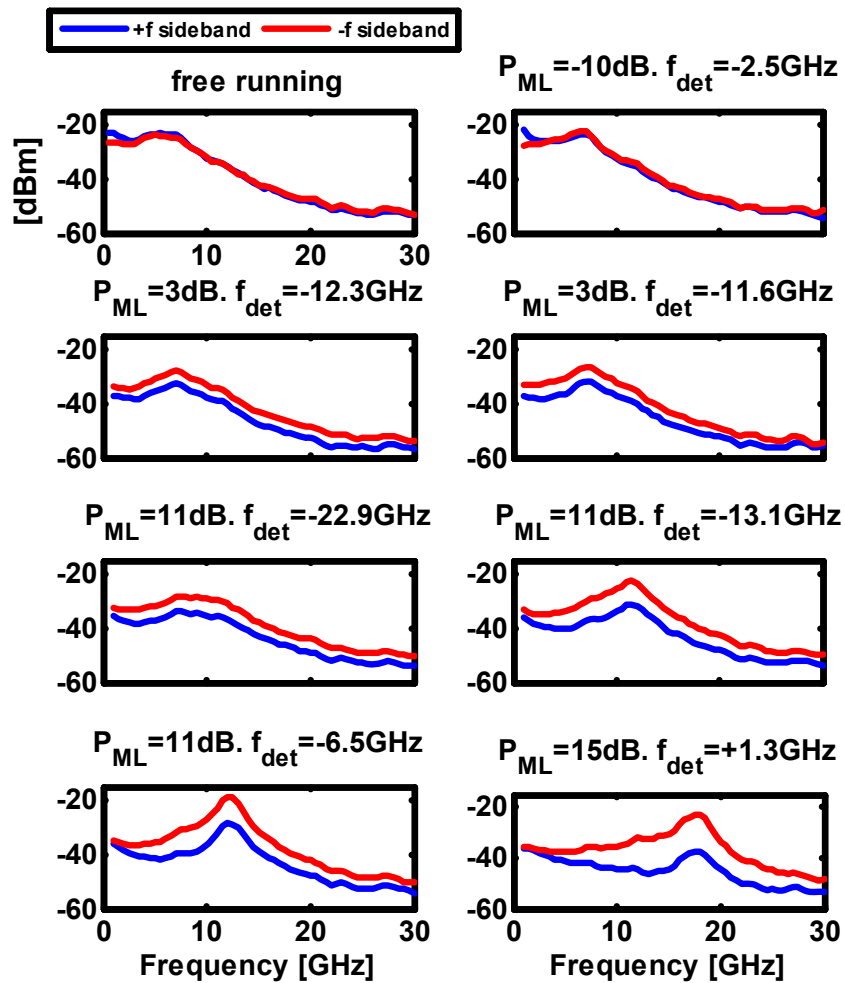
Figure 4.3 Heterodyne detection of frequency response from 0-75 GHz. (a) Optical spectrum of the injection-locked laser, showing the position of the local oscillator. (b) Frequency response, consisting of the two concatenated parts.

4.4 Modulation Sideband Separation

Modulation usually creates two optical sidebands, one on each side of the fundamental line. If these two sidebands are not symmetric in amplitude (see Figure 4.4(a)), direct detection will not resolve this asymmetry. By using a heterodyne detection system, we can separate the sidebands and determine the asymmetry. If the LO was placed on the high frequency side (right-hand side in Figure 4.4(a)), the beat frequency between the LO and upper sideband, $f_{LO} - (f_0 + f_m)$, would be much lower frequency than that between the LO and lower sideband, $f_{LO} - (f_0 - f_m)$. Hence, we would be able to plot the magnitude of the upper sideband. Similarly, we can do the same for the lower sideband. This is shown in Figure 4.4(b) for an injection-locked laser at different injection ratios and detuning frequencies. One can see that the modulation strength of the lower sideband contributes much more than the upper sideband. This corroborates with the cavity mode model that was explained in Section 2.7. For small injection ratios, the sidebands are quite symmetric. For larger injection ratios, the asymmetry increases, looking increasingly like single-sideband modulation [15]. For the last case, where $P_{ML} = 15$ dB, and is the largest injection ratio case, the sideband asymmetry is at its largest: 14.6 dB at 18 GHz. The asymmetry is quite broadband as well, giving >10 dB asymmetry for a bandwidth of 10 GHz.



(a)



(b)

Figure 4.4 Measurement that separates and shows the asymmetry of modulation sidebands. (a) Frequency domain representation of the separation. (b) Frequency response of an injection-locked laser at different injection ratios and detuning frequencies.

4.4.2 Quantifying the Sideband Asymmetries

When the modulation sidebands of a modulated signal are asymmetric and their phases are not complex conjugates, direct detection can not resolve these asymmetries. If we describe the fundamental laser line field with a complex phasor as:

$$\tilde{E}_0 \propto \sqrt{P_0} \exp j[\omega_0 t + \phi_0], \quad (4.3)$$

where P_0 , ω_0 , and ϕ_0 are the optical power, frequency and phase of the fundamental mode, then the upper (\tilde{E}_+) and lower (\tilde{E}_-) sidebands can be described generally as:

$$\tilde{E}_\pm \propto \sqrt{P_\pm} \exp j[(\omega_0 \pm \omega_m)t + \phi_\pm]. \quad (4.4)$$

The power is then proportional to:

$$P \propto |\tilde{E}_0 + \tilde{E}_+ + \tilde{E}_-|^2. \quad (4.5)$$

The power at the beat frequency, ω_m , is then equal to:

$$P(\omega_m) = 2\sqrt{P_0} \sqrt{P_+ + P_- + 2\sqrt{P_+ P_-} \cos(\Delta\phi_+ + \Delta\phi_-)} \quad (4.6)$$

where the phase difference, $\Delta\phi_\pm \equiv \phi_0 - \phi_\pm$, is the difference in phases between the fundamental and each sideband. We can measure $P(\omega_m)$ by direct detection and find the magnitudes of P_+ and P_- by heterodyne detection. Hence, by (4.6), the sum of the phase differences can be determined. This may have potential application in characterizing optoelectronic devices for determining effects of chromatic dispersion.

Chapter 5 High-Frequency Injection-Locked Lasers

5.1 Motivation

High-speed modulation of semiconductor lasers has been a topic of avid research for the past two decades. The drive to develop increased bandwidth lasers for direct modulation has been fueled by commercial telecommunications applications, as well as high-end radar and sensing systems. Table 5.1 shows the current state-of-the-art for direct modulation of semiconductor lasers. Shown in the top table are the record 3-dB bandwidths for 1550 nm InP lasers. Matsui uses a conventional laser design [89] while Bach utilizes a more exotic 3-section laser structure that contains two resonance frequencies [90]. In other wavelength materials, most notably GaAs, the speed is typically faster than in InP. In the middle table, the fastest lasers were reported by Weisser [91] and Zhang [82], at 40 and 43 GHz respectively, as shown in the middle table.

Over the years, speed improvements have slowed as we approach the fundamental limits of laser modulation. The technique of optical injection locking allows us to exceed these fundamental limits. As previously stated, injection locking can increase the laser resonance frequency. Chrostowski et al., also at UC Berkeley, showed a 50 GHz enhanced resonance frequency, but at the expense of bandwidth [38]. We reiterate that it is difficult to balance the increased resonance and increased dip between DC and resonance, in order to optimize the 3-dB bandwidth. The record for bandwidth was held by Lee [40] at 28 GHz. Note that there is a large discrepancy between record bandwidth and resonance frequency, unlike free-running lasers. To date, there have been no comprehensive studies linking the resonance frequency and bandwidth of injection-locked lasers. In this chapter, we experimentally demonstrate many of the theoretical trends developed in the previous chapters. We use the insight gained from these calculations to demonstrate record-breaking results in both bandwidth and resonance frequency.

Record bandwidths, 1550nm

Author(s)	λ [nm]	f_{3dB}	Year	Laser	Affiliation
Morton, et al. [92]	1550	25 GHz	1992	strained MQW	Bell Labs
Goutain, et al. [93]	1550	30 GHz	1997	MQW-DFB, modulating saturable absorber	Thomson-CSF/LCR
Matsui, et al. [89]	1550	30 GHz	1997	strained MQW	FTRA/Oki Elec. Co.
Kjebon, et al. [94]	1550	31 GHz	1997	2- section DBR, detuned loading	KTH, Electrum
Bach, et al. [90]	1550	37 GHz	2003	coupled-cavity injection grating lasers (double resonance)	U. Wurzburg/TUD

Record bandwidths, other λ 's

Author(s)	λ [nm]	f_{3dB}	Year	Laser	Affiliation
Chen, et al. [95]	1300	20 GHz	1995	MQW DFB	Ortel Corp.
Weisser, et al. [91]	1100	40 GHz	1996	MQW F-P	Fraunhofer Inst.
Lear, et al. [96]	850	20 GHz	1997	VCSEL	Sandia
Zhang, et al. [82]	980	43 GHz	1997	tunnel-injection lasers	U. Mich., Ann Arbor

Record bandwidth & resonance frequency, injection-locked lasers

Author(s)	λ [nm]	Notes	Year	Laser	Affiliation
Chrostowski, et al. [38]	1550	$f_R = 50$ GHz	2005	VCSEL, intrinsic resonance only	UC Berkeley
Lee, et al. [40]	1550	$f_{3dB} = 28$ GHz	2000	DBR slave laser	MIT

Table 5.1 Survey of state-of-the-art records in high-speed laser modulation.

5.2 Laser Structure

The slave laser (SL) used for the experiments was a 1550 nm capped-mesa buried heterostructure (CMBH) DFB manufactured by Multiplex, Inc. [37]. The laser, shown in Figure 5.1, was a two-section DFB where each section was designed to lase independently. The DFB gratings ensured that if only one section was biased, the laser had a sufficiently-defined cavity to allow lasing. Since we performed reflection-style injection locking experiments, we only used one facet and, therefore, one of the bias sections. The length of the biased section was 500 μm , the width was 1 μm , and the laser had a threshold of 8 mA. The SL is biased at 29 mA ($3.5 \times I_{\text{th}}$) at 16°C; its optical power is $P_{SL} = +4$ dBm. The grating κL was designed to be approximately 3-4. The free-running slave at 29 mA bias had a frequency response as shown in Figure 5.2. It had a resonance frequency of about 6 GHz and a 3-dB bandwidth of 8 GHz.

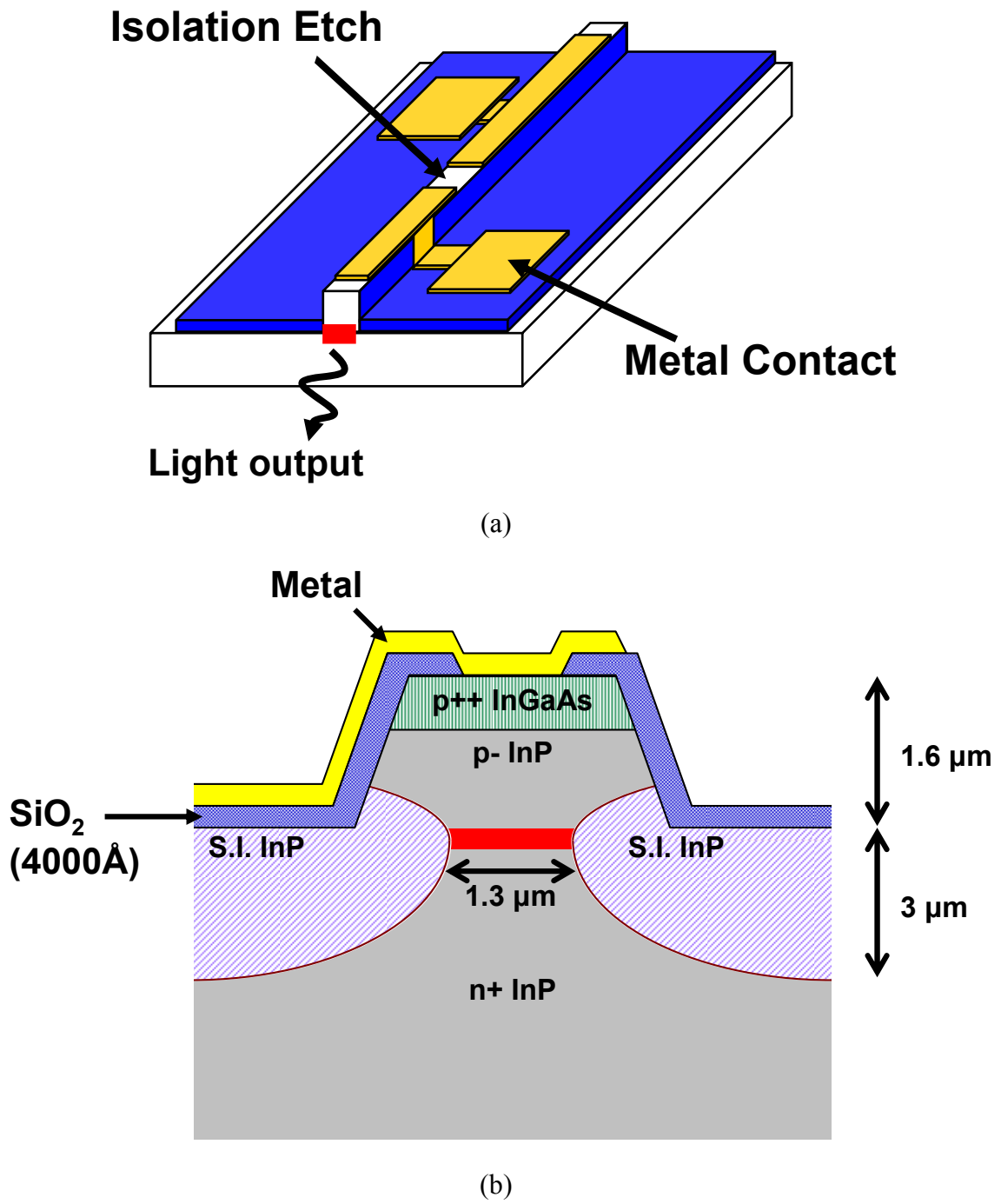


Figure 5.1 Laser structure of the 1550 nm CMBH DFB laser [37]. (a) Isometric view of the laser chip, showing top contacts, ridge waveguide, and output facet. (b) Blow-up of laser facet, showing epitaxial growth layers and CMBH structure.

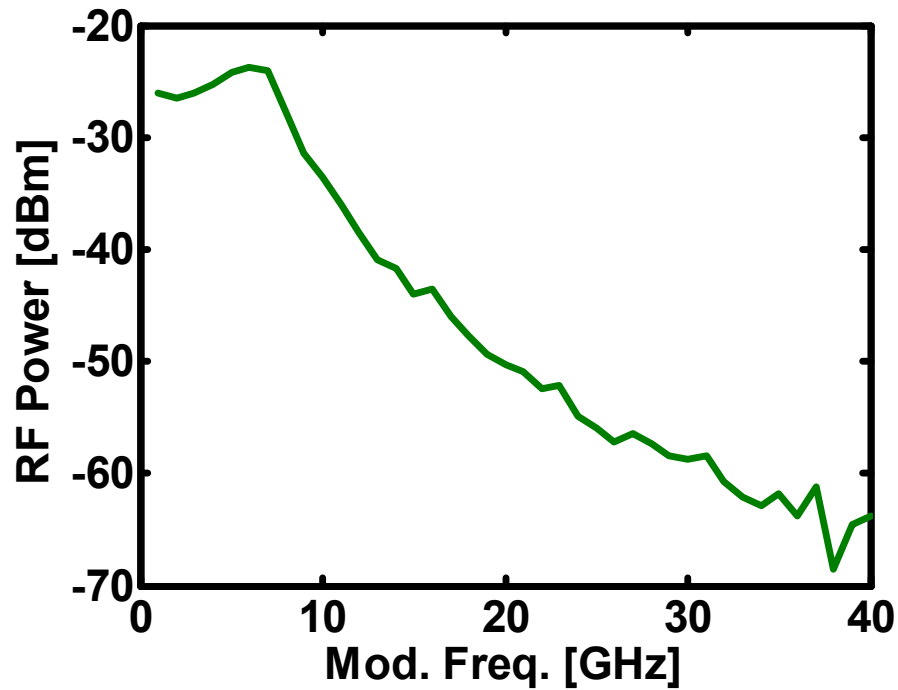


Figure 5.2 Frequency response of the free-running slave laser at 29 mA.

The gold contact pad on the laser chip was $60 \times 60 \mu\text{m}^2$, while the metallization from contact pad to waveguide was $20 \times 100 \mu\text{m}^2$. The SiO_2 oxide layer was 4000 \AA thick and the semi-insulating (S.I.) Fe-InP layer beneath it was $3 \mu\text{m}$ thick. To calculate the RC roll-off from the laser parasitics, we used relative permittivity values of $\epsilon_R = 3.7^2$ and 3.17^2 for the oxide and S.I. InP layers, respectively. The resistivity was assumed to be 50Ω . We can assume the forward-biased active region contributed little to the effective capacitance of the laser. Therefore, the primary capacitance occurs between the gold contact pad and lead. The capacitances of the oxide and S.I. InP are assumed to be in series. This results in an R-C roll-off frequency of 21 GHz.

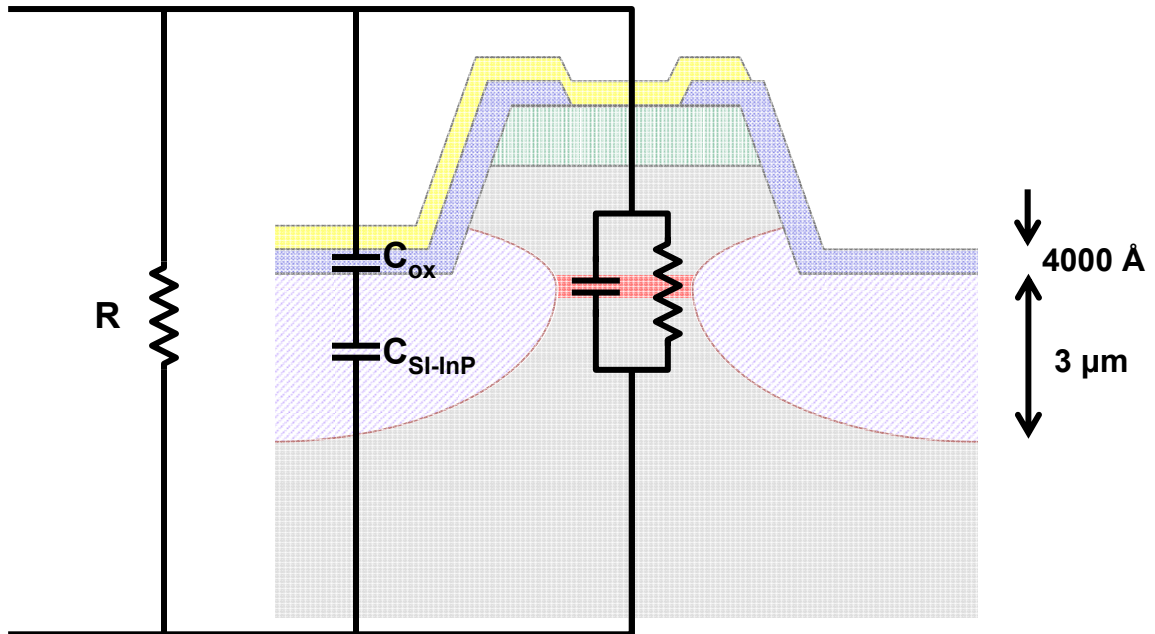


Figure 5.3 Small-signal circuit model of the laser, showing relevant components. The RC in the active region (shown, but unlabeled) was neglected.

5.3 Experimental Setup

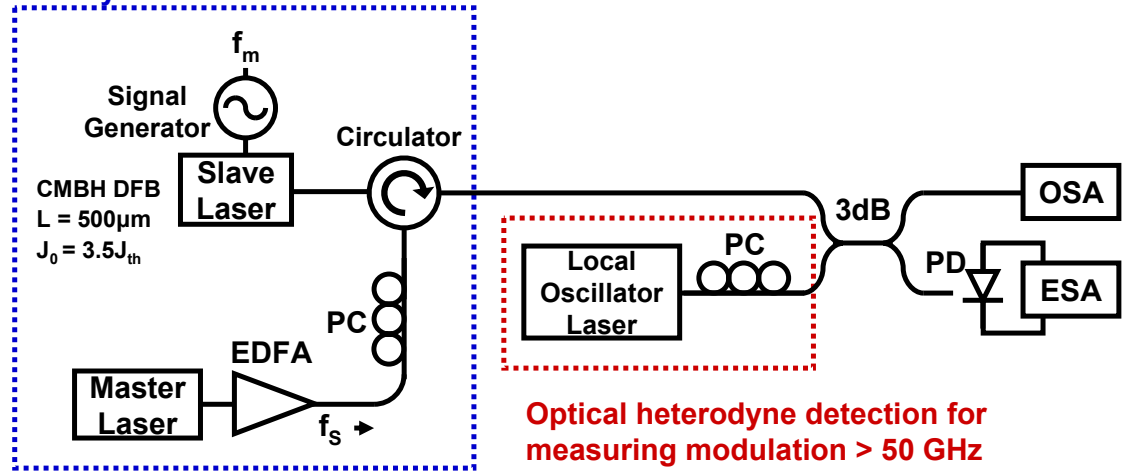
The experimental setup is shown in Figure 5.4. The injection-locked laser system is shown in the dotted dark blue box. The slave laser was heat sunk to a brass post using silver epoxy. The post was mounted in a large brass heat sink, which was thermally coupled to a thermo-electric cooler (TEC). The temperature was controlled at 289 K. Modulation was delivered to the slave laser via a 50-GHz signal generator (HP 83650B). Modulation from 50-75 GHz was supplied via a V-band frequency multiplier (HP 83557A). The output light of the slave laser was coupled to an optical fiber via a micro-positioned optical head (AR-coated objective lens). The same optical head was used to inject light into the output facet (reflection-style). An E-Tek circulator was used to ensure isolation between slave output and master input. The master laser (SDL 8610) had a typical output power of 2 dBm, and was amplified by an Erbium-doped fiber amplifier

(EDFA) made by Calmar Optcom, resulting in a master laser power up to $P_{ML} = +25$ dBm. The polarization is matched to the slave laser via a polarization controller (PC). The slave output is split via a 3-dB coupler and sent to an Ando AQ6317B optical spectrum analyzer (OSA) and an HP 83440D DC-34 GHz photodetector followed by an HP 8565E 50-GHz electrical spectrum analyzer (ESA). In order to measure frequencies above 50 GHz (the limit of our direct detection setup), we used a heterodyne detection scheme, described in Chapter 4. This is shown in the dotted dark red box. The LO was an Agilent 81680A tunable laser source biased at 3 dBm. When using direct detection, the local oscillator is simply turned off. The Bias-T was a 50-GHz Agilent model, the cables were typically K-cables, and the microwave probe was a K-connector signal/ground (SG) probe from GGB. All fibers were standard single-mode fiber.

The coupling loss from the optical head to the slave laser facet was measured to be 2.75 dB. Therefore the actual master laser power arriving at the facet of the slave laser was about 3-dB (including insertion losses from other components) lower than the output of the EDFA.

All measurement data was collected via computer. A key component in our experimental process was automation of the data collection by using GPIB-controlled test and measurement equipment and by iterative loop programs written in LabView. This allowed us to collect comprehensive data across a huge span of bias points. Typically, an injection level was set and then the master was tuned to a specific frequency. At each bias point, optical spectrum and electrical frequency response data were taken.

Strong optical injection-locked laser system via EDFA



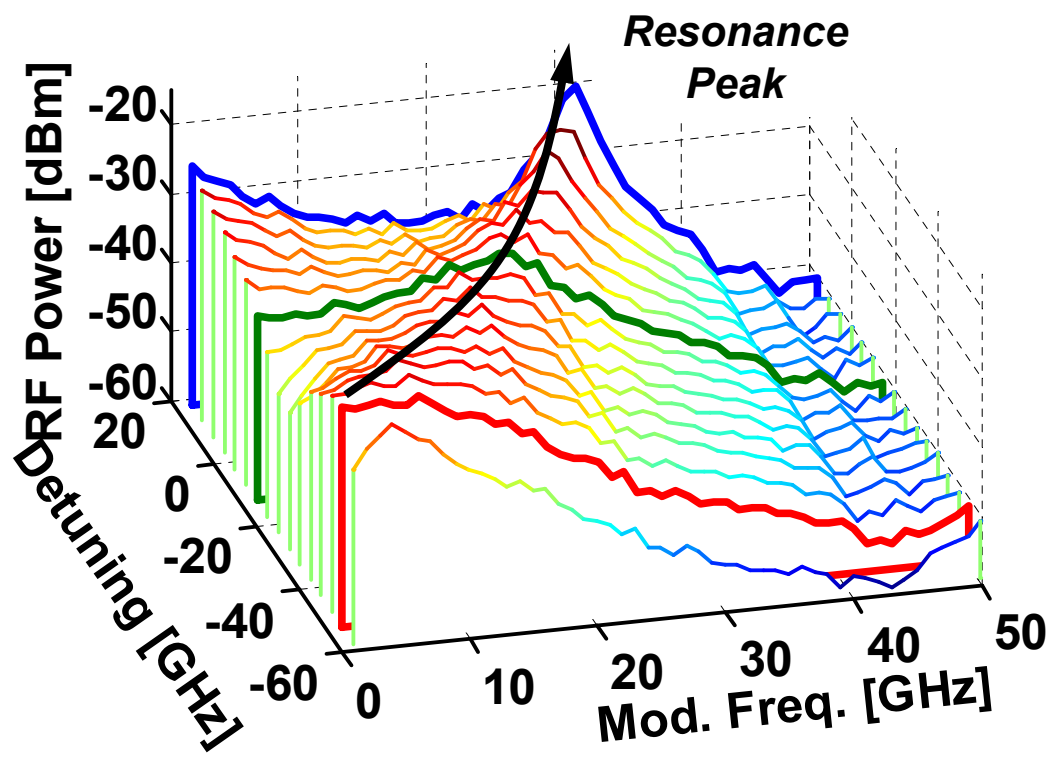
EDFA: Erbium-doped fiber amplifier
 PC: Polarization controller
 PD: Photodetector

3dB: 3dB-coupler
 OSA: Optical spectrum analyser
 ESA: Electrical spectrum analyser

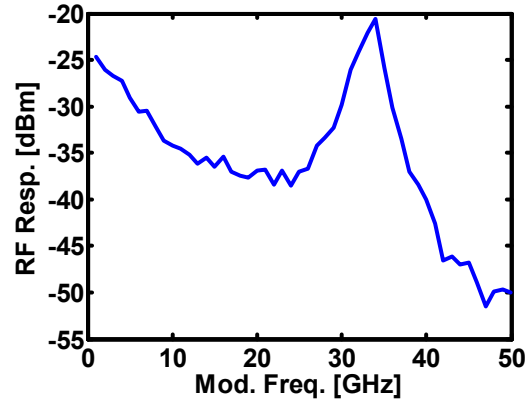
Figure 5.4 Experimental setup with optional heterodyne detection.

5.4 Resonance Frequency Evolution

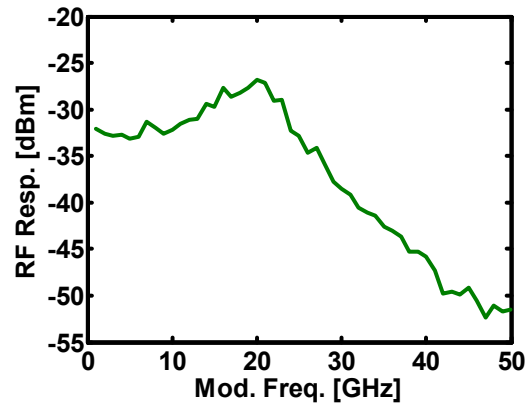
Figure 5.5 experimentally shows the resonance frequency dependence on detuning frequency, across the full stable locking range. The power of the master was set to $P_{ML} = 15$ dBm, hence the injection ratio was $R_{ext} = 8$ dB. The detuning frequency was varied from -59.8 to $+16.1$ GHz, the latter value resulting in a maximum resonance frequency of 34 GHz. We see excellent agreement with the waterfall plot shown in Figure 2.7(a). The trend for increasing the resonance frequency is apparent when increasing the frequency detuning. In Figure 5.5(b)-(d), we show selected frequency responses that represent the detuning frequencies that give the (b) highest resonance frequency, (c) largest 3-dB bandwidth (27.5 GHz), and (d) highest low-frequency gain, for this injection ratio.



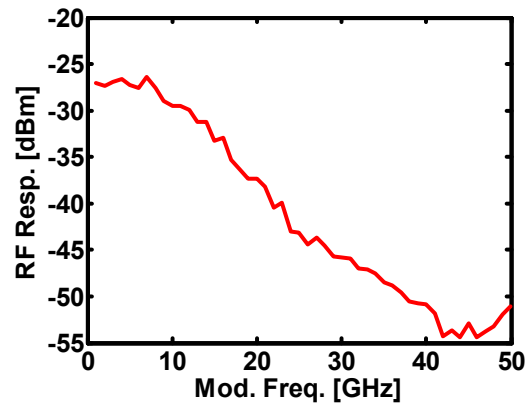
(a)



(b)



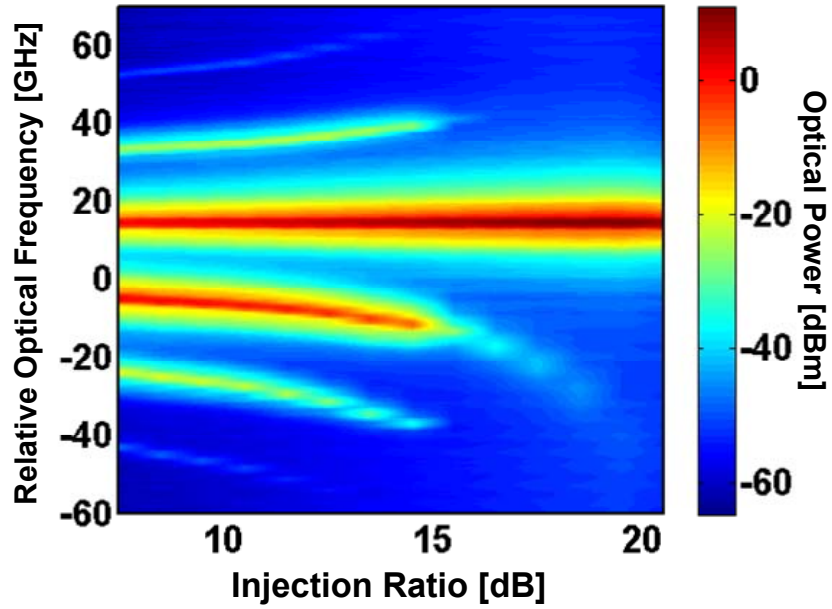
(c)



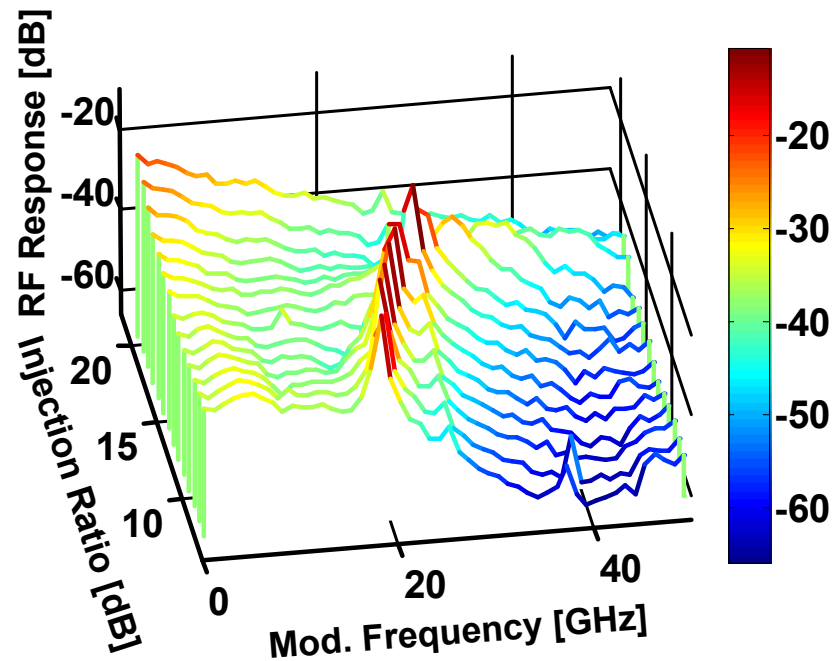
(d)

Figure 5.5 Experimental frequency response versus detuning, for $R_{ext} = 8$ dB. (a) Waterfall plot showing all frequency responses across the locking range, plus the resonance frequency evolution. Selected frequency response curves showing (b) maximum resonance frequency (c) largest broadband response (d) highest LF gain.

We can also look at frequency response evolution with respect to injection ratio. Figure 5.6(a) and (b) show the optical spectra evolution and frequency response slices, respectively. The detuning frequency is fixed at +15 GHz. The optical spectra are shown as optical frequency with respect to the free-running slave. There is no modulation applied when collecting the optical spectrum data. The locked mode (shown at +15 GHz for all injection ratios) grows in power by a few dB as the injection ratio increases. The slave cavity mode (shown as the falling horizontal line, starting at -5 GHz on the left hand side) pulls away from the locked mode as the injection ratio increases and finally vanishes with sufficient injection power. This corresponds to a shift in the cavity index due to a drop in the carrier number, as predicted in Section 2.7. The other prominent horizontal lines correspond to four-wave mixing terms, two above the locked mode and two below the cavity mode.



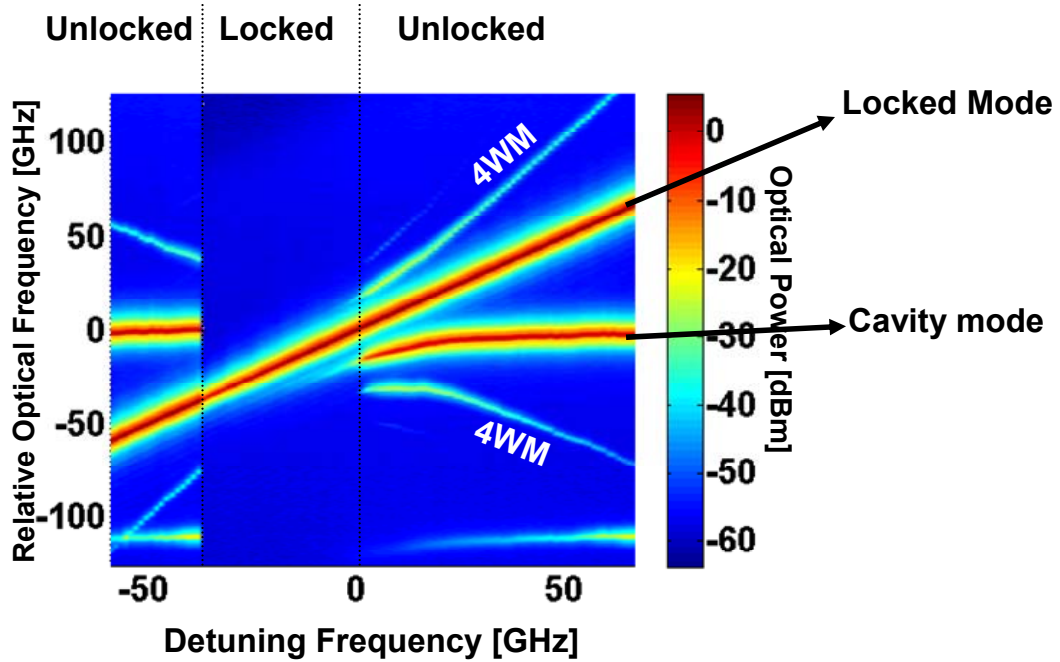
(a)



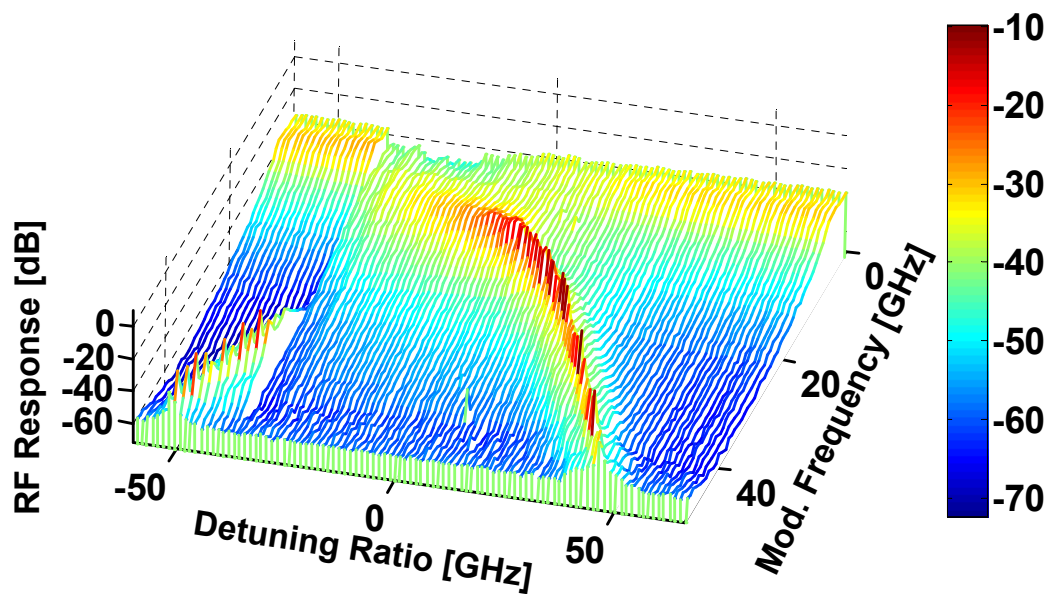
(b)

Figure 5.6 Frequency response vs. injection ratio, Δf_{inj} is fixed at +15 GHz. (a) Optical spectra with optical frequency relative to free-running frequency. Locked mode shown as highest power horizontal line (+15 GHz). Cavity mode is shown as 2nd highest horizontal line (starting at -5 GHz on l.h.s.). Four-wave mixing terms are shown above and below locked and cavity mode, respectively. (b) Waterfall plot of frequency responses. Resonance frequency is shown to increase with increasing injection ratio.

Similarly, we can show the optical spectrum and corresponding frequency response curves as we fix the injection ratio and sweep the detuning frequency (Figure 5.7). In Figure 5.7(a), the locking boundaries are marked with vertical dotted lines. The lower frequency edge is simple to distinguish, however the upper edge is continuous. Therefore, the locking edge is arbitrarily chosen to be at the point the cavity mode has a SMSR of 40 dB, ensuring single-mode performance at DC. Locked, cavity and four-wave mixing modes are labeled. As with the case of Figure 5.6, when the detuning frequency is increased, the cavity mode pulls away from the locked mode, resulting in an increased resonance frequency, shown in Figure 5.7(b). This clearly demonstrates the theory developed in Section 2.7.



(a)



(b)

Figure 5.7 Frequency response vs. detuning frequency. R_{ext} is fixed at +8 dB. (a) Optical spectra with optical frequency relative to free-running frequency. Locked, cavity, and four-wave mixing (4WM) modes are labeled. The locking boundary is marked at $\Delta f_{inj} = -37$ and 0 GHz. (b) Waterfall plot of frequency responses. Resonance frequency is shown to increase and damping is shown to decrease with increasing frequency response.

Finally, we can create a complete locking map by changing the injection ratio and sweeping the detuning frequency across the locking range (Figure 5.8). Again, we automate the process of collecting frequency response curves by using LabView. From the highest value of injection ratio (least quantization error), we can estimate the linewidth enhancement factor from (2.20), obtaining a value of $\alpha \approx 2.98$. This clearly shows the trend for increasing resonance frequency by increasing injection ratio and/or detuning frequency, and experimentally demonstrates the theoretical trends shown in Figure 2.3(b).

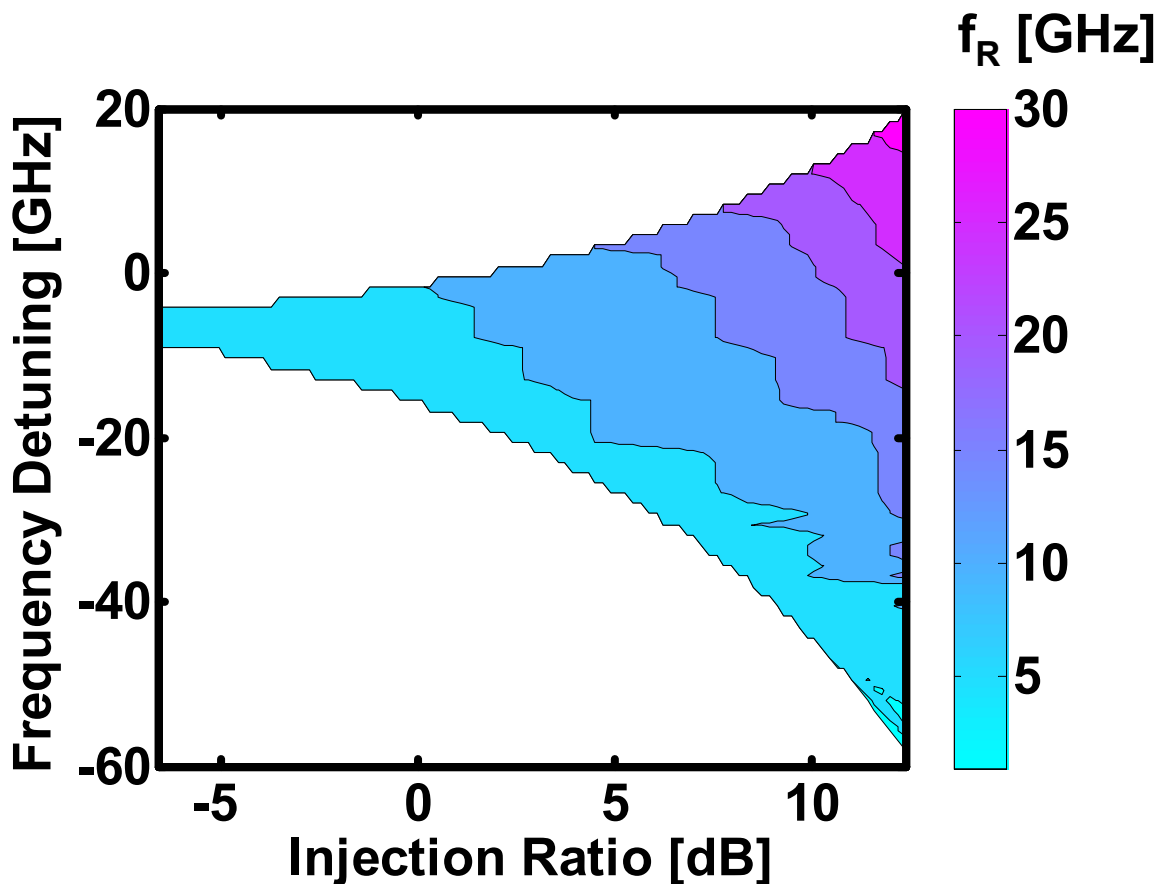


Figure 5.8 Experimental mapping of resonance frequency versus locking range.

5.5 Experimental Results

5.5.1 Optimized Resonance Frequency

Using the trends of the resonance frequency described in the theory and shown in the experiments above, we optimized the system for achieving the highest resonance frequency possible. The master laser power after EDFA amplification was 23 dBm, while the slave, biased at 3.5 times threshold, lased at 4 dBm, resulting in an injection ratio of +16 dB. The master was detuned to +64 GHz from the free-running slave. The LO is tuned to 50 GHz below the frequency of the master laser. Since our direct detection system measures up to 50 GHz, we measure the frequency response of the injection-locked laser up to 50 GHz. We then use the 50-75 GHz mm-wave source module to modulate the laser and use the heterodyne detection system to measure the frequency response. Since the separation between LO and locked mode was -50 GHz, the down-converted modulation frequency would be around 0-25 GHz, well within the bandwidth of both the PD and ESA. The LO was placed on the negative side to select the modulation sideband that was cavity-mode-enhanced. We ensured that the PD calibration for the down-converted data corresponded to the detected frequency, not the actual modulation frequency. The listed bias conditions resulted in an enhanced resonance frequency (f_R) of 72 GHz, as shown in Figure 5.9. To the best of our knowledge, this is the highest resonance frequency measured by electrical frequency response of any semiconductor laser. Also shown is a detuning condition (Δf_{inj}) of +53 GHz, resulting in a resonance frequency of 59 GHz. This demonstrates the simple tunability of the system. Photodetector and bias-T frequency-dependent loss was accounted for, but cable loss and modulation efficiency above 50 GHz were not calibrated. Microwave probe loss was not

calibrated out, as the signal and ground contacts were designed to have a height difference of 125 μm .

This resonance-enhanced modulation is different from biasing the system in the period-one oscillation regime, as described in [97], since the un-modulated optical beating is not detectable within the noise floor of the ESA (~ -65 dBm). Only when modulation is applied on or near the resonance frequency is there a detectable enhancement. Additionally, by tuning the master laser parameters, we can tune the magnitude and frequency of the resonance for greater peak response or variable frequency.

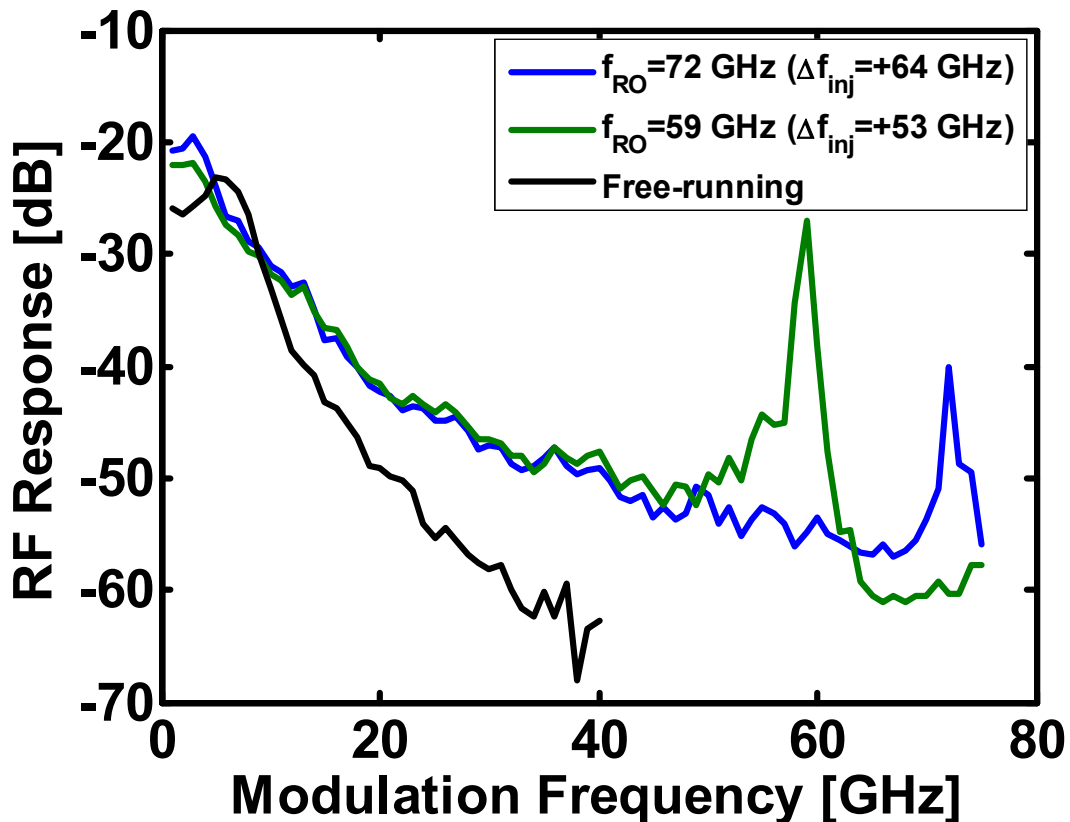


Figure 5.9 Experimental frequency response curve showing resonance frequencies of 59 GHz and 72 GHz. $R_{ext} = +16$ dB.

5.5.2 Optimized Broadband Performance

By optimizing for broadband performance, we obtain the results shown in Figure 5.10. For an 18-dB power ratio, we show a record 44 GHz broadband response. Optimization of bandwidth was achieved by two specific improvements: 1) systematic mapping of frequency response via automated data acquisition; 2) optical amplification of the master laser via EDFA into the extremely-strong injection regime (> 10 dB). Note that these results have only been calibrated for photodetector, cable loss, and source power. Again, the microwave probe response was not calibrated. Having this knowledge would improve our results. To our best knowledge, this is the broadest frequency response of any semiconductor laser at any wavelength.

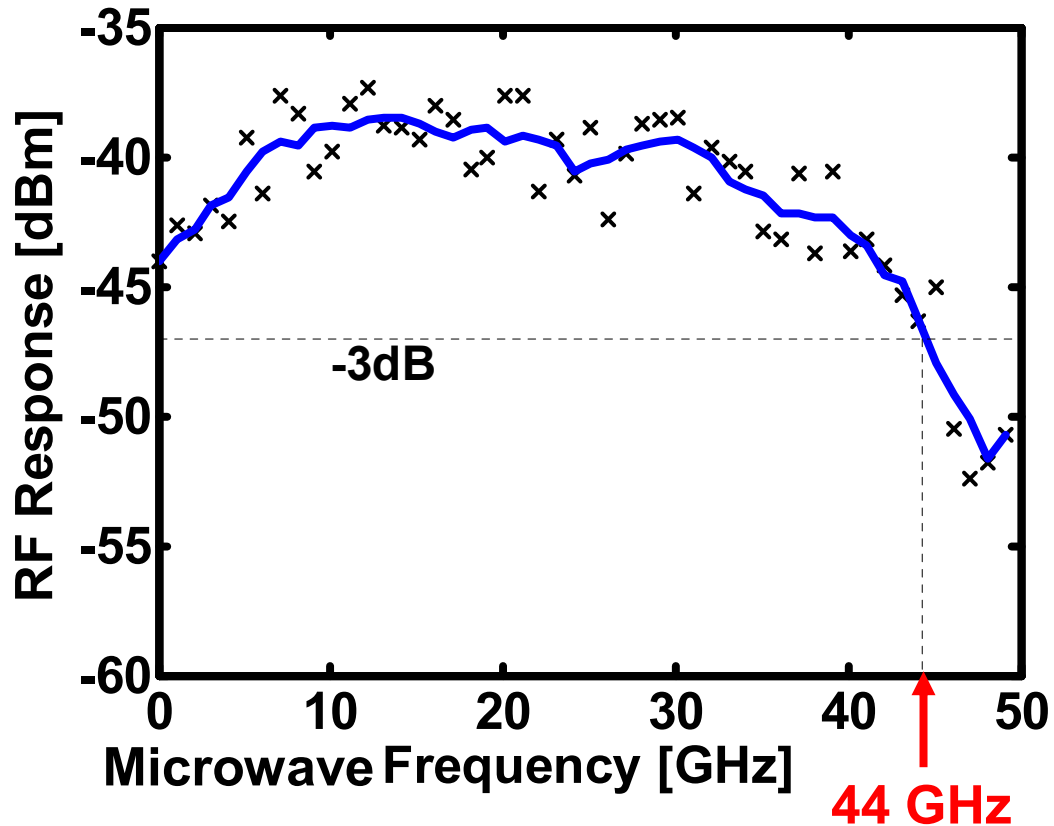


Figure 5.10 Experimental frequency response curve showing a broadband, 3-dB response of 44 GHz. $R_{ext} = +18$ dB, $\Delta f_{inj} = -60.5$ GHz.

5.6 Discussion

5.6.1 Facets of Two-Section DFB Lasers

The internal “facet”, defined by the end of the bias section and adjacent to the isolation etch region in Figure 5.1(a), was not ideal. In essence, it can be modeled as an AR-coated facet, since the light entering into the isolation etch region and beyond will experience extreme loss, due to these sections being unbiased, and not be reflected back in to the relevant lasing section. The loss at this facet did not increase the coupling of injected light, as a similar reduction in mirror reflectivity would have done for the output facet, and most likely increased the threshold carrier number and current. According to

the conclusions from Chapter 4, this is exactly the opposite condition from the optimal case. The laser used was not designed with these high-speed applications in mind. Although our results are extremely fast, we foresee increased performance as we begin to implement the design rules developed in this dissertation and design optimal devices for reaching even higher resonance frequencies and bandwidths.

5.6.2 > 100 GHz Resonance Frequencies

The record resonance frequency of 72 GHz was chosen because our microwave generation capabilities were limited to < 75 GHz. To prove the capability of obtaining higher resonance frequencies, we look to the optical spectrum. Figure 5.11 shows the optical spectrum of a bias point at which the cavity mode is 100 GHz away from the locked mode. From the theory developed in Section 2.6.1, we expect to be able to measure a frequency response with a 100-GHz resonance. The limit to the resonance frequency enhancement is governed only by the amount of power one can inject via the master laser. We plan to be able to measure resonance frequencies over 100 GHz, and explore the practical limits of this phenomenon.

5.6.3 Future Plans

Since we used the heterodyne detection technique, our ability to measure resonance frequencies higher than 75 GHz was limited only by a lack of a W-band source. Our future plans involve upgrading the maximum electrical speed of our system to observe > 50 GHz broadband response and > 100 GHz resonance frequencies. This includes obtaining higher frequency sources and detectors. Since the maximum resonance frequency is proportional to the square root of the injection ratio, we can also benefit

from increasing the master laser power. This would require higher power sources or higher saturation power EDFAs. We also plan to extend our work to injection locking of VCSELs through collaboration with our colleagues at UC Berkeley.

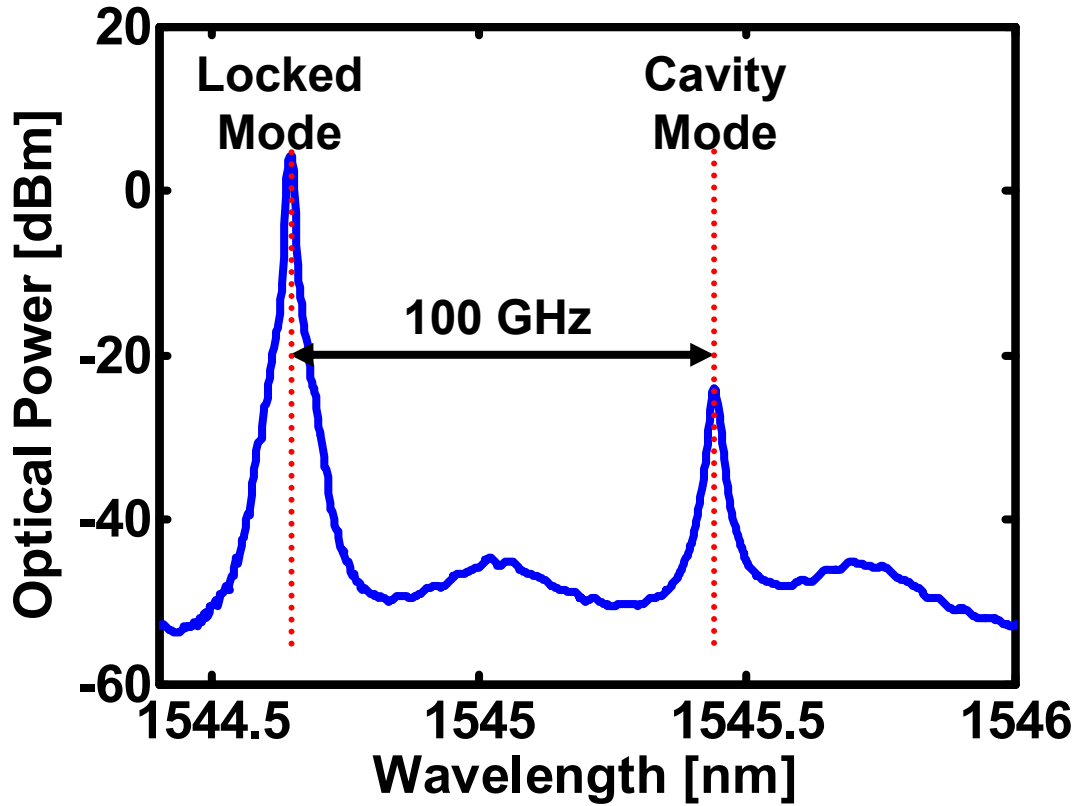


Figure 5.11 Optical spectrum of an injection-locked laser biased such that the cavity mode is 100 GHz away from the locked mode. This shows potential for >100 GHz resonance frequency lasers. $P_{ML} = 16$ dBm, $P_{SL} = 1.4$ dBm, $\Delta f_{inj} = +94$ GHz.

Chapter 6

Modulation of the Master Laser

6.1 Motivation

Most of the previous studies on optical injection locking have focused on the modulation of the slave laser, or direct modulation. Modulation of master lasers has many potential applications in FM spectroscopy and FM discrimination. Intuitively, the slave laser frequency would follow that of the master laser, while its intensity is weakly dependent on the master laser power. Potentially, this can be used to produce frequency modulation (FM) and/or suppress residual amplitude modulation (RAM). Alternatively, it can be used to lock the local oscillator in coherent analog optical links.

In this chapter, we present a systematic study, both experimentally and theoretically, of the effects of master laser modulation on the slave laser. We find that FM can be preserved, up to the resonance peak, and even for relatively weak injection ratios. Additionally, AM is suppressed, inverse-proportionally to the injection ratio. We also discovered that pure master FM converts not only to slave FM, but also significantly creates slave AM. This novel conversion technique has a wide range of potential

applications such as an FM discriminator for detection of PSK or FSK modulation schemes. The bandwidth of all these effects is extended by the resonance frequency enhancement in the strong-injection regime. In the same way as relative intensity noise (RIN), the resonance frequency and damping are correlated to the direct modulation response. Hence, the trends developed in the previous chapters directly relate to the modulation schemes listed in this one.

6.2 Experiment

In injection-locked laser systems, a master laser injects light into a slave laser, thus modifying the slave's characteristics. Typically, we modulate the system by applying a modulating current (direct modulation, or DM) on the slave, shown in Figure 6.1(a). Alternatively, as shown in Figure 6.1(b), we can modulate the injected light from the master laser, either AM or FM.

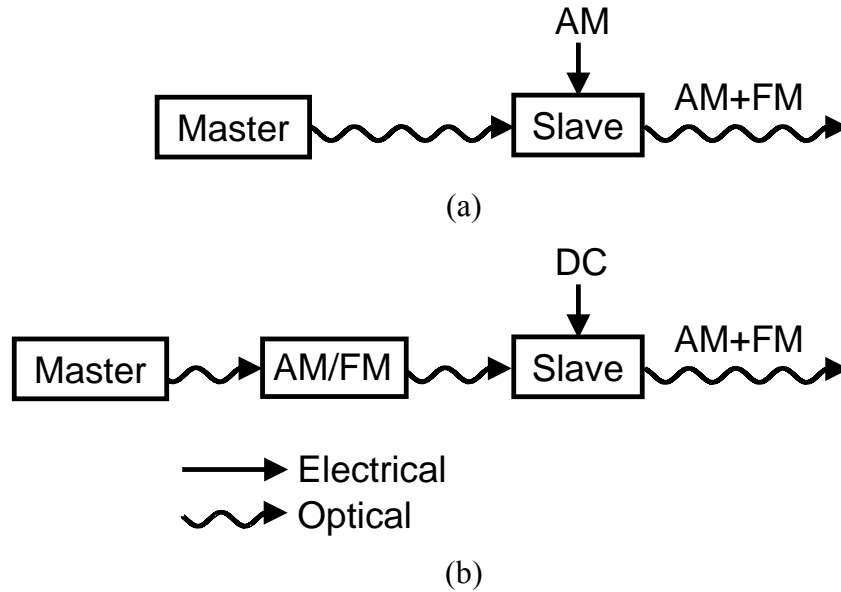
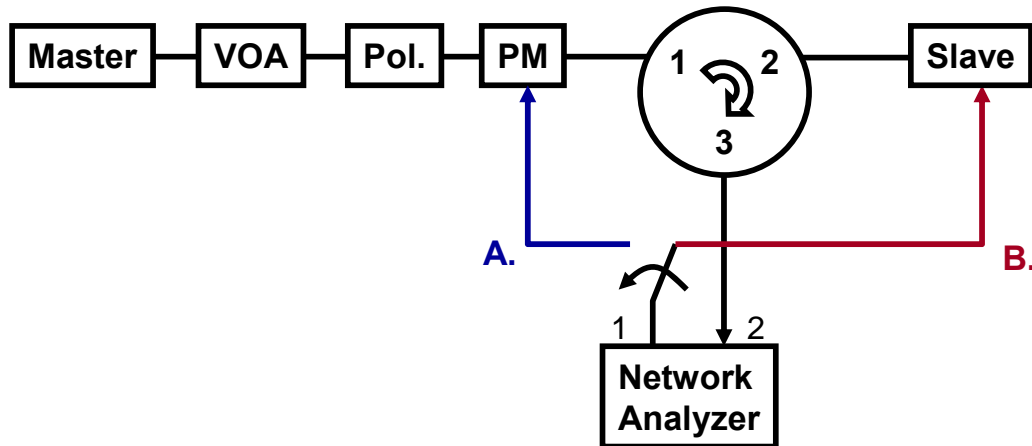


Figure 6.1 (a) Schematic of typical injection locking system with direct modulation on the slave current, resulting in AM+FM output. (b) Schematic of injection locking system with master laser modulation. If external modulation is applied, AM or FM (PM) can be applied separately. Choosing either modulation will result in both AM and FM on the slave output.



- A. Frequency Modulation on Master**
- B. Current Modulation on Slave**

Figure 6.2 Schematic of experimental setup for measuring FM-to-AM conversion and direct modulation. One of two modes can be switched from the output of the network analyzer: A. will create frequency modulation on the master while B. will directly modulate the slave. VOA = variable optical attenuator, Pol. = polarization controller, PM = phase modulator.

RAM suppression (AM to AM) and FM efficiency (FM to FM) have already been demonstrated in FM spectroscopy systems [28]. In this section, we experimentally demonstrate FM-to-AM conversion (FM to AM). We define FM-to-AM conversion as the conversion of injected FM into slave AM. The experimental setup is shown in Figure 6.2. The master laser is a frequency-tunable diode laser and the slave laser is a 1550 nm distributed feedback (DFB) laser. The master was typically tuned to 0 GHz detuning frequency. We follow the master laser with a variable attenuator (VOA), polarization controller (Pol.) and phase modulator (PM). The master light is injected into the slave via a circulator. The slave output is taken from the same side as injection. We obtain frequency response data via a network analyzer. We modulate the system at two different points: A. we modulate the master laser using a LiNbO₃ PM, which produces FM injection light without AM; B. we directly modulate the slave laser. The same RF power is used on both modulation points. Figure 6.3 shows the experimental results. The network analyzer's photodetector only senses slave AM and therefore the slave FM is decorrelated from these results. *AM on Slave (unlocked)* shows the direct modulation frequency response of the laser without injection. *AM on Slave (locked)* shows the characteristic enhanced resonance frequency due to injection locking. *FM on master (unlocked)* shows the effect of the master FM on the slave AM in the unlocked state (not injection-locked). Since the FM is not correlated to the AM in this case, the frequency response is essentially the noise floor of the network analyzer system. *FM on Master (locked)* shows FM-to-AM conversion for the injection-locked system. The FM-to-AM conversion is proportional to the modulation frequency, and therefore there is less crosstalk for lower modulation frequencies and more for higher frequencies. Below

resonance, the AM due to FM-to-AM conversion is much smaller than the AM due to direct modulation. At resonance, the FM-to-AM conversion magnitude is about 10 dB below the direct modulation, and is a significant effect. Above resonance, the crosstalk effect is almost equal to the direct modulation.

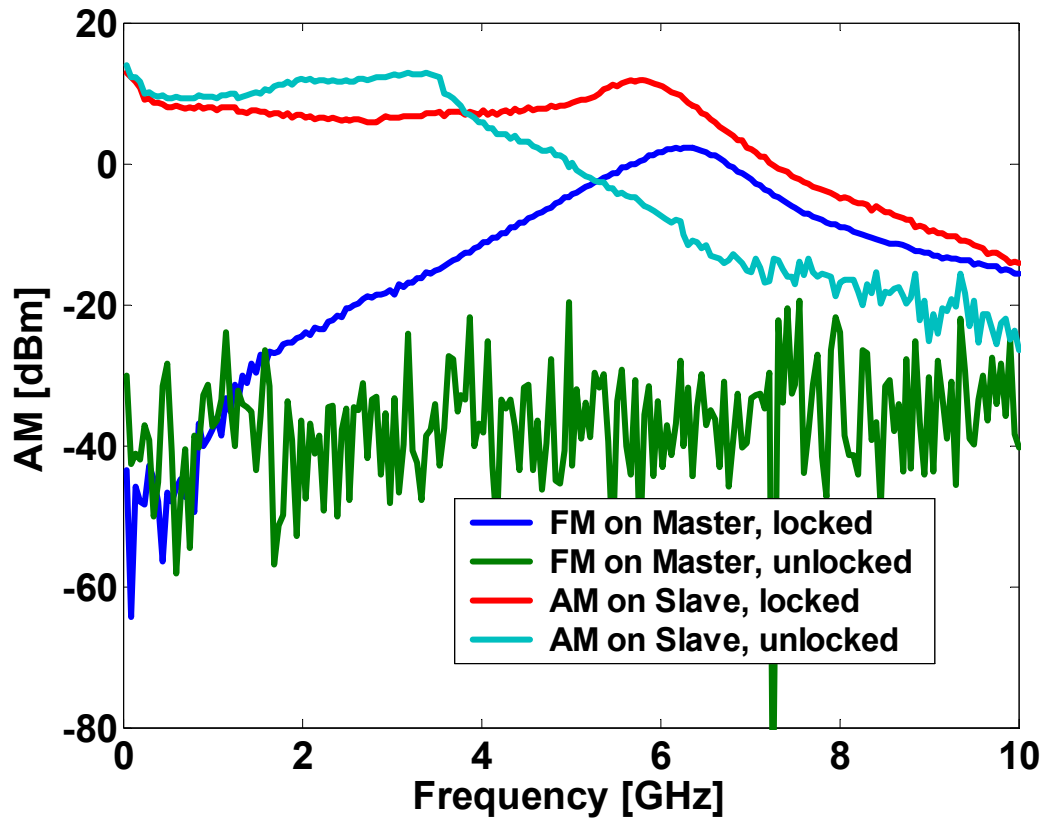


Figure 6.3 Slave AM due to different modulation sources. FM-to-AM conversion and direct modulation are shown.

Figure 6.4 shows the FM-to-AM conversion for various injection ratios. We can compare this to our theoretical results, found in Figure 6.8. The general response line features match up quite well, although the injection ratios are different, due to the fact that the real laser is a DFB rather than a Fabry-Perot, which is used in the theory. As is

the case with direct modulation, the resonance frequency for FM-to-AM conversion is enhanced for larger injection ratios.

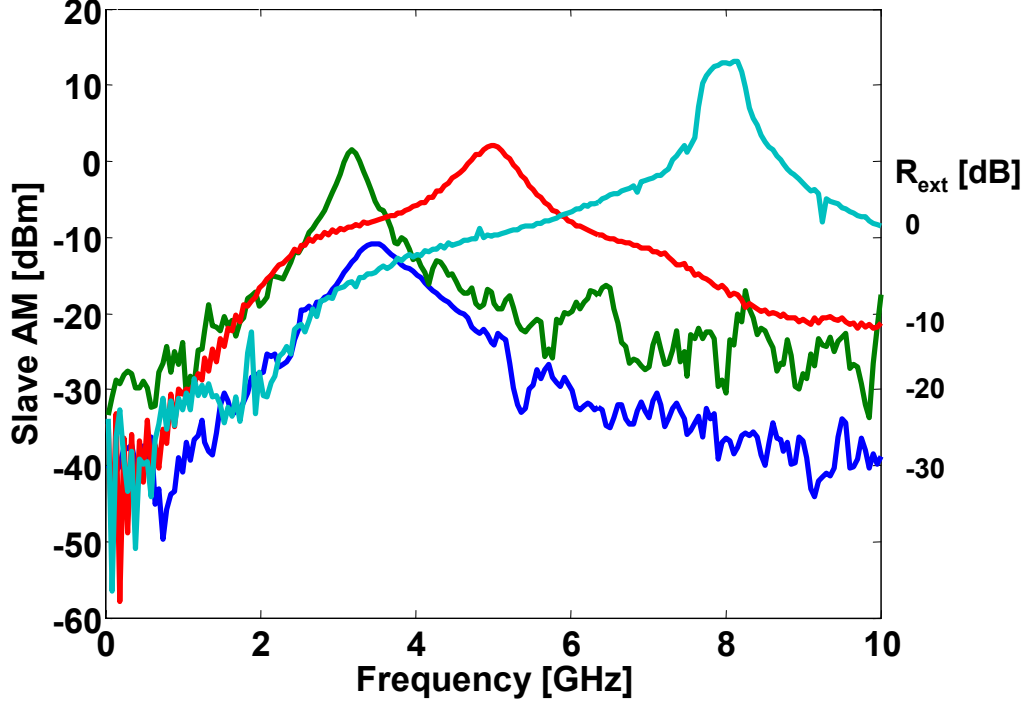


Figure 6.4 Experimental FM-to-AM conversion for different injection ratios.

6.3 Theory

In order to analyze the effects of master laser modulation, we perform a small-signal linearization of the laser rate equations with injection [98]:

$$\frac{\partial E(t)}{\partial t} = -\frac{1}{2\tau_p} E(t) + i(\omega_0 - \omega_c) E(t) + \frac{\Gamma}{2} g(t)(1 - i\alpha) E(t) + \kappa E_i(t) + F_{sp} \quad (6.1)$$

$$\frac{\partial N(t)}{\partial t} = \frac{\eta_i}{qV} I(t) - \frac{N(t)}{\tau_c(t)} - \gamma g(t) |E(t)|^2 \quad (6.2)$$

where $E(t)$ is the slave's complex field, τ_p is its photon lifetime, ω_0 is the free-running frequency, ω_c is the cold-cavity frequency, Γ is the confinement factor, $g(t)$ is the non-linear gain, α is the linewidth enhancement parameter, κ is the coupling rate coefficient,

F_{sp} is the spontaneous emission term, $N(t)$ is the slave's carrier density, η_i is the current injection efficiency, q is the electric charge per electron, V is the volume of the active region, $I(t)$ is the current, and $\tau_c(t)$ is the carrier-dependent carrier lifetime. Here, we use equations that contain more higher-order effects than (2.3)-(2.5), namely the logarithmic gain model with gain compression, carrier-dependent carrier lifetime, and current leakage, η_i . The non-linear gain model, carrier lifetime and γ are defined as:

$$g(t) = g_0 \ln \left(\frac{N(t) + N_s}{N_{tr} + N_s} \right) \left(1 - \varepsilon \gamma |E(t)|^2 \right) \quad (6.3)$$

$$\frac{1}{\tau_c(t)} = A + BN(t) + CN^2(t) \quad (6.4)$$

$$\gamma \equiv \frac{2\varepsilon_0 n^2}{h\nu} \quad (6.5)$$

where N_{tr} is the transparency carrier density, N_s is a logarithmic gain fitting parameter, ε is the gain compression term, ε_0 is the permittivity of free-space, n is the effective index of the slave mode, and $h\nu$ is the photon energy. A , B , and C are the defect, spontaneous, and Auger recombination coefficients, respectively.

Typically, we would add DC plus perturbation terms to the time-dependent functions, then linearize the equations such that they fit into the matrix format shown in (2.13). However, the analysis in [98] contains only one driving term: current modulation on the slave, which we define here:

$$I(t) = I_0 + I_{RF} \sin(\omega_M t + \delta_{DM}) \quad (6.6)$$

where I_0 is the bias current, I_{RF} is the small-signal current strength, ω_M is the modulation frequency, and δ_{DM} is the direct modulation (DM) phase. To include the master

modulation terms, we modify the injection term, E_i (typically taken as a constant) to include AM and FM driving terms:

$$E_i(t) = A_i(t)e^{-\Omega t - i\theta(t)} \quad (6.7)$$

where $A_i(t)$, Ω , and $\theta(t)$, are the amplitude modulation (AM), detuning frequency, and phase modulation (PM) (which translates to FM through a time derivative) of the master laser field, respectively:

$$A_i(t) = A_i(1 + M \sin(\omega_M t + \delta_{AM})) \quad (6.8)$$

$$\theta(t) = \beta \sin(\omega_M t + \delta_{PM}) \quad (6.9)$$

where A_i is the DC injection magnitude, M is the master laser amplitude modulation index, δ_{AM} is the AM phase, β is the master laser phase modulation index, and δ_{PM} is the PM phase offset. We then neglect the spontaneous emission and separate the slave amplitude and phase into two separate rate equations:

$$\frac{\partial A(t)}{\partial t} = \frac{\Gamma}{2} g(t)A(t) - \frac{1}{2\tau_p} A(t) + \kappa A_i(1 + M \sin(\omega_M t + \delta_{AM})) \cos[\Omega t + \beta \sin(\omega_M t + \delta_{PM}) - \Phi(t)] \quad (6.10)$$

$$\frac{\partial \Phi(t)}{\partial t} = -(\omega_0 - \omega_c) + \frac{\Gamma}{2} \alpha g(t) + \kappa \frac{A_i}{A(t)}(1 + M \sin(\omega_M t + \delta_{AM})) \sin[\Omega t + \beta \sin(\omega_M t + \delta_{PM}) - \Phi(t)] \quad (6.11)$$

$$\frac{\partial N(t)}{\partial t} = \frac{\eta_i}{qV} (I_0 + I_{RF} \sin(\omega_M t + \delta_{DM})) - \frac{N(t)}{\tau_c(t)} - \gamma g(t) |A(t)|^2 \quad (6.12)$$

The steady-state solutions are found similarly to those in Chapter 2, where we define A_0 , Φ_0 , and N_0 as the steady-state values. To achieve a steady-state phase without injection, the frequency difference, $\omega_0 - \omega_c$, is equal to:

$$\omega_0 - \omega_c = \frac{\Gamma}{2} \alpha G_0 \quad (6.13)$$

where G_0 is the steady-state gain:

$$G_0 = v_G g_0 \ln \left(\frac{N_0 + N_s}{N_{tr} + N_s} \right) (1 - \varepsilon \gamma |A_0|^2). \quad (6.14)$$

We then perform small-signal linearization upon (6.10)-(6.12). Our solution is similar to that found in [98], however it contains two additional driving terms: the master AM and the master PM. The final form of the matrix equations are:

$$\begin{bmatrix} m_{11} - s & m_{12} & m_{13} \\ m_{21} & m_{22} - s & m_{23} \\ m_{31} & m_{32} & m_{33} - s \end{bmatrix} \begin{bmatrix} \Delta A \\ \Delta \Phi \\ \Delta N \end{bmatrix} = \begin{bmatrix} -\kappa \cos \phi_0 \\ \kappa \frac{1}{A_0} \sin \phi_0 \\ 0 \end{bmatrix} \Delta A_i e^{j\delta_{AM}} + \begin{bmatrix} -\kappa A_i \sin \phi_0 \\ -\kappa \frac{A_i}{A_0} \cos \phi_0 \\ 0 \end{bmatrix} \Delta \theta e^{j\delta_{PM}} + \begin{bmatrix} 0 \\ 0 \\ -\frac{\eta_i}{eV} \end{bmatrix} \Delta I e^{j\delta_{DM}} \quad (6.15)$$

where the general complex s can be replaced with $j\omega_M$. Here, there are three separate driving terms: ΔA_i , $\Delta \theta$, and ΔI . where $\Delta A_i = A_i M$ and $\Delta \theta = \beta$. The matrix elements are similar to those in Chapter 2, except for the higher-order terms:

$$\begin{aligned} m_{11} &= \frac{1}{2} \left(\Gamma G_0 - \frac{1}{\tau_p} \right) - \Gamma G_S (\varepsilon S_0) \\ m_{12} &= -\kappa A_i \sin \phi_0 \\ m_{13} &= \frac{1}{2} \Gamma G_N A_0 \\ m_{21} &= -\Gamma \alpha G_S (\varepsilon \gamma A_0^2) + \kappa \frac{A_i}{A_0^2} \sin \phi_0 \\ m_{22} &= -\kappa \frac{A_i}{A_0} \cos \phi_0 \\ m_{23} &= \frac{1}{2} \Gamma \alpha G_N \\ m_{31} &= -2G_0 \gamma A_0 + G_S (2\varepsilon \gamma A_0) \gamma A_0^2 \\ m_{32} &= 0 \\ m_{33} &= -A - 2BN_0 - 3CN_0^2 - G_N S_0 \end{aligned} \quad (6.16)$$

where

$$\begin{aligned}
 G_N &= v_G g_0 \frac{1 - \varepsilon S_0}{N_0 - N_S} \\
 G_S &= v_G g_0 \ln \left(\frac{N_0 + N_S}{N_{tr} + N_S} \right) \\
 S_0 &= \gamma A_0^2.
 \end{aligned} \tag{6.17}$$

The third driving term in (6.15), ΔI , should be recognized as the direct modulation term, and can be commonly found in literature [98, 99]. The first and second driving terms are AM (ΔA_i) and PM ($\Delta \theta$) that has been implied upon the injected master light. By choosing one of the three terms and setting the other two to zero, we can calculate that driving term's effect on the modulation of the slave field amplitude (ΔA), phase ($\Delta \Phi$), and carrier density (ΔN). We define four of the more interesting terms in the next section.

6.4 Analysis

If we choose one output term and one driving term, we can take their ratio, and from (6.15), determine its frequency response. There are 3 output and 3 driving terms, giving us 9 different ratios. The typical ratios found in literature are $\Delta A/\Delta I$ (DM to AM), or commonly called modulation response, and $\Delta \Phi/\Delta I$ (DM to FM), which can be used to determine the direct modulation frequency response and frequency chirp. The parameters used in this chapter are listed in Table 6.1.

Symbol	Name	Value	Units
λ	wavelength	1550	nm
Γ	confinement factor	0.06	-
ε	gain compression factor	1.5×10^{-17}	cm^3
n_G	group index	3.7	-
n_{Eff}	effective index	3.3	-
η_i	current injection efficiency	1	-
g_0	logarithmic gain coefficient	1500	1/s
N_{tr}	carrier transparency density	1.5×10^{18}	cm^{-3}
N_s	gain curve fitting parameter	0.6×10^{18}	cm^{-3}
L	length	500	μm
w	width	2.5	μm
t_{QW}	quantum well thickness	80	\AA
N_{QW}	quantum well number	8	#
α	linewidth enhancement parameter	4	-
I_0	bias current	30	mA
α_i	intrinsic material loss	18	cm^{-1}
A	defect recombination	0	1/s
B	spontaneous recombination	1×10^{-10}	cm^3/s
C	Auger recombination	80×10^{-30}	cm^6/s
r	mirror reflectivity	0.286	-

Table 6.1 Laser parameters used in this chapter.

6.4.1 Direct Modulation

Figure 6.5 shows the frequency response from direct modulation ($\Delta A/\Delta I$) for a typical edge-emitting laser, whose parameters we will use throughout this paper. The family of curves corresponds to varying injection ratios (R_{int}). As observed in the literature [33, 99], the resonance peak is enhanced for higher injection ratios.

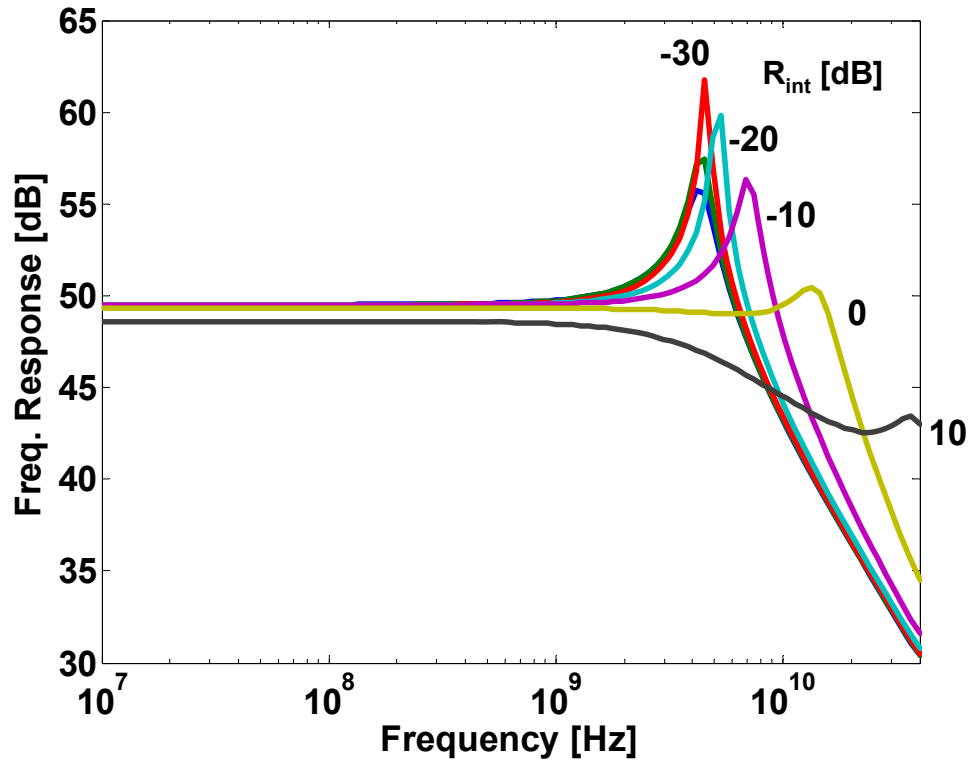


Figure 6.5 Direct modulation for various injection ratios: (a) schematic (b) frequency response. Driving source: current modulation on slave. Measured output: optical AM on slave.

6.4.2 RAM Suppression

If we explore the ratio, $\Delta A_i/\Delta A$ (AM to AM), we can observe how the master AM affects the slave AM. This ratio is proportional to residual amplitude modulation (RAM) suppression, which is defined as the degree of suppression of optical AM as it is transferred from master to slave. If we are interested in only the FM component of a signal that contains both AM and FM, RAM suppression may be useful in removing the

unwanted AM. For example, this technique has been used in FM spectroscopy [28]. Figure 6.6 shows the frequency response of RAM suppression for our sample laser. For smaller injection ratios, the suppression is greater, attesting to the fact that the master only injects small amounts of light into the slave's photon reservoir. At a nominal injection ratio of -50 dB, a RAM suppression of >130 dB can be achieved. At resonance, the suppression actually goes negative for higher injection ratios, which corresponds to an AM enhancement.

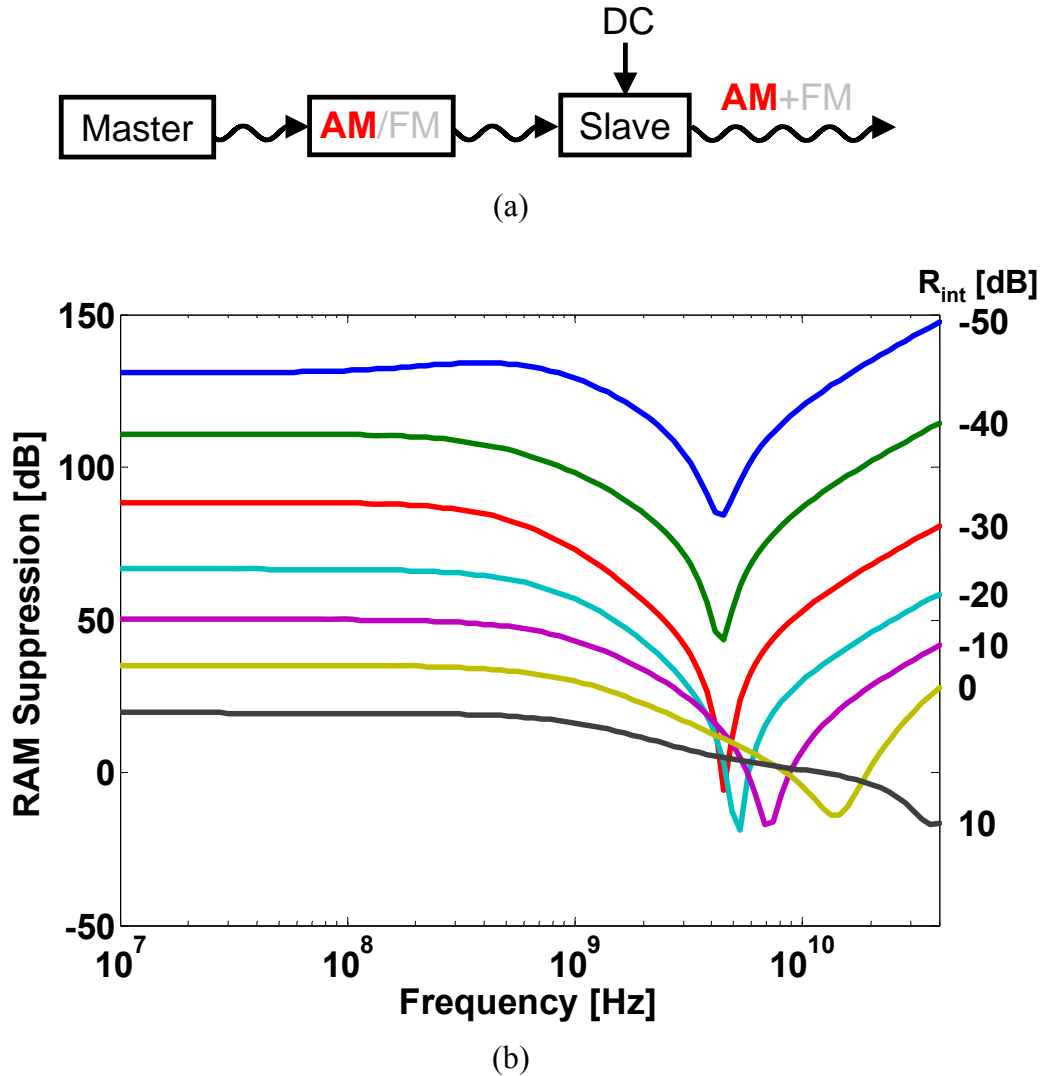


Figure 6.6 RAM suppression for various injection ratios: (a) schematic (b) frequency response. Driving source: optical AM on master. Measured output: optical AM on slave.

6.4.3 FM-to-AM Conversion

We can also determine the effect of master FM on both the AM and FM of the slave, through the ratios $\Delta A_i / \Delta \theta$ (FM to AM) and $\Delta \Phi / \Delta \theta$ (FM to FM), respectively. The first is proportional to FM-to-AM conversion; it shows a coupling between the master FM and the slave AM. This can be used as a FM discriminator or, in other applications, it may lead to unwanted AM, as in FM spectroscopy [28]. Figure 6.7 shows the frequency

response of the slave amplitude per Hertz of master frequency excursion. Figure 6.8 shows the frequency response of the slave amplitude per radian of phase modulation excursion, and is related to Figure 6.7 by the modulation frequency. This corresponds to a 0.88 mW/GHz frequency-to-amplitude modulation conversion efficiency. Our theory (Figure 6.4) predicts our experimental evidence of FM-to-AM conversion quite well.

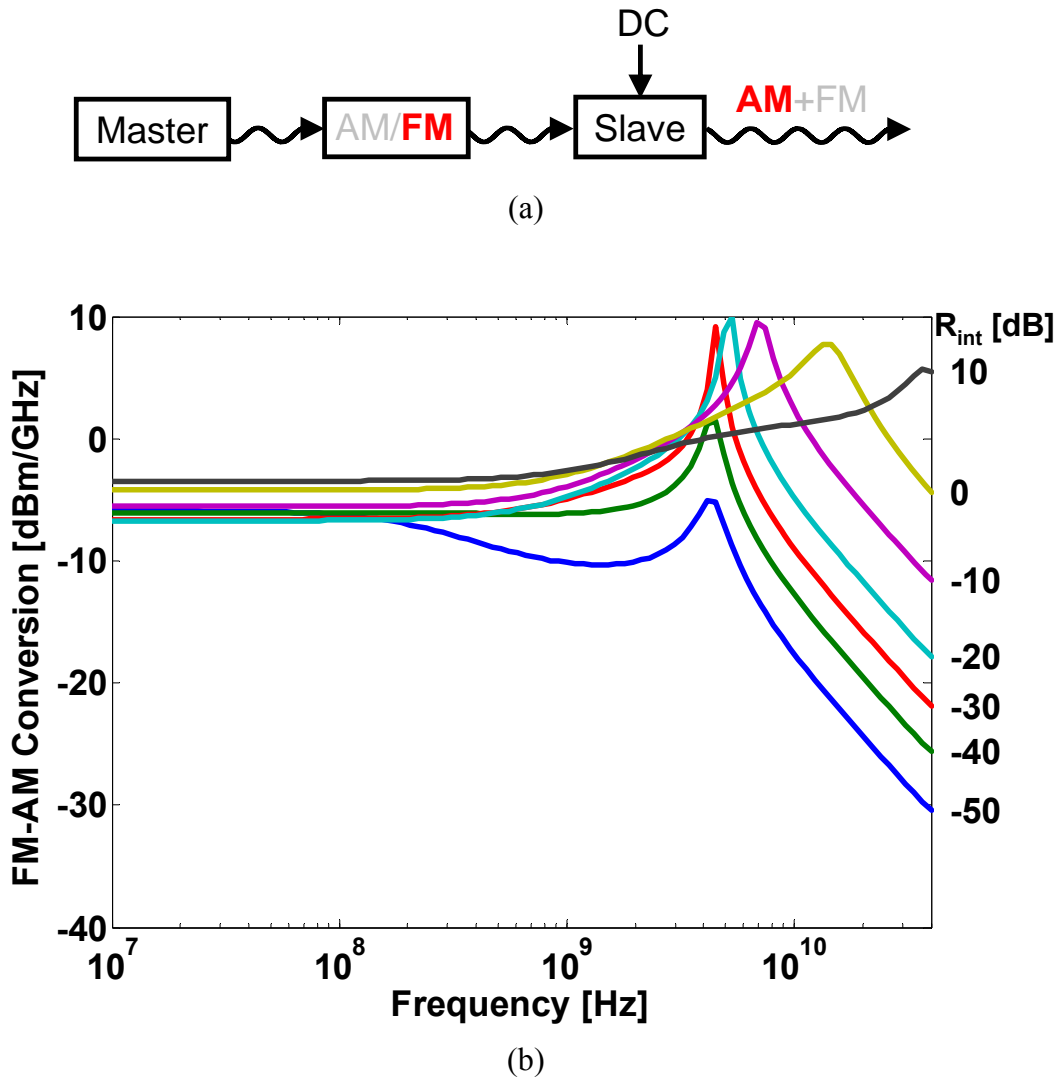


Figure 6.7 FM-to-AM conversion for various injection ratios: (a) schematic (b) frequency response. Driving source: optical FM on master. Measured output: optical AM on slave.

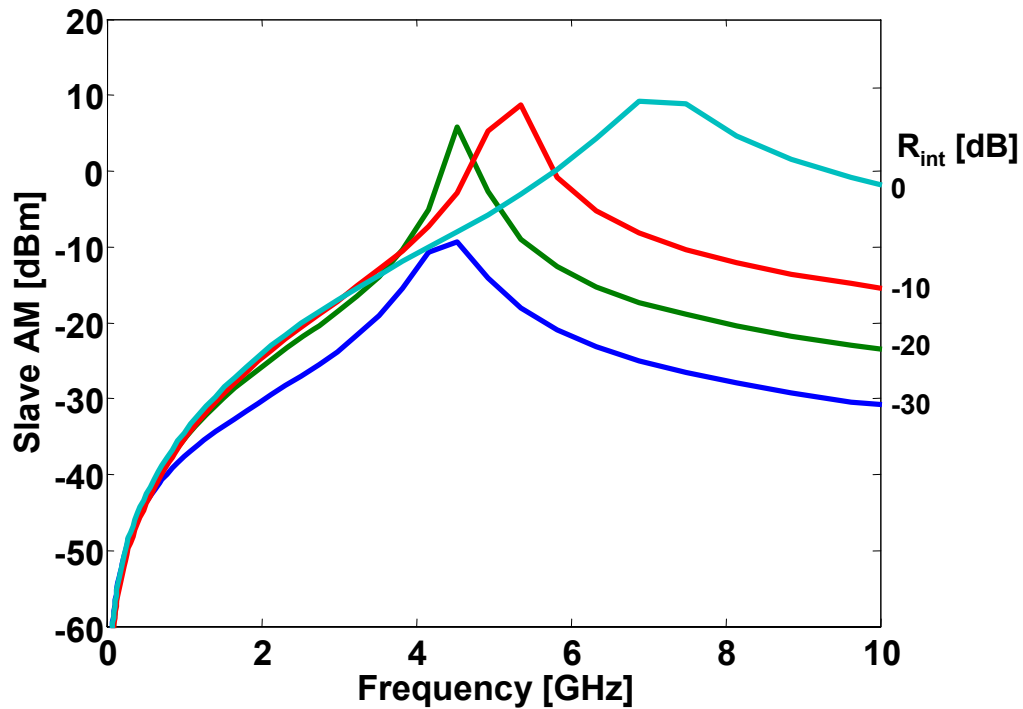


Figure 6.8 Theoretical FM-to-AM conversion for various injection ratios.

6.4.4 FM Efficiency

The second term, called FM efficiency, shows how well the master FM is mapped onto the slave FM. This may be useful for preserving an FM signal from one laser to another, for example as a regeneration technique for frequency-shift keying (FSK). Figure 6.9 shows the frequency response for FM efficiency. Note that for low frequencies, the FM efficiency is 0 dB, which means that the slave laser is exactly tracking the detuned frequency of the master. At resonance, the slave actually overshoots the master's frequency for certain injection ratios. At higher frequencies, the slave's dynamics are too slow to track the master's frequency fully, hence the FM efficiency rolls off. An interesting phenomenon is that at resonance, the laser will actually enhance the FM signal that it sees from the input. Since the injected power can be smaller than the

slave laser's output power, there will be a net DC gain. If the modulation format is chosen to be a FM style such as FSK, this type of master modulation can see gain in a narrow-band range.

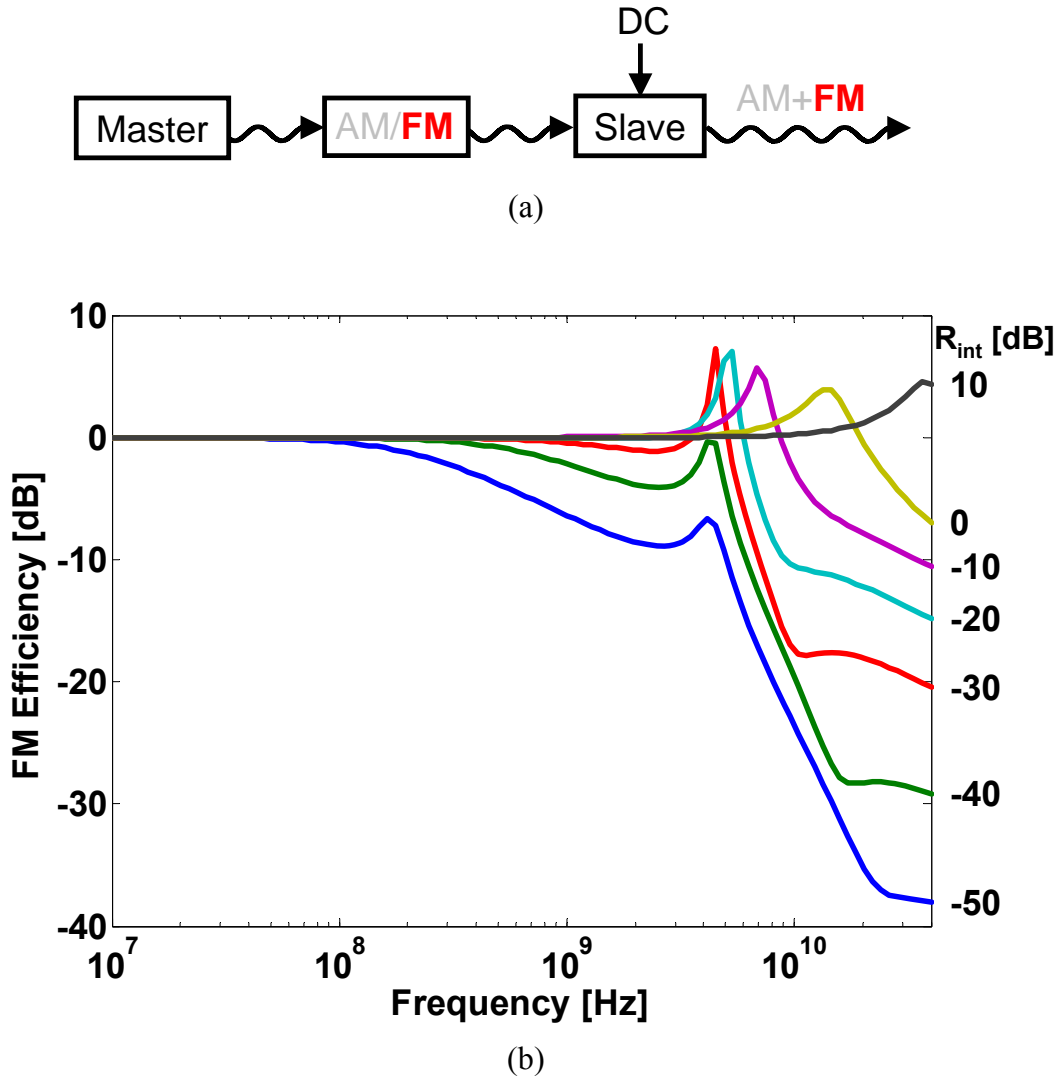


Figure 6.9 FM Efficiency for various injection ratios: (a) schematic (b) frequency response. Driving source: optical FM on master. Measured output: optical FM on slave.

6.5 Discussion

We investigated the effects of applying modulation to the master laser in injection-locked systems, both experimentally and theoretically. We experimentally verified a novel phenomenon, FM-to-AM conversion, where the FM on the master laser is converted into AM on the slave laser. We show this to have a significant effect on the slave AM for high modulation frequencies, on the order of magnitude to direct modulation gain. Experimental evidence also shows that the FM-to-AM conversion is negligible for frequencies below resonance. We modified the existing small-signal analysis theory for injection-locked lasers to include driving terms for the master AM and FM. Using this model, we show the frequency response for RAM suppression, FM efficiency, and FM-to-AM conversion. RAM suppression is shown to be inversely proportional to the injection ratio. FM efficiency is shown to have a 1 Hz-to-1 Hz frequency excursion from master to slave, for frequencies up to the resonance point. It is possible to achieve net gain as well in a narrow bandwidth. Further work will be conducted in this direction. FM-to-AM conversion is verified theoretically and shown to fit quite well with our experimental data. The bandwidth of all these effects is shown to increase, along with the enhancement of the resonance frequency, for higher injection ratios.

Chapter 7 Conclusion

7.1 Future Applications

The goal of the work in this thesis was to develop insight into the characteristics of high-speed modulation in optical injection-locked lasers. We have also experimentally probed the fundamental limits of resonance frequency and bandwidth. With the ability to create ultra-high resonance frequencies with large gain, we can develop applications based on this high-power, high-frequency source.

7.1.1 Opto-Electronic Oscillator

Microwave oscillators that synthesize high-purity, single-frequency signals are useful for many applications. Typically, these electronically-created signals are limited in phase noise by the quality factor of the oscillator. A device, called an optoelectronic oscillator (OEO), has been developed that leverages the long, low-loss nature of optical fiber to effectively increase the loop delay and hence increase the Q of the oscillator [100]. The device is shown in Figure 7.1. The pump laser is sent through the electro-optic

modulator (EOM), which then passes along a long loop of fiber. The light is converted to microwave, amplified, filtered, and then returned to the EOM as its microwave input. The amplifier gain is increased until the system achieves greater than unity gain. Without the filter, the numerous Fabry-Perot modes of the loop will have a free-spectral range equal to that of the OEO loop's time delay. The filter removes all but one mode, at the center frequency of the desired oscillator signal. The longer the optical fiber, the smaller the linewidth of the microwave signal will be. The phase noise of this system is far superior than that of a pure microwave oscillator [101]. However, its performance is limited by the noise added by the ~60 dB gain necessary from the RF amplifiers to achieve unity gain.

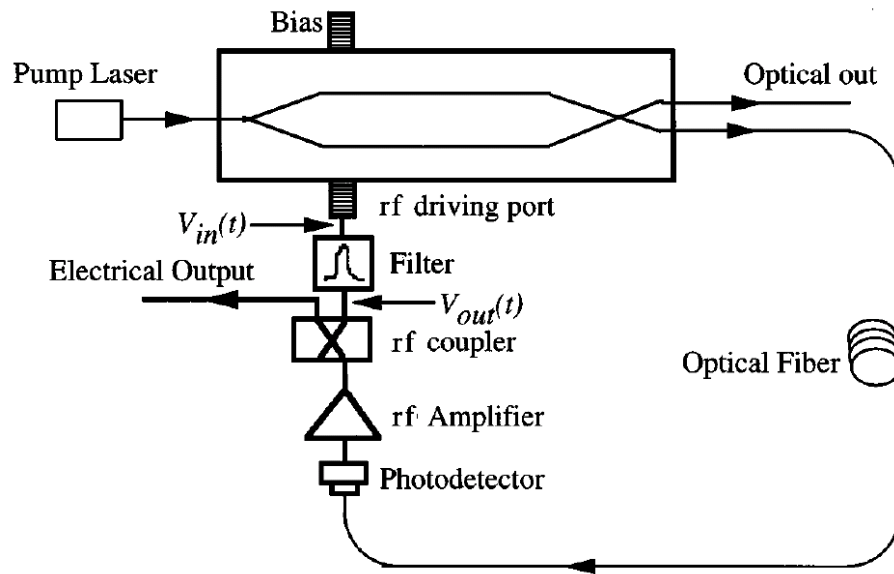
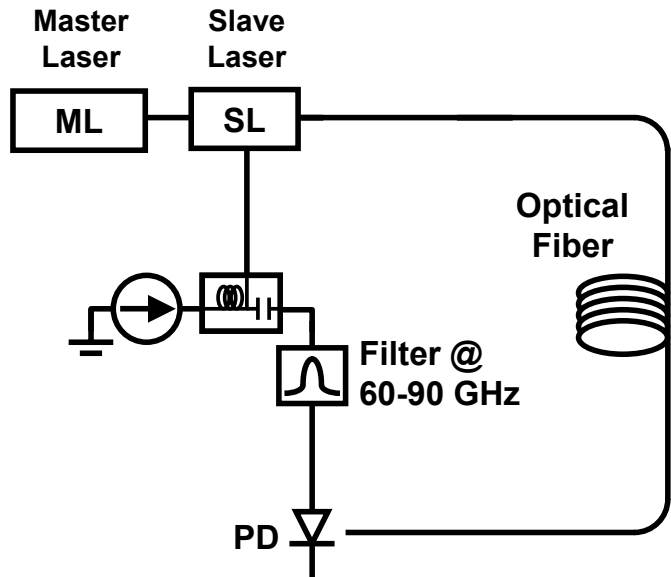


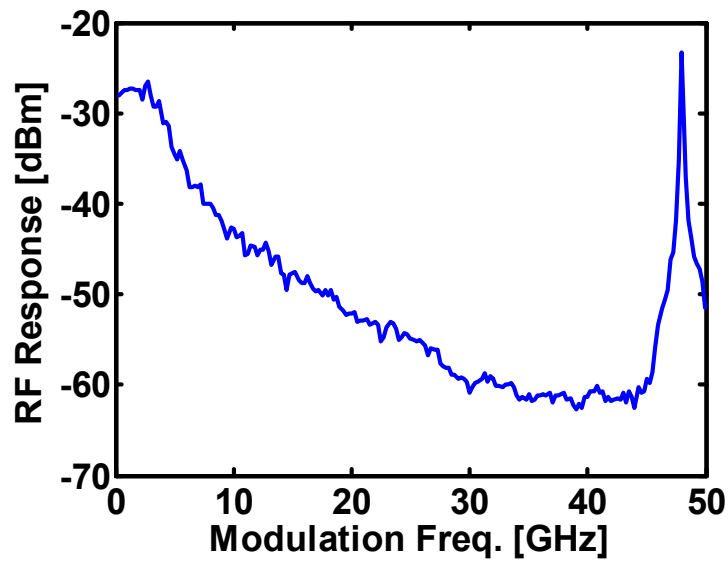
Figure 7.1 Schematic of optoelectronic oscillator. The noise is dominated by the RF amplifier.

We propose a new system, called the optical injection-locked optoelectronic oscillator (OIL-OEO) [102, 103]. The system is similar to the OEO, except the pump laser and EOM are replaced by an OIL system that is biased in the high resonance, low damping regime. The schematic is shown in Figure 7.2(a). A sample open-loop frequency

response is shown in Figure 7.2(b). The resonance frequency of 48 GHz is coupled with a -23 dBm response, for an input of -10 dBm, giving a mere 13-dB link loss. This gives an extremely high gain for a narrow-band frequency range, centered at the resonance frequency. By optimizing these preliminary results, we hope to achieve unity loop gain, thus relieving the need for RF amplifiers and potentially having extremely low phase-noise performance. Additionally, this system is widely tunable, the OIL system having tunability already shown from <10 to >72 GHz. This is an exciting potential application for our future works.



(a)



(b)

Figure 7.2 (a) Schematic of OIL-OEO. The system will have enough narrow-band gain to remove the need for RF amplifiers. Note also the high potential frequency of oscillation. (b) Experimental frequency response showing ultra-high resonance and gain at 48 GHz.

7.2 Summary

In the realm of bandwidth improvement for ever-faster and more demanding communications systems, injection locking has proven to add great value to the directly modulated laser. The bandwidth increases by direct modulation have gradually slowed as the laser community reaches the fundamental limits set by laser physics [104]. Injection locking allows us to exceed those fundamental limits, and is a technique applicable to any laser, regardless of design. This ensures universal applicability and performance improvements for any laser system. Improvements to bandwidth and resonance frequency so far have no inherent fundamental limits. Improvements are linked to injection ratio and therefore limited only to the injected power. We foresee continued improvements to both bandwidth and resonance frequency as higher power sources are implemented, or by engineering and optimizing the slave laser for superior injection locking performance.

Injection locking inherently complicates the basic laser system. System integration becomes an issue when mass production and cost are important. Since the birth of integrated circuits, there has existed a universal trend to single-chip integration; this is no different for semiconductor lasers and photonic systems. We can achieve this integration by building the master and slave lasers monolithically on a single chip [105, 106]. Analog performance benefits were observed, despite the lack of optical isolation which caused mutual locking. As new technologies of chip-level optical isolation become more prevalent [107, 108], monolithic integration of injection-locked lasers should become an increasingly attractive method of meeting record-breaking system specifications.

We have provided a brief overview of optical injection locking history, from its inception to current record-breaking performance. We also provide several intuitive

physical models and describe the most prevalent theoretical model of injection locking. This model contains the most important physical effects, including resonance frequency enhancement, noise reduction, and non-linearity suppression. We use this theory as a basis for understanding the relatively new regime of strong injection locking. We develop simple physical approximations to some of the important figure-of-merits, such as resonance frequency enhancement and damping. Utilizing our understanding of the strong injection regime, we are able to achieve a bandwidth improvement to 44 GHz, currently the highest bandwidth semiconductor laser. Additionally, we report a record 72-GHz resonance frequency, also the highest of any semiconductor laser. In order to measure these high modulation frequencies, we developed a novel heterodyne detection technique that is simple, cost-effective, and usable by a wide array of optical modulation devices. Finally, we complete our summary of optical injection locking by looking at a potential application, the OIL opto-electronic oscillator, that may be developed with our new understanding of injection locking physics. Injection locking shows great promise for improving the performance of analog and digital communication systems. As laser technology grows, we will continue to see further improvements, as the practical limits governing injection locking performance have yet to be discovered.

Appendix 1 MATLAB Code

A1.1 Locking Range Mapping: LockingRange.m

```
%LOCKINGRANGE Solves for steady-state and dynamic OIL values.
% This program chooses a value of R, then scans phi across the range
% from -pi/2 to acot(alpha), then solves dwInj, A0, N0 exactly. It
% then proceeds to solve for many other values, such as poles/zeros,
% frequency response, etc.

clear all;
#####
% LASER PARAMETERS
paramfile = 'LaserParam';
eval(paramfile);
#####
% DATA-SAVING STUFF
T          = datevec(now);
dirname    = [mfilename '_' num2str(T(1),'%02.0f') '.'
             num2str(T(2),'%02.0f') ...
             '.' num2str(T(3),'%02.0f') '.' num2str(T(4:5),'%02.0f')];
mkdir(dirname);
filename= mfilename;
copyfile([filename '.m'], dirname);
copyfile([paramfile '.m'], dirname);

%% INITIALIZE SCANNING VECTORS FOR phi and rInj
rInjM     = logspace(-2, .5, 101);
phi0M     = pi/2*sin(linspace(-pi/2*(.9999), acot(alpha)*( .99), 101));

%% FIND FREE-RUNNING VALUES
Afr       = sqrt((J-gammaN*Nth)/gammaP);
Ainj      = Afr;
```

```

%% INITIALIZE CONTAINER MATRICES
lambda = zeros(3,length(rInjM),length(phi0M));
m11M = zeros(length(rInjM),length(phi0M)); m12M = m11M; m13M = m11M;
m21M = m11M; m22M = m11M; m23M = m11M;
m31M = m11M; m32M = m11M; m33M = m11M;
zM = m11M; A0M = m11M; N0M = m11M; dwInjM = m11M;
AM = m11M; BM = m11M; CM = m11M; DM = m11M; ZM = m11M;

f = linspace(1e7,1e11,10e2+1); % [1/s] freq. vector for
Analytical P/Z response

%% MAIN LOOP
for X = 1:length(rInjM),
    tic;
    for Y = 1:length(phi0M),
        phi0 = phi0M(Y);
        rInj = rInjM(X);
        kInj = (1/tIN*(1-r0^2)/r0)*rInj;

        a = 1;
        b = -(2*kInj/gammaP*Ainj*cos(phi0) +
g*gammaN/(2*kInj*gammaP*Ainj*cos(phi0)));
        c = -Ainj^2;

        ruts = roots([1 -(2*kInj/gammaP*Ainj*cos(phi0) +
g*gammaN/(2*kInj*gammaP*Ainj*cos(phi0))) -Ainj^2]);
        I = find(ruts>=Afr);
        A0 = ruts(I);
        dN0 = -2*kInj/g*Ainj/A0*cos(phi0);
        dwInj = -kInj*sqrt(1+alpha^2)*Ainj/A0*sin(phi0+atan(alpha));

        wR = sqrt(g*gammaP*A0.^2);
        gammaR = gammaN + g*A0.^2;

        #####
        % SOLVE THE MATRIX ELEMENTS
        z = kInj*Ainj/A0;
        m11 = z*cos(phi0);
        m12 = z*A0*sin(phi0);
        m13 = -1/2*g*A0;
        m21 = -z/A0*sin(phi0);
        m22 = z*cos(phi0);
        m23 = -alpha/2*g;
        m31 = 2*A0*(gammaP-2*z*cos(phi0));
        m32 = 0;
        m33 = gammaN+g*A0^2;

        % H(s) = DM * (ZM + s) / (s^3 + AM*s^2 + BM*s + CM)
        syms s;
        MM = [m11+s m12 m13; m21 m22+s m23; m31 0 m33+s];
        MMDMsol = inv(MM)*[0; 0; 1];
        [MMsolNum, MMsolDen] = numden(MMDMsol(1));
        PolyNum(:,X,Y) = sym2poly(MMsolNum);
        PolyDen(:,X,Y) = sym2poly(MMsolDen);
    end
end

```

```

    DMpoles(:,X,Y) = roots(PolyDen(:,X,Y));
    DMzeros(:,X,Y) = roots(PolyNum(:,X,Y));
    Fresp(:,X,Y) =
abs(polyval(PolyNum(:,X,Y),j*2*pi*f)./polyval(PolyDen(:,X,Y),j*2*pi*f))
;
    RFGain(:,X,Y) = (2*gammaP*hv*A0*Fresp(:,X,Y)/q).^2*Rout/Rin;

    %% SOLVE THE DETERMINANT EQUATION: C(1)s^3 + C(2)s^2 + C(3)s +
C(4) = 0
    AM(X,Y) = m11+m22+m33;
    BM(X,Y) = m11*m22+m11*m33+m22*m33-m12*m21-m13*m31;
    CM(X,Y) = m11*m22*m33+m12*m23*m31-m12*m21*m33-m13*m31*m22;
    DM(X,Y) = -m13;
    ZM(X,Y) = (m13*m22-m12*m23)/m13;
    C(1) = 1;
    C(2) = AM(X,Y);
    C(3) = BM(X,Y);
    C(4) = CM(X,Y);
    lambda(:,X,Y) = roots(C);
    stable(X,Y) = all(real(lambda(:,X,Y))<0);

    %% SOLVE FOR ANALYTIC VALUES
    wRes(X,Y) = sqrt(wR^2 + (kInj*Ainj/A0*sin(phi0))^2);
    gamma(X,Y)= gammaR - g*dN0;
    %% SAVE STEADY-STATE VALUES
    A0M(X,Y) = A0;
    N0M(X,Y) = dN0 + Nth;
    dwInjM(X,Y) = dwInj;
    zM(X,Y) = z;
    m11M(X,Y) = m11;
    m12M(X,Y) = m12;
    m13M(X,Y) = m13;
    m21M(X,Y) = m21;
    m22M(X,Y) = m22;
    m23M(X,Y) = m23;
    m31M(X,Y) = m31;
    m32M(X,Y) = m32;
    m33M(X,Y) = m33;
end;
#####
% DISPLAY TEXT INDICATOR THAT THIS ITERATION IS FINISHED
CPUtime(X) = toc;
disp(['rInj: ' num2str(rInjM(X)) ' ' ...
      '. Elapsed Time: ' num2str(toc) ' s.']);
end;
disp(['FINISHED. Total Elapsed Time: ' num2str(sum(sum(CPUtime,2))) '
s.']);

%% FINDS SYMMETRIC BOUNDS OF LOCKING RANGE
kInjM = 1/tIN*(1-r0^2)/r0*rInjM;
lowbounds = -kInjM*Ainj./A0M(:,end)*sqrt(1+alpha^2); % phi =
acot(alpha)
asymbounds = kInjM; % phi = -pi/2
%% FIND DYNAMICALLY STABLE BOUNDARY
stablebounds = zeros(size(rInjM));

```

```

for X = 1:length(rInjM),
    temp = find(stable(X,:));
    stablebounds(X) = dwInjM(X,temp(1));
end;
%% FIND APPROX. ANALYTIC SOLUTION FOR DYNAMICALLY STABLE BOUNDARY
wRfr = sqrt(g*gammaP*Afr.^2);
wRO = sqrt(wRfr^2 + (kInjM*Ainj/Afr).^2);
phi0stable = -acos(alpha*g*gammaP*Afr^2/2./kInjM./wRO);
dwstable = -kInjM*sqrt(1+alpha^2).*sin(phi0stable+atan(alpha));
stableI = [];
for X = 1:length(rInjM)*length(phi0M), if stable(X)==1, stableI =
[stableI X];end;end;
rInjM2 = repmat(rInjM',1,length(phi0M));
phi0M2 = repmat(phi0M,length(rInjM),1);

#####
% PLOT RESULTS
LaserPlot;

#####
% SAVE DATA
% clear Fresp RFGain;
save([dirname '/' filename '.mat']);

```

A1.2 Plotting Scripts: LaserPlot.m

```

%LASERPLOT Plots many useful values.
% This script plots many useful values. See each section for the
% different values.
%
% Used by LOCKINGRANGE.

#####
% PLOT LOCKING MAP
try [Uncomment this array to run TRY conditional]
catch
figure
pH=plot(20*log10(rInjM),[kInjM;-kInjM*sqrt(1+alpha^2)]/2/pi/GHz,'k:');
patch(20*log10([rInjM fliplr(rInjM)]'),[stablebounds
fliplr(lowbounds)]'/2/pi/GHz,zeros(length(stablebounds)*2,1),[.8 .8
.8]);
patch(20*log10([rInjM fliplr(rInjM)]'),[stablebounds
fliplr(asybounds)]'/2/pi/GHz,zeros(length(stablebounds)*2,1),[1 1 1]);
xlabel('Injection Ratio [dB]');ylabel('Detuning Frequency [GHz]');
slidestyle(gcf,'linewidth',2); box on;
set(gca,'xlim',20*log10(rInjM([1 end])), 'ylim',[-100 100]);
set(pH,'linewidth',1);
end

#####
% FIND POLES OF FREE-RUNNING CASE
m33 = gammaN + g*Afr^2;
m13 = -1/2*g*Afr;
m31 = 2*gammaP*Afr;
FrespFR = abs(-m13./polyval([1 m33 -m13*m31],j*2*pi*f));

```

```

RFGainFR = (2*gammaP*hv*Afr*FrespFR/q).^2*Rout/Rin;
FRpoles = (-m33+[1 -1]*sqrt(m33^2+4*m13*m31))/2;

#####
% PLOT POLES/ZEROS
try [Uncomment this array to run TRY conditional]
catch
figure;
jetM=gray(length(phi0M)+5);
lH=plot(real(FRpoles/2/pi/GHz),imag(FRpoles/2/pi/GHz),'xk');
set(lH,'markersize',12);
hold on;
for X=1:length(phi0M),

lpH(X)=plot(real(DMpoles(:,end,X))/2/pi/GHz,imag(DMpoles(:,end,X))/2/pi
/GHz,'xb');

lzH(X)=plot(real(DMzeros(:,end,X))/2/pi/GHz,imag(DMzeros(:,end,X))/2/pi
/GHz,'ob');
    set(lpH(X),'color',jetM(X,:),'markersize',12);
    set(lzH(X),'color',jetM(X,:),'markersize',10);
end;
hold off;
slidestyle(gcf);
xlabel('Real Axis [GHz]');ylabel('Imag. Axis [GHz]');
end
#####
% PLOT RF MODULATION GAIN vs. DETUNING, 2-D CURVE FAMILY
try %[Uncomment this array to run TRY conditional]
catch
figure;
hold on;
fI = find(and(f>=0,f<=100e9));
for X=find(stable(end,:)),
    lH(X) =
plot(f(fI)/GHz,10*log10(abs(Fresp(fI,end,X)/FrespFR(fI(1)))));
    set(lH(X),'color',[0 0 (X/length(phi0M))]);
end;
frH = plot(f(fI)/GHz,10*log10(FrespFR(fI)/FrespFR(fI(1))));
set(frH,'color',[1 0 0]);
xlabel('Frequency [GHz]');ylabel('RF Gain [dB]')
% plot(wRO/2/pi/GHz,
slidestyle(gcf,'linewidth',2.5);
hold off;
end
#####
% PLOT PEAK RESPONSE VS. DETUNING
try %[Uncomment this array to run TRY conditional]
catch
figure;
wRO = sqrt(wRfr^2 + (kInjM*Ainj./A0M.*sin(phi0M)).^2);
gammaR = -g*(N0M-Nth) - alpha*g*gammaP*A0M.^2./wRO;
PeakFresp = alpha*g*A0M/2./gammaR./wRO;
pkFresp = squeeze(max(Fresp(:,:),[],1));
lfFrespFR = 1/2/Afr/gammaP;

```

```

semilogx(-((dwInjM(stableI)-
(333165558689))/2/pi),20*log10(pkFresp(stableI)/lfFrespFR));%J=1.3*Jth,
R=2
xlabel('Detuned Frequency from Locking Range Stability Edge [Hz]');
ylabel('RF Gain above Free-Running [dB]');
slidestyle(gcf,'linewidth',2.5,'fontsize',12);
end
#####
% PLOT 3-D SURF OF FREQ. vs. DETUNING
try %[Uncomment this array to run TRY conditional]
catch
figure;
surf(dwInjM/2/pi/GHz,f/GHz,10*log10(squeeze(Fresp(:,end,:)))); shading
interp; view(2);
xlabel('Frequency [GHz]');ylabel('\Delta{f} [GHz]');zlabel('Opt. Spect.
[dB]');
end

#####
% PLOT VARIABLES ACROSS THE LOCKING MAP (RInj and phase)
try [Uncomment this array to run TRY conditional]
catch
%% CREATES STATE VALUE MATRICES WITH STABLE REGIONS
wROM = squeeze(max(abs(imag(lambda(:,:,:))),[],1));
NsM = NaN*ones(length(rInjM),length(phi0M)); AsM = NsM; dwInjsM = NsM;
wROsM = NsM; maskM = NsM;
NsM(stableI) = N0M(stableI);
AsM(stableI) = A0M(stableI);
dwInjsM(stableI) = dwInjM(stableI);
wROsM(stableI) = wROM(stableI);
maskM(stableI) = 1;

[rInjsM phi0sM] = meshgrid(20*log10(rInjM),phi0M);
Xnum = size(phi0sM,1);
Ynum = size(phi0sM,2);
lengthM = Xnum*Ynum;

phi0sMT = phi0sM/pi;
AsMT = AsM'/Ainj;
NsMT = NsM'/Nth;
dwInjsMT = dwInjsM'/2/pi/GHz;
wROsMT = wROsM'/2/pi/GHz;

FaceM = zeros((Ynum-1)*(Xnum),4);
for X=1:Xnum-1,
    for Y=0:Ynum-2,
        FaceM(X+Y*(Xnum-1),:) = [X+Y*Xnum X+1+Y*Xnum X+1+(Y+1)*Xnum
X+(Y+1)*Xnum];
    end;
end;

for Y=1:Ynum, tmp = find(stable(Y,:)); X(Y)=tmp(1); end

for Y=1:Ynum-1,
    if X(Y)<=X(Y+1),

```

```

        FaceM((Ynum-1)*(Xnum-1)+Y,:) = [X(Y)+(Y-1)*Xnum X(Y+1)+(Y-
1)*Xnum X(Y+1)+Y*Xnum X(Y)+(Y-1)*Xnum];
    else
        FaceM((Ynum-1)*(Xnum-1)+Y,:) = [X(Y)+(Y-1)*Xnum X(Y+1)+Y*Xnum
X(Y)+Y*Xnum X(Y)+(Y-1)*Xnum];
    end;
end

VertM = [phi0sMT(1:lengthM)' rInjsM(1:lengthM)'];

%% PLOT CARRIER DENSITY
ColorM = NsMT(1:lengthM)';
figure;
patch('Vertices',VertM,'Faces',FaceM, ...
    'FaceVertexCData',ColorM,'FaceColor','Interp','LineStyle','none');
shading interp;view(2);colorbar
xlabel('Phase, \phi_0/\pi');ylabel('Injection Ratio
[dB]');zlabel('N_0/N_{th}');title('Carrier Density, N_0/N_{th}');
slidestyle(gcf,'linewidth',2); box on;
set(gca,'xlim',[-.5 acot(alpha)/pi*.99],'xtick',[-.5 -.25 0
acot(alpha)/pi],'xticklabel',{'-0.5','-
0.25','0',num2str(acot(alpha)/pi,'%1.2f')})
set(gca,'ylim',20*log10(rInjM([1 end])));
temp = get(findobj(gcf,'tag','Colorbar'),'ylim');
set(findobj(gcf,'tag','Colorbar'),'ylim',[temp(1) 1])

%% PLOT FREQ. DETUN.
ColorM = dwInjsMT(1:lengthM)';
figure;
patch('Vertices',VertM,'Faces',FaceM, ...
    'FaceVertexCData',ColorM,'FaceColor','Interp','LineStyle','none');
shading interp;view(2);colorbar
xlabel('Phase, \phi_0/\pi');ylabel('Injection Ratio
[dB]');zlabel('\Delta{f}');title('Detuning Freq., \Delta{f} [GHz]');
slidestyle(gcf,'linewidth',2); box on;
set(gca,'xlim',[-.5 acot(alpha)/pi*.99],'xtick',[-.5 -.25 0
acot(alpha)/pi],'xticklabel',{'-0.5','-
0.25','0',num2str(acot(alpha)/pi,'%1.2f')})
set(gca,'ylim',20*log10(rInjM([1 end])));

%% PLOT RO FREQ
ColorM = wROsMT(1:lengthM)';
figure;
patch('Vertices',VertM,'Faces',FaceM, ...
    'FaceVertexCData',ColorM,'FaceColor','Interp','LineStyle','none');
shading interp;view(2);colorbar
xlabel('Phase, \phi_0/\pi');ylabel('Injection Ratio
[dB]');zlabel('f_{RO} [GHz]');title('Resonance Freq., f_{RO} [GHz]');
slidestyle(gcf,'linewidth',2); box on;
set(gca,'xlim',[-.5 acot(alpha)/pi*.99],'xtick',[-.5 -.25 0
acot(alpha)/pi],'xticklabel',{'-0.5','-
0.25','0',num2str(acot(alpha)/pi,'%1.2f')})
set(gca,'ylim',20*log10(rInjM([1 end])));
temp = get(findobj(gcf,'tag','Colorbar'),'ylim');
set(findobj(gcf,'tag','Colorbar'),'ylim',[0 temp(2)]);

```

```

%% PLOT FIELD AMPLITUDE
ColorM = AsMT(1:lengthM)';
figure;
patch('Vertices',VertM,'Faces',FaceM, ...
      'FaceVertexCData',ColorM,'FaceColor','Interp','LineStyle','none');
shading interp;view(2);colorbar
xlabel('Phase, \phi_0/\pi');ylabel('Injection Ratio
[dB]');zlabel('A_0/A_{fr}');title('Normalized Field, A_0/A_{fr}');
slidestyle(gcf,'linewidth',2); box on;
set(gca,'xlim',[-.5 acot(alpha)/pi*.99],'xtick',[-.5 -.25 0
acot(alpha)/pi],'xticklabel',{'-0.5','-
0.25','0',num2str(acot(alpha)/pi,'%1.2f')})
set(gca,'ylim',20*log10(rInjM([1 end])));
temp = get(findobj(gcf,'tag','Colorbar'),'ylim');
set(findobj(gcf,'tag','Colorbar'),'ylim',[1 temp(2)])

#####
%% PLOT VARIABLES VERSUS LOCKING MAP (RInj and Fdet)
VertM = [rInjsM(1:lengthM)' dwInjsMT(1:lengthM)'];

% PLOT RO FREQUENCY VS. LOCKING MAP
ColorM = wROsMT(1:lengthM)';
figure;
pH=plot(20*log10(rInjM),[kInjM;lowbounds;stablebounds]/2/pi/GHz,'k');
patch('Vertices',VertM,'Faces',FaceM, ...
      'FaceVertexCData',ColorM,'FaceColor','Interp','LineStyle','none');
view(2);colorbar
xlabel('Injection Ratio [dB]');ylabel('Detuning Frequency
[GHz]');title('Resonance Freq., f_{RO} [GHz]');
slidestyle(gcf,'linewidth',2); box on;
set(pH,'linewidth',1.5);
set(gca,'xlim',20*log10(rInjM([1 end])), 'ylim',[-100 100]);
temp = get(findobj(gcf,'tag','Colorbar'),'ylim');
set(findobj(gcf,'tag','Colorbar'),'ylim',[0 temp(2)]);

% PLOT NORMALIZED FIELD VS. LOCKING MAP
ColorM = AsMT(1:lengthM)';
figure;
pH=plot(20*log10(rInjM),[kInjM;lowbounds;stablebounds]/2/pi/GHz,'k');
patch('Vertices',VertM,'Faces',FaceM, ...
      'FaceVertexCData',ColorM,'FaceColor','Interp','LineStyle','none');
shading interp;view(2);colorbar
xlabel('Injection Ratio [dB]');ylabel('Detuning Frequency
[GHz]');title('Normalized Field, A_0/A_{fr}');
slidestyle(gcf,'linewidth',2); box on;
set(pH,'linewidth',1.5);
set(gca,'xlim',20*log10(rInjM([1 end])), 'ylim',[-100 100]);
temp = get(findobj(gcf,'tag','Colorbar'),'ylim');
set(findobj(gcf,'tag','Colorbar'),'ylim',[1 temp(2)]);

% PLOT NORMALIZED CARRIER VS. LOCKING MAP
ColorM = NsMT(1:lengthM)';
figure;
pH=plot(20*log10(rInjM),[kInjM;lowbounds;stablebounds]/2/pi/GHz,'k');

```

```

patch('Vertices',VertM,'Faces',FaceM, ...
      'FaceVertexCData',ColorM,'FaceColor','Interp','LineStyle','none');
shading interp;view(2);colorbar
xlabel('Injection Ratio [dB]');ylabel('Detuning Frequency
[GHz]');title('Carrier Density, N_0/N_{th}');
slidestyle(gcf,'linewidth',2); box on;
set(pH,'linewidth',1.5);
set(gca,'xlim',20*log10(rInjM([1 end])), 'ylim',[-100 100]);
temp = get(findobj(gcf,'tag','Colorbar'),'ylim');
set(findobj(gcf,'tag','Colorbar'),'ylim',[temp(1) 1])

% PLOT PHASE VS. LOCKING MAP
ColorM = phi0sMT(1:lengthM)';
figure;
pH=plot(20*log10(rInjM),[kInjM;lowbounds;stablebounds]/2/pi/GHz,'k');
patch('Vertices',VertM,'Faces',FaceM, ...
      'FaceVertexCData',ColorM,'FaceColor','Interp','LineStyle','none');
shading interp;view(2);colorbar
xlabel('Injection Ratio [dB]');ylabel('Detuning Frequency
[GHz]');title('Phase, \phi_0/\pi');
slidestyle(gcf,'linewidth',2); box on;
set(pH,'linewidth',1.5);
set(gca,'xlim',20*log10(rInjM([1 end])), 'ylim',[-100 100]);
temp = get(findobj(gcf,'tag','Colorbar'),'ylim');
set(findobj(gcf,'tag','Colorbar'),'ylim',[-0.5 temp(2)]);
end

```

A1.3 Laser Parameters: LaserParam.m

```

%LASERPARAM Loads modelocked laser parameters.
% Loads physical parameters, laser geometry, and biasing.
%
% Used by LOCKINGRANGE.

#####
% CONSTANTS
q      = 1.6022e-19; % [C]      Coulomb/charge
h      = 6.626076e-34; % [J*s]   Planck's constant
c      = 2.9979e10; % [cm/s]   Speed of light
mu0    = pi*4e-9; % [A/cm]   Magnetic permeability
e0     = 1/c^2/mu0; % [V/cm]   Electric permittivity
eta0   = sqrt(mu0/e0); % [Ohm]  Impedence of free space
#####
% UNITS
ns     = 1e-9; % [s] # of seconds in a nanosecond
(abbrev.)
ps     = 1e-12; % [s] # of seconds in a picosecond
(abbrev.)
pJ     = 1e-12; % [s] # of Joules in a picoJoule
(abbrev.)
kHz    = 1e3; % [Hz] kiloHertz/Hertz
MHz    = 1e6; % [Hz] MegaHertz/Hertz
GHz    = 1e9; % [Hz] GigaHertz/Hertz
um     = 1e-4; % [cm] # of microns in a centimeter
nm     = 1e-7; % [cm] # of nanometers in a centimeter

```

```

Ang      = 1e-8;          % [cm]      # of Angstroms in a centimeter
mA       = 1e-3;          % [A]       # of milliAmps in an Amp
kA       = 1e3;           % [A]       # of kiloAmps in an Amp
mW       = 1e-3;          % [A]       # of milliWatts in a Watt
#####
% THEORETICAL QUANTITIES

lambda   = 1550*nm;      % [cm]      Lasing wavelength
hv       = h*c/lambda;   % [J]       Energy/photon
g        = 2.5e-16*8.5e9/1.5e-10*0.4;
Nth      = 2.214e8;
gammaP   = 1/3e-12;
gammaN   = 1e9;
tIN      = 7e-12;
r0       = 0.548;
alpha    = 3;
V        = 120e-18;
Ith      = 33.5e-3;
Jth      = Ith/q;
J        = 5*Jth;
Einj     = 0;
dwinj    = 0;

Rin      = 4;
Rout     = 50;

```

A1.4 Differential Equation Solution: LaserODE.m

```

%LASERODE Solves the OIL differential equations.
% This script is similar to LOCKINGRANGE, but solves the OIL
% differential equations to reach the steady-state. This is useful
% when trying to solve the frequency response, by adding time-
% dependent inputs. It can be used to solve IMD3, etc.

clear all;
#####
% LASER PARAMETERS
paramfile = 'LaserParam';
eval(paramfile);
odefile   = 'RateEq';
#####
% DATA-SAVING STUFF
T         = datevec(now);
dirname   = [mfilename '_' num2str(T(1),'%02.0f') '.'
num2str(T(2),'%02.0f') ...
 '.' num2str(T(3),'%02.0f') '.' num2str(T(4:5),'%02.0f')];
mkdir(dirname);
filename= mfilename;
copyfile([filename '.m'], dirname);
copyfile([paramfile '.m'], dirname);
copyfile([odefile '.m'], dirname);
#####
% COMPUTATION PARAMETERS
%
% |   init   |   trans   |   steady state   |

```

```

% -tInit          0          tSS          tWin
tInit   = 50*ns;          % [s]          Time window to reach initial DC
freerunning steadystate
tWin    = 100*ns;        % [s]          Time window of each simulation
tSS     = 50*ns;        % [s]          How far into the time window needed
to
%
% reach a steady-state modulation
tDISP   = 40*ns;        % [s]          Length of time window to graph
#####
% CONSTRUCT TIME AND FREQUENCY VECTORS
dt       = 1/(200*GHz);    % [s]          spacing between time pts.
tPTS     = round(tWin/dt); %          # of pts. in time vector
t        = linspace(0,tWin-dt,tPTS);% [s]    time vector
fPTS     = length(find(t>=tSS)); %          # of pts. for FFT
df       = 1/fPTS/dt;     % [1/s]       discretized frequency
spacing
fmax     = 1/dt/2;        % [1/s]       max. freq.
fFFT     = round([-fmax:df:fmax-df]);% [1/s]   freq. vector for FFT
f        = linspace(0,1e11,1e3+1); % [1/s]   freq. vector for Analytical
P/Z response
#####
% SCANNING PARAMETERS
v1Name   = 'fDet';
v1S      = 'f_{det}';
v1M      = [-70:5:15]*GHz; rInj = 1e-0;
v1Scale  = GHz;
v1UnitS  = 'GHz';
v1Format = '%-2.3f';
v1LogLin = 'lin';
#####
% FREE-RUNNING STEADY-STATE
#####
% SOLVE ODE FOR STEADY STATE DC VALUES, FREE-RUNNING
Aifr    = sqrt((J-gammaN*Nth)/gammaP); % initial guess
tspan   = [-tInit 0];
AphiN0  = [Aifr; 0; Nth];
odeparam = odeset('RelTol',1e-8);
ParamList = {g Nth 0 0 alpha 0 J 0 0 gammaN gammaP};
[ti, AphiNi] = ode23(odefile,tspan,AphiN0,odeparam,ParamList);
A_Tr     = AphiNi(:,1);
phi_Tr   = zeros(size(A_Tr));
N_Tr     = AphiNi(:,3);
#####
% DETERMINE STEADY-STATE VALUES
Afr      = mean(A_Tr(find(ti>-10*ns)));
phifr    = 0;
Nfr      = mean(N_Tr(find(ti>-10*ns)));
#####
% FIND POLES OF FREE-RUNNING CASE
m33      = gammaN + g*Afr^2;
m13      = -1/2*g*Afr;
m31      = 2*gammaP*Afr;
FRpoles  = (-m33+[1 -1]*sqrt(m33^2+4*m13*m31))/2;
#####
% INJECTED STEADY-STATE

```

```

#####
EM = zeros(length(v1M),tPTS); NM=EM;
FMs= zeros(length(v1M),fPTS); FMe=FMs;
Ldim1 = length(v1M);
figure;
for X = 1:Ldim1
    tic;
    eval(['v1Name ' = ' num2str(v1M(X)) ';' ]);
    % INJECTION PARAMETERS
    dwInj = 2*pi*fDet;
    AInj = Afr; % they set AInj to be same as As of free-running
laser.
    #####
    %% FINDS SYMMETRIC BOUNDS OF LOCKING RANGE
    kInj = 1/tIN*(1-r0^2)*rInj/r0;
    bounds = kInj*sqrt(1+alpha^2)/2/pi;
    asymbounds = kInj/2/pi;
    #####
    %% FIND INITIAL GUESS STEADY-STATE VALUES WITH INJECTION
    phiis = asin(-dwInj/kInj/sqrt(1+alpha^2)) - atan(alpha);
    Nis = Nth - 2*kInj.*cos(phiis)/g;
    dNis = Nis - Nth;
    Ais = sqrt((AINj^2 - gammaN/gammaP/dNis)/(1 + g*dNis/gammaP));
    #####
    % SOLVE ODE FOR STEADY STATE DC VALUES, W/ INJECTION TERMS
    tspan = [0; tWin];
    AphiN0 = [Ais phiis Nis];
    odeparam = odeset('RelTol',1e-8);
    ParamList = {g Nth kInj AInj alpha dwInj J 0 0 gammaN gammaP};
    [tODE, AphiN] = ode23(odefile,tspan,AphiN0,odeparam,ParamList);
    AphiN(find(~isfinite(AphiN))) = eps;
    #####
    % THESE ARE THE 3 STATE VARIABLES
    A_ODE = AphiN(:,1);
    phi_ODE = AphiN(:,2);
    N_ODE = AphiN(:,3);
    #####
    % DETERMINE MOD. DEPTH FROM FREQUENCY SPECTRUM
    A = spline(tODE,A_ODE,t); %
    phi = spline(tODE,phi_ODE,t); %
    N = spline(tODE,N_ODE,t); %
    phiss = phi-dwInj*t;
    #####
    % DETERMINE S.S. VALUES WITH THE INJECTION
    A0 = mean(A(find(t>=tSS)));
    phi0 = mean(phi(find(t>=tSS)));
    N0 = mean(N(find(t>=tSS)));
    #####
    % DETERMINE OPTICAL SPECTRUM THROUGH FOURIER TRANSFORM
    E = A.*exp(j*phi);
    F = fftshift(fft(E(find(t>=tSS)))); % [?] Freq-Domain of
optical spectrum
    #####
    % SAVE VALUES INTO MATRICES
    A0M(X) = A0; phi0M(X) = phi0; N0M(X) = N0;

```

```

EM(X,:) = E;
NM(X,:) = N;
FM(X,:) = abs(fftshift(fft(E(1:fPTS))));
FMe(X,:) = abs(fftshift(fft(E([end-fPTS+1:end]))));
FM(X,:) = abs(fftshift(fft(E)));
plot(fFFT/GHz, 10*log10(abs(FMe(X,:)))); xlabel('Frequency [GHz]');
ylabel('Opt. Spec. [dB]');
title([v1Name '=' num2str(v1M(X)/v1Scale, v1Format) ' ' v1Units]);
drawnow;
#####
% FIND THE POLES
z = kInj*AInj/A0;
m11 = z*cos(phi0);
m12 = z*A0*sin(phi0);
m13 = -1/2*g*A0;
m21 = -z/A0*sin(phi0);
m22 = z*cos(phi0);
m23 = -alpha/2*g;
m31 = 2*A0*(gammaP-2*z*cos(phi0));
m32 = 0;
m33 = gammaN+g*A0^2;

syms s;
MM = [m11+s m12 m13; m21 m22+s m23; m31 0 m33+s];
A = m11+m22+m33;
B = m11*m22+m11*m33+m22*m33-m12*m21-m13*m31;
C = m11*m22*m33+m12*m23*m31-m12*m21*m33-m13*m31*m22;
M = -m13;
Z = (m13*m22-m12*m23)/m13;
MMDMsol = inv(MM)*[0; 0; 1];
[MMsolNum, MMsolDen] = numden(MMDMsol(1));
PolyNum(X,:) = sym2poly(MMsolNum);
PolyDen(X,:) = sym2poly(MMsolDen);
DMpoles(:,X) = roots(PolyDen(X,:));
DMzeros(:,X) = roots(PolyNum(X,:));
if size(DMzeros,1) == 1, DMzeros= repmat(DMzeros,2,1); end;
Fresp(X,:) =
abs(polyval(PolyNum(X,:), j*2*pi*f) ./ polyval(PolyDen(X,:), j*2*pi*f));
RFGain(X,:) = (2*gammaP*hv*A0*Fresp(X,)/q).^2*Rout/Rin;
RFPeak = (2*gammaP*hv*/q/g/A0^2).^2*Rout/Rin;
#####
% DISPLAY TEXT INDICATOR THAT THIS ITERATION IS FINISHED
CPUTime(X) = toc;
disp([v1Name ': ' num2str(v1M(X)/v1Scale, v1Format) ' ' v1Units ...
      '. Elapsed Time: ' num2str(toc) ' s.']);
end;
disp(['FINISHED. Total Elapsed Time: ' num2str(sum(sum(CPUTime,2))) '
s.']);
#####
% Set the entire vector of values to the names instead of 'v1M' and
'v2M'
eval([v1Name '= v1M;']);
#####
% SAVE DATA
clear A phi N phiss Fresp AphiN AphiNi *ODE ti *_Tr *pd phase;

```

```

save([dirname '/' filename '.mat']);

#####
% PLOT POLES/ZEROS

try [Uncomment this array to run TRY conditional]
catch
figure;
jetM=jet(length(v1M));
lH=plot(real(FRpoles/2/pi/GHz),imag(FRpoles/2/pi/GHz),'xk');
set(lH,'markersize',12);
hold on;
for X=1:length(v1M),

lpH(X)=plot(real(DMpoles(:,X))/2/pi/GHz,imag(DMpoles(:,X))/2/pi/GHz,'xb
');

lzH(X)=plot(real(DMzeros(:,X))/2/pi/GHz,imag(DMzeros(:,X))/2/pi/GHz,'ob
');
    set(lpH(X),'color',jetM(X,:),'markersize',12);
    set(lzH(X),'color',jetM(X,:),'markersize',10);
end;
hold off;
slidestyle(gcf);
xlabel('Real Axis [GHz]');ylabel('Imag. Axis [GHz]');
print(['-f' num2str(gcf)], '-djpeg', [dirname '/' filename '_PZ.jpg']);
hgsave([dirname '/' filename '_PZ.fig']);
end

#####
% PLOT FREQ. RESP vs. DETUNING CONTOUR

try %[Uncomment this array to run TRY conditional]
catch
figure;
fI = find(and(f>=0,f<=100e9));
surf(f(fI)/GHz,fDet/GHz,10*log10(abs(Fresp(:,fI)))); shading interp;
xlabel('Frequency [GHz]');ylabel('\Delta{f} [GHz]');zlabel('Freq. Resp.
[dB]');
print(['-f' num2str(gcf)], '-djpeg', [dirname '/' filename
'_FResp.jpg']);
hgsave([dirname '/' filename '_FResp3D.fig']);
end

#####
% PLOT GAIN vs. DETUNING, 2-D CURVE FAMILY

try [Uncomment this array to run TRY conditional]
catch
figure;
hold on;
fI = find(and(f>=0,f<=100e9));
for X=1:length(v1M),
%     lH(X) =
plot(f(fI)/GHz,20*log10(abs(Fresp(X,fI)/max(Fresp(1,:)))));

```

```

    LH(X) = plot(f(fI)/GHz,10*log10(RFGain(X,fI)));
    set(LH(X),'color',[0 0 (X/length(v1M))]);
end;
xlabel('Frequency [GHz]');ylabel('RF Gain [dB]')
slidestyle(gcf,'linewidth',3);
print(['-f' num2str(gcf)], '-djpeg', [dirname '/' filename
'_FResp.jpg']);
hgsave([dirname '/' filename '_FResp.fig']);
end

#####
% PLOT 3-D SURF OF FREQ. vs. DETUNING

try %[Uncomment this array to run TRY conditional]
catch
figure;
surf(f/GHz,fDet/GHz,10*log10(FMs)); shading interp; view(2);
xlabel('Frequency [GHz]');ylabel('\Delta{f} [GHz]');zlabel('Opt. Spect.
[dB]');
end

#####
% PLOT 3-D SURF OF SHIFTED (for Detuning) FREQ. vs. DETUNING
fPTS = tPTS; % # of pts. for FFT
df = 1/fPTS/dt; % [1/s] discretized frequency
spacing
fmax = 1/dt/2; % [1/s] max. freq.
ffull = round([-fmax:df:fmax-df]);% [1/s] freq. vector

```

A1.5 Injection-Locked Laser Rate Equation: RateEq.m

```

%RATEEQ Rate equation function for OIL.
% This function describes the differential equations for OIL.
%
% Used by LASERODE.

function dAdphiN = rateeqmurakami(t,AphiN,flag,ParamList)

[g Nth kInj AInj alpha dwInj J dJ fM gammaN gammaP] =
deal(ParamList{:});

A = AphiN(1);
phi = AphiN(2);
N = AphiN(3);

dA = 1/2*g*(N-Nth)*A + kInj*AINj*cos(phi);
dphi = alpha/2*g*(N-Nth) - kInj*AINj/A*sin(phi) - dwInj;
dN = J + dJ*sin(fM*2*pi*t) - gammaN*N - (gammaP + g*(N-Nth))*A^2;

dAdphiN = [dA; dphi; dN];

```

BIBLIOGRAPHY

- [1] K. Iwashita and K. Nakagawa, "Suppression of mode partition noise by laser diode light injection," *IEEE Trans. Microwave Theory Tech.*, vol. 30, pp. 1657-1662, 1982.
- [2] C. H. Henry, N. A. Olsson, and N. K. Dutta, "Locking range and stability of injection locked 1.54 μm InGaAsP semiconductor lasers," *IEEE Journal of Quantum Electronics*, vol. QE-21, pp. 1152-6, 1985.
- [3] A. Murakami, K. Kawashima, and K. Atsuki, "Cavity resonance shift and bandwidth enhancement in semiconductor lasers with strong light injection," *IEEE Journal of Quantum Electronics*, vol. 39, pp. 1196-204, 2003.
- [4] T. B. Simpson, J. M. Liu, and A. Gavrielides, "Bandwidth enhancement and broadband noise reduction in injection-locked semiconductor lasers," *IEEE Photonics Technology Letters*, vol. 7, pp. 709-11, 1995.
- [5] X. J. Meng, T. Chau, D. T. K. Tong, and M. C. Wu, "Suppression of second harmonic distortion in directly modulated distributed feedback lasers by external light injection," *Electronics Letters*, vol. 34, pp. 2040-1, 1998.
- [6] L. Chrostowski, C. H. Chang, and C. Chang-Hasnain, "Reduction of relative intensity noise and improvement of spur-free dynamic range of an injection locked VCSEL," presented at 2003 IEEE LEOS Annual Meeting Conference Proceedings (IEEE Cat. No.03CH37460). IEEE. Part vol.2, 2003, pp.706-7 vol.2. Piscataway, NJ, USA., 2003.
- [7] N. Schunk and K. Petermann, "Noise analysis of injection-locked semiconductor injection lasers," *IEEE Journal of Quantum Electronics*, vol. QE-22, pp. 642-50, 1986.
- [8] M. C. Espana-Boquera and A. Puerta-Notario, "Noise effects in injection locked laser simulation: phase jumps and associated spectral components," *Electronics Letters*, vol. 32, pp. 818-19, 1996.
- [9] J. M. Liu, H. F. Chen, X. J. Meng, and T. B. Simpson, "Modulation bandwidth, noise, and stability of a semiconductor laser subject to strong injection locking," *IEEE Photonics Technology Letters*, vol. 9, pp. 1325-7, 1997.
- [10] G. Yabre, H. De Waardt, H. P. A. van den Boom, and G. D. Khoe, "Noise characteristics of single-mode semiconductor lasers under external light injection," *IEEE Journal of Quantum Electronics*, vol. 36, pp. 385-93, 2000.
- [11] C. Lin and F. Mengel, "Reduction of frequency chirping and dynamic linewidth in high-speed directly modulated semiconductor lasers by injection locking," *Electronics Letters*, vol. 20, pp. 1073-5, 1984.
- [12] H. Toba, Y. Kobayashi, K. Yanagimoto, H. Nagai, and M. Nakahara, "Injection-locking technique applied to a 170 km transmission experiment at 445.8 Mbit/s," *Electronics Letters*, vol. 20, pp. 370-1, 1984.

- [13] N. A. Olsson, H. Temkin, R. A. Logan, L. F. Johnson, G. J. Dolan, J. P. van der Ziel, and J. C. Campbell, "Chirp-free transmission over 82.5 km of single mode fibers at 2 Gbit/s with injection locked DFB semiconductor lasers," *Journal of Lightwave Technology*, vol. LT-3, pp. 63-7, 1985.
- [14] H.-K. Sung, T. Jung, M. C. Wu, D. Tishinin, K. Y. Liou, and W. T. Tsang, "Optical Injection-Locked Gain-Lever Distributed Bragg Reflector Lasers with Enhanced RF Performance," *Proc. 2004 International Topical Meeting on Microwave Photonics*, 2004.
- [15] H.-K. Sung, E. K. Lau, and M. C. Wu, "Near-single sideband modulation in strong optical injection-locked semiconductor lasers," presented at OFCNFOEC 2006. 2006 Optical Fiber Communication Conference and National Fiber Optic Engineers Conference. Anaheim, CA, 2006.
- [16] L. Goldberg, A. M. Yurek, H. F. Taylor, and J. F. Weller, "35 GHz microwave signal generation with an injection-locked laser diode," *Electronics Letters*, vol. 21, pp. 814-15, 1985.
- [17] A. J. Seeds, I. D. Blanchflower, N. J. Gomes, G. King, and S. J. Flynn, "New developments in optical control techniques for phased array radar," presented at 1988 IEEE MTT International Microwave Symposium Digest (Cat. No.88CH2489-3). IEEE. 1988, pp.905-8 vol.2. New York, NY, USA., 1988.
- [18] S. Kobayashi and T. Kimura, "Optical phase modulation in an injection locked AlGaAs semiconductor laser," *IEEE Transactions on Microwave Theory & Techniques*, vol. MTT-30, pp. 1650-7, 1982.
- [19] S. Yamashita and D. Matsumoto, "Waveform reshaping based on injection locking of a distributed-feedback semiconductor laser," *Photonics Technology Letters, IEEE*, vol. 12, pp. 1388-1390, 2000.
- [20] A. Pikovsky, M. Rosenblum, J. Kurths, and B. Chirikov, "Synchronization : A Universal Concept in Nonlinear Sciences," in *Cambridge Nonlinear Science Series*. Cambridge, U.K.: Cambridge University Press, 2003.
- [21] R. Adler, "A study of locking phenomena in oscillators," *Proceedings of IRE*, vol. 34, pp. 351-7, 1946.
- [22] R. H. Pantell, "The laser oscillator with an external signal," *Proceedings of the IEEE*, vol. 53, pp. 474-477, 1965.
- [23] H. L. Stover and W. H. Steier, "Locking of laser oscillators by light injection," *Applied Physics Letters*, vol. 8, pp. 91-93, 1966.
- [24] C. J. Buczek and R. J. Freiberg, "Hybrid injection locking of higher power CO₂ lasers," *IEEE Journal of Quantum Electronics*, vol. qe-8, pp. 641-50, 1972.
- [25] S. Kobayashi and T. Kimura, "Coherence on injection phase-locked AlGaAs semiconductor laser," *Electronics Letters*, vol. 16, pp. 668-670, 1980.

- [26] Y. Yamamoto, "Receiver performance evaluation of various digital optical modulation-demodulation systems in the 0.5-10 μm wavelength region," *IEEE Journal of Quantum Electronics*, vol. QE-16, pp. 1251-9, 1980.
- [27] S. Kobayashi and T. Kimura, "Optical FM signal amplification by injection locked and resonant type semiconductor laser amplifiers," *Quantum Electronics, IEEE Journal of*, vol. 18, pp. 575, 1982.
- [28] S. Kasapi, S. Lathi, and Y. Yamamoto, "Sub-shot-noise frequency-modulation spectroscopy by use of amplitude-squeezed light from semiconductor lasers," *Journal of the Optical Society of America B-Optical Physics*, vol. 17, pp. 275-9, 2000.
- [29] R. D. Esman, L. Goldberg, and J. F. Weller, "Optical phase control of an optically injection-locked FET microwave oscillator," *IEEE Transactions on Microwave Theory & Techniques*, vol. 37, pp. 1512-18, 1989.
- [30] C. Lin, J. K. Andersen, and F. Mengel, "Frequency chirp reduction in a 2.2 Gbit/s directly modulated InGaAsP semiconductor laser by CW injection," *Electronics Letters*, vol. 21, pp. 80-1, 1985.
- [31] L. Goldberg, H. F. Taylor, and J. F. Weller, "FM sideband injection locking of diode lasers," *Electronics Letters*, vol. 18, pp. 1019-20, 1982.
- [32] R. Lang, "Injection locking properties of a semiconductor laser," *IEEE Journal of Quantum Electronics*, vol. QE-18, pp. 976-83, 1982.
- [33] X. J. Meng, T. Jung, C. Tai, and M. C. Wu, "Gain and bandwidth enhancement of directly modulated analog fiber optic links using injection-locked gain-coupled DFB lasers," presented at International Topical Meeting on Microwave Photonics. MWP'99. Technical Digest (Cat. No.99EX301). IEEE. Part vol.1, 1999, pp.141-4 vol.1. Piscataway, NJ, USA., 1999.
- [34] S. Saito, F. Mogensen, and H. Olesen, "Effective bandwidth for FM noise suppression in an injection-locked semiconductor laser," *Electronics Letters*, vol. 21, pp. 1173-5, 1985.
- [35] F. Mogensen, H. Olesen, and G. Jacobsen, "FM noise suppression and linewidth reduction in an injection-locked semiconductor laser," *Electronics Letters*, vol. 21, pp. 696-7, 1985.
- [36] F. Mogensen, H. Olesen, and G. Jacobsen, "Locking conditions and stability properties for a semiconductor laser with external light injection," *IEEE Journal of Quantum Electronics*, vol. QE-21, pp. 784-93, 1985.
- [37] H. K. Sung, T. Jung, M. C. Wu, D. Tishinin, T. Tanbun-Ek, K. Y. Liou, and W. T. Tsang, "Modulation bandwidth enhancement and nonlinear distortion suppression in directly modulated monolithic injection-locked DFB lasers," presented at MWP 2003 Proceedings. International Topical Meeting on Microwave Photonics (IEEE Cat. No. 03EX933). IEEE. 2004, pp.27-30. Piscataway, NJ, USA., 2003.

- [38] L. Chrostowski, X. Zhao, C. J. Chang-Hasnain, R. Shau, M. Ortsiefer, and M. Amann, "50 GHz directly-modulated injection-locked 1.55 μm VCSELs," presented at Optical Fiber Communication Conference, 2005. Technical Digest., 2005.
- [39] E. K. Lau, H.-K. Sung, and M. C. Wu, "Ultra-high, 72 GHz resonance frequency and 44 GHz bandwidth of injection-locked 1.55- μm DFB lasers," presented at OFCNFOEC 2006. 2006 Optical Fiber Communication Conference and National Fiber Optic Engineers Conference. Anaheim, CA, 2006.
- [40] H. L. T. Lee, R. J. Ram, O. Kjebon, and R. Schatz, "Bandwidth enhancement and chirp reduction in DBR lasers by strong optical injection," presented at Conference on Lasers and Electro-Optics (CLEO 2000). Technical Digest. Postconference Edition. TOPS Vol.39 (IEEE Cat. No.00CH37088). Opt. Soc. America. 2000, pp.99-100. Salem, MA, USA., 2000.
- [41] S. K. Hwang, J. M. Liu, and J. K. White, "35-GHz modulation bandwidth in injection-locked semiconductor lasers," 2003.
- [42] X. J. Meng, T. Chau, and M. C. Wu, "Improved intrinsic dynamic distortions in directly modulated semiconductor lasers by optical injection locking," *IEEE Trans. Microwave Theory Tech.*, vol. 47, pp. 1172-1176, 1999.
- [43] L. Chrostowski, C. Chih-Hao, and C. J. Chang-Hasnain, "Enhancement of dynamic range in 1.55- μm VCSELs using injection locking," *Photonics Technology Letters, IEEE*, vol. 15, pp. 498-500, 2003.
- [44] J. H. Seo, Y. K. Seo, and W. Y. Choi, "Nonlinear distortion suppression in directly modulated DFB lasers by sidemode optical injection," 2001.
- [45] X. Jin and S. L. Chuang, "Relative intensity noise characteristics of injection-locked semiconductor lasers," *Applied Physics Letters*, vol. 77, pp. 1250-2, 2000.
- [46] K. Schunk, G. Grosskopf, L. Kuller, and K. Petermann, "Noise characteristics of injection locked semiconductor lasers," presented at IOOC-ECOC '85. 5th International Conference on Integrated Optics and Optical Fibre Communication and 11th European Conference on Optical Communication. Technical Digest. Istituto Int. Comunicazioni. 1985, pp.717-20 vol.1. Genoa, Italy., 1985.
- [47] K. J. Vahala, M. A. Newkirk, and T. R. Chen, "The optical gain lever: A novel gain mechanism in the direct modulation of quantum well semiconductor lasers," *Applied Physics Letters*, vol. 54, pp. 2506-8, 1989.
- [48] N. Moore and K. Y. Lau, "Ultrahigh efficiency microwave signal transmission using tandem-contact single quantum well GaAlAs lasers," *Applied Physics Letters*, vol. 55, pp. 936-8, 1989.
- [49] H. K. Sung, T. Jung, D. Tishinin, K. Y. Liou, W. T. Tsang, and M. C. Wu, "Optical injection-locked gain-lever distributed Bragg reflector lasers with enhanced RF performance," presented at 2004 IEEE International Topical Meeting on Microwave Photonics. Ogunquit, ME, 2004.

- [50] Y. Yamamoto, "Receiver performance evaluation of various digital optical modulation-demodulation systems in the 0.5-10 μm wavelength region," *IEEE Journal of Quantum Electronics*, vol. QE-16, pp. 1251-9, 1980.
- [51] J. M. Kahn, "1 Gbit/s PSK homodyne transmission system using phase-locked semiconductor lasers," *Photonics Technology Letters, IEEE*, vol. 1, pp. 340-342, 1989.
- [52] A. C. Bordonalli, C. Walton, and A. J. Seeds, "High-performance phase locking of wide linewidth semiconductor lasers by combined use of optical injection locking and optical phase-lock loop," *Lightwave Technology, Journal of*, vol. 17, pp. 328-342, 1999.
- [53] L. Wangkuen, M. M. Mielke, S. Etemad, and P. J. Delfyett, Jr., "Injection-locked passively mode-locked semiconductor laser for optical heterodyne detection using a single axial mode," presented at Enabling Photonic Technologies for Aerospace Applications VI. Orlando, FL, 2004.
- [54] L. Wangkuen, M. Mielke, S. Etemad, and P. J. Delfyett, "Subgigahertz channel filtering by optical heterodyne detection using a single axial mode from an injection-locked passively mode-locked semiconductor laser," *Photonics Technology Letters, IEEE*, vol. 16, pp. 1945-1947, 2004.
- [55] W. Lee and P. J. Delfyett, "Dual-mode injection locking of two independent modelocked semiconductor lasers," *Electronics Letters*, vol. 40, pp. 1182-1183, 2004.
- [56] T. Jung, S. Ji-Lin, D. T. K. Tong, S. Murthy, M. C. Wu, T. Tanbun-Ek, W. Wenshen, R. Lodenkamper, R. Davis, L. J. Lembo, and J. C. Brock, "CW injection locking of a mode-locked semiconductor laser as a local oscillator comb for channelizing broad-band RF signals," *Microwave Theory and Techniques, IEEE Transactions on*, vol. 47, pp. 1225, 1999.
- [57] A. Kuramoto and S. Yamashita, "All-optical regeneration using a side-mode injection-locked semiconductor laser," *Selected Topics in Quantum Electronics, IEEE Journal of*, vol. 9, pp. 1283-1287, 2003.
- [58] A. Umbach, G. Unterborsch, R. P. Braun, and G. Grobkopf, "Stable optical source and high-speed photodetector used for remote fiber-optic 64-GHz mm wave generation," presented at OFC '98 Optical Fiber Communication Conference and Exhibit. Technical Digest Conference Edition 1998 OSA Technical Digest Series. Vol.2. San Jose, CA, 1998.
- [59] E. Wong, X. Zhao, and C. Chang-Hasnain, "Uncooled, optical injection-locked 1.55 μm VCSELs for upstream transmitter in WDM-PONs," *OFC 2006*, 2006.
- [60] X. Wang, Y. Liu, H. Lu, X. Wang, and Z. Fang, "Intensity-modulating characteristics of a laser diode subjected to optical injection," *Optics Letters*, vol. 30, pp. 860-2, 2005.

- [61] A. Kaszubowska, P. Anandarajah, and L. P. Barry, "Improved performance of a hybrid radio/fiber system using a directly modulated laser transmitter with external injection," *IEEE Photonics Technology Letters*, vol. 14, pp. 233-5, 2002.
- [62] L. A. Johansson and A. J. Seeds, "36-GHz 140-Mb/s radio-over-fiber transmission using an optical injection phase-lock loop source," *Photonics Technology Letters, IEEE*, vol. 13, pp. 893-895, 2001.
- [63] L. Hai-Han, H. Hsu-Hung, S. Heng-Sheng, and W. Ming-Chuan, "Fiber optical CATV system-performance improvement by using external light-injection technique," *Photonics Technology Letters, IEEE*, vol. 15, pp. 1017-1019, 2003.
- [64] R. A. York and T. Itoh, "Injection- and phase-locking techniques for beam control antenna arrays," *IEEE Trans. Microwave Theory Tech.*, vol. 46, pp. 1920-1929, 1998.
- [65] C. Henry, "Theory of the linewidth of semiconductor lasers," *Quantum Electronics, IEEE Journal of*, vol. 18, pp. 259, 1982.
- [66] T. B. Simpson, J. M. Liu, A. Gavrielides, V. Kovanis, and P. M. Alsing, "Period-doubling route to chaos in a semiconductor laser subject to optical injection," *Applied Physics Letters*, vol. 64, pp. 3539-41, 1994.
- [67] X. J. Meng, C. Tai, and M. C. Wu, "Experimental demonstration of modulation bandwidth enhancement in distributed feedback lasers with external light injection," *Electronics Letters*, vol. 34, pp. 2031, 1998.
- [68] L. Chrostowski, X. Zhao, C. J. Chang-Hasnain, R. Shau, M. Ortsiefer, and M. C. Amann, "50-GHz Optically Injection-Locked 1.55- μm VCSELs," *Photonics Technology Letters, IEEE*, vol. 18, pp. 367-369, 2006.
- [69] T. B. Simpson and J. M. Liu, "Enhanced modulation bandwidth in injection-locked semiconductor lasers," *IEEE Photonics Technology Letters*, vol. 9, pp. 1322-4, 1997.
- [70] A. Yariv, *Optical Electronics in Modern Communications*, 5th ed. New York: Oxford University Press, 1997.
- [71] L. P. Barry, P. Anandarajah, and A. Kaszubowska, "Optical pulse generation at frequencies up to 20 GHz using external-injection seeding of a gain-switched commercial Fabry-Perot laser," *IEEE Photonics Technology Letters*, vol. 13, pp. 1014-16, 2001.
- [72] L. Chrostowski, X. Zhao, and C. J. Chang-Hasnain, "Microwave Performance of Optically Injection-Locked VCSELs," *Microwave Theory and Techniques, IEEE Transactions on*, vol. 54, pp. 788-796, 2006.
- [73] S. K. Hwang, J. M. Liu, and J. K. White, "35-GHz intrinsic bandwidth for direct modulation in 1.3- μm semiconductor lasers subject to strong injection locking," *IEEE Photonics Technology Letters*, vol. 16, pp. 972-4, 2004.

- [74] H.-H. Lu, H.-H. Huang, H.-S. Su, and M.-C. Wang, "Fiber optical CATV system-performance improvement by using external light-injection technique," *Photonics Technology Letters, IEEE*, vol. 15, pp. 1017-1019, 2003.
- [75] L. A. Coldren and S. W. Corzine, *Diode Lasers and Photonic Integrated Circuits*. New York: John Wiley & Sons, Inc., 1995.
- [76] J. C. Slater, *Microwave Electronics*. New York: Van Nostrand, 1950.
- [77] K. Noguchi, O. Mitomi, and H. Miyazawa, "Millimeter-wave Ti:LiNbO₃ optical modulators," *Journal of Lightwave Technology*, vol. 16, pp. 615-19, 1998.
- [78] R. G. Walker, "Electro-optic modulation at mm-wave frequencies in GaAs/AlGaAs guided wave devices," presented at LEOS '95. IEEE Lasers and Electro-Optics Society 1995 Annual Meeting. 8th Annual Meeting. Conference Proceedings. San Francisco, CA, 1995.
- [79] M. Lee, H. E. Katz, C. Erben, D. M. Gill, P. Gopalan, J. D. Heber, and D. J. McGee, "Broadband modulation of light by using an electro-optic polymer," *Science*, vol. 298, pp. 1401-3, 2002.
- [80] R. Lewen, S. Irmscher, U. Westergren, L. Thylen, and U. Eriksson, "Traveling-wave electrode electroabsorption modulators toward 100 Gb/s," presented at Optical Fiber Communication Conference (OFC). Los Angeles, CA, 2004.
- [81] T. Ido, S. Tanaka, M. Suzuki, M. Koizumi, H. Sano, and H. Inoue, "Ultra-high-speed multiple-quantum-well electro-absorption optical modulators with integrated waveguides," *Journal of Lightwave Technology*, vol. 14, pp. 2026-2034, 1996.
- [82] X. Zhang, A. Gutierrez-Aitken, D. Klotzkin, P. Bhattacharya, C. Caneau, and R. Bhat, "0.98- μ m multiple-quantum-well tunneling injection laser with 98-GHz intrinsic modulation bandwidth," *IEEE. IEEE Journal of Selected Topics in Quantum Electronics*, vol.3, no.2, April 1997, pp.309-14. USA., 1997.
- [83] T. S. Tan, R. L. Jungerman, and S. S. Elliott, "Optical receiver and modulator frequency response measurement with a Nd:YAG ring laser heterodyn technique," *IEEE Transactions on Microwave Theory & Techniques*, vol. 37, pp. 1217-22, 1989.
- [84] C. D. Watson, D. A. Humphreys, and M. G. F. Wilson, "Calibration of Optical Modulators by Optical Down-Conversion," *IEEE Photonics Technology Letters*, vol. 5, pp. 1005-1007, 1993.
- [85] O. Mitomi, K. Noguchi, and H. Miyazawa, "Estimation of frequency response for high-speed LiNbO₃ optical modulators," *IEE Proceedings-Optoelectronics*, vol. 146, pp. 99-104, 1999.
- [86] A. K. M. Lam, M. Fairburn, and N. A. F. Jaeger, "Wide-band electrooptic intensity modulator frequency response measurement using an optical heterodyne down-conversion technique," *IEEE Transactions on Microwave Theory and Techniques*, vol. 54, pp. 240-246, 2006.

- [87] Y. Yamamoto and T. Kimura, "Coherent Optical Fiber Transmission-Systems," *IEEE Journal of Quantum Electronics*, vol. 17, pp. 919-935, 1981.
- [88] H.-K. Sung, T. Jung, M. C. Wu, D. Tishinin, K. Y. Liou, and W. T. Tsang, "Optical generation of millimeter-waves using monolithic sideband injection locking of a two-section DFB laser," presented at Lasers and Electro-Optics Society, 2003. LEOS 2003. The 16th Annual Meeting of the IEEE 2003.
- [89] Y. Matsui, H. Murai, S. Arahira, S. Kutsuzawa, and Y. Ogawa, "30-GHz bandwidth 1.55- μ m strain-compensated InGaAlAs-InGaAsP MQW laser," *Photonics Technology Letters, IEEE*, vol. 9, pp. 25, 1997.
- [90] L. Bach, W. Kaiser, J. P. Reithmaier, A. Forchel, T. W. Berg, and B. Tromborg, "Enhanced direct-modulated bandwidth of 37 GHz by a multi-section laser with a coupled-cavity-injection-grating design," *Electronics Letters*, vol. 39, pp. 1592-1593, 2003.
- [91] S. Weisser, E. C. Larkins, K. Czotscher, W. Benz, J. Daleiden, I. Esquivias, J. Fleissner, J. D. Ralston, B. Romero, R. E. Sah, A. Schonfelder, and J. Rosenzweig, "Damping-limited modulation bandwidths up to 40 GHz in undoped short-cavity In_{0.35}Ga_{0.65}As-GaAs multiple-quantum-well lasers," *IEEE Photonics Technology Letters*, vol. 8, pp. 608-10, 1996.
- [92] P. A. Morton, R. A. Logan, T. Tanbun-Ek, P. F. Sciortino, Jr., A. M. Sergent, R. K. Montgomery, and B. T. Lee, "25 GHz bandwidth 1.55 μ m GaInAsP p-doped strained multiquantum-well lasers," *Electronics Letters*, vol. 28, pp. 2156, 1992.
- [93] E. Goutain, J. C. Renaud, M. Krakowski, D. Rondi, R. Blondeau, and D. Decoster, "30 GHz bandwidth, 1.55 μ m MQW-DFB laser diode based on a new modulation scheme," *Electronics Letters*, vol. 32, pp. 896, 1996.
- [94] O. Kjebon, R. Schatz, S. Lourdudoss, S. Nilsson, B. Stalnacke, and L. Backbom, "Two-section InGaAsP DBR-lasers at 1.55 μ m wavelength with 31 GHz direct modulation bandwidth," presented at Conference Proceedings. 1997 International Conference on Indium Phosphide and Related Materials (Cat. No.97CH36058). IEEE. 1997, pp.665-8. New York, NY, USA., 1997.
- [95] T. R. Chen, J. Ungar, X. L. Yeh, and N. Bar-Chaim, "Very large bandwidth strained MQW DFB laser at 1.3 μ m," *Photonics Technology Letters, IEEE*, vol. 7, pp. 458, 1995.
- [96] K. L. Lear, V. M. Hietala, H. Q. Hou, J. Banas, B. E. Hammons, J. Zolper, and S. P. Kilcoyne, "High-speed 850 nm oxide-confined vertical cavity surface emitting lasers," presented at Proceedings of Ultrafast Electronics and Optoelectronics TOPS Vol.13 (ISBN 1 55752 486 6). Incline Village, NV, 1997.
- [97] T. B. Simpson and F. Doft, "Double-locked laser diode for microwave photonics applications," *IEEE Photonics Technology Letters*, vol. 11, pp. 1476-8, 1999.

- [98] T. B. Simpson, J. M. Liu, and A. Gavrielides, "Small-signal analysis of modulation characteristics in a semiconductor laser subject to strong optical injection," *Quantum Electronics, IEEE Journal of*, vol. 32, pp. 1456-1468, 1996.
- [99] J. Wang, M. K. Haldar, L. Li, and F. V. C. Mendis, "Enhancement of modulation bandwidth of laser diodes by injection locking," *Photonics Technology Letters, IEEE*, vol. 8, pp. 34, 1996.
- [100] X. S. Yao and L. Maleki, "High frequency optical subcarrier generator," *Electronics Letters*, vol. 30, pp. 1525-6, 1994.
- [101] N. Yu, E. Salik, and L. Maleki, "Ultralow-noise mode-locked laser with coupled optoelectronic oscillator configuration," *Optics Letters*, vol. 30, pp. 1231-3, 2005.
- [102] S. C. Chan and J. M. Liu, "Tunable narrow-linewidth photonic microwave generation using semiconductor laser dynamics," *IEEE Journal of Selected Topics in Quantum Electronics*, vol. 10, pp. 1025-32, 2004.
- [103] H. K. Sung, E. K. Lau, M. C. Wu, X. Zhao, D. Parekh, C. J. Chang-Hasnain, and M. C. Wu, "Optically Injection-Locked Optoelectronic Oscillators with Low RF Threshold Gain," in *Conference on Lasers and Electro-Optics (CLEO 2007)*. Baltimore, MD: Opt. Soc. America., submitted 2007.
- [104] R. Olshansky, P. Hill, V. Lanzisera, and W. Powazinik, "Frequency response of 1.3 μ m InGaAsP high speed semiconductor lasers," *Quantum Electronics, IEEE Journal of*, vol. 23, pp. 1410, 1987.
- [105] A. Q. Liu, X. M. Zhang, H. Cai, D. Y. Tang, and C. Lu, "Miniaturized injection-locked laser using microelectromechanical systems technology," *Applied Physics Letters*, vol. 87, 2005.
- [106] H. K. Sung, T. Jung, M. C. Wu, D. Tishinin, T. Tanbun-Ek, K. Y. Liou, and W. T. Tsang, "Modulation bandwidth enhancement and nonlinear distortion suppression in directly modulated monolithic injection-locked DFB lasers," presented at MWP 2003 Proceedings. International Topical Meeting on Microwave Photonics (IEEE Cat. No. 03EX933). IEEE. 2004, pp.27-30. Piscataway, NJ, USA., 2004.
- [107] M. Vanwolleghem, W. Van Parys, D. Van Thourhout, R. Baets, F. Lelarge, O. Gauthier-Lafaye, B. Thedrez, R. Wirix-Speetjens, and J. De Boeck, "First experimental demonstration of a monolithically integrated InP-based waveguide isolator," presented at Optical Fiber Communication Conference (OFC) (IEEE Cat. No.04CH37532). Opt. Soc. America. 2004, pp.3 pp.. Washington, DC, USA., 2004.
- [108] T. R. Zaman, X. Guo, and R. J. Ram, "Proposal for a polarization-independent integrated optical circulator," *IEEE Photonics Technology Letters*, vol. 18, pp. 1359-61, 2006.